Two-dimensional Molecular Self-assemblies on Surfaces Studied by Low-Temperature Scanning Tunneling Microscopy

HUANG YULI

(B. Sc, SHANDONG UNIV)

A THESIS SUBMITTED

FOR THE DEGREE OF DOCTOR OF PHILOSOPHY

DEPARTMENT OF PHYSICS

NATIONAL UNIVERSITY OF SINGAPORE

(2010)

ACKNOWLEDGEMENT

I would like to take this chance to express my deepest gratitude for all the help, support, and encouragement I have received during my Ph. D study.

First and foremost, I owe my most sincere gratitude to my supervisors, Prof. Andrew Thye Shen Wee and Assist. Prof. Chen Wei. Without their patient guidance, help and encouragement, it is impossible for me to obtain the necessary research skills in such a short time and finish this thesis in four years. I appreciate the valuable discussions and helpful suggestions gave by Prof. Andrew T. S Wee during my research. His in-depth reviews of my every manuscript and also this thesis word by word despite his busy schedule also gave me a great impression. Assist. Prof. Chen Wei is the one who taught me the basic experimental operations, data analysis and also academic writing skills. With his help in my daily research life, the difficulties that I meet during my experiments could always be resolved immediately. My supervisors have also spurred me to communicate and cooperate with people from different fields and this has benefited me a lot in research. They set good examples as active researchers.

I would like to sincerely thank my lab colleagues, Dr. Huang Han, Dr. Chen Lan, and Mr. Zhang Hong Liang, for their friendly assistance in experimental operations, equipment maintenance and academic discussions. They are also my good friends who made the four years enjoyable. I warmly thank Dr. Gao Xing

Yu, Dr. Qi Dong Chen and Mr. Chen Shi from Singapore Synchrotron Light Source (SSLS) for their help in photoelectron spectroscopy measurements. I also owe my thanks to Dr. Li Hui for his help in conducting theoretical simulations for my research work. His work is indispensable in making the results consistent and convincing. The other lab members, including Mr. Wong, Ms. Xie Lan Fei, Mr. Yong Chaw Keong, Dr. Sun Jia Tao, Mr. Wong Swee Liang, Dr. Iman Santosoi, Mr Niu Tian Chao, Mr. Wang Rui and many others, also helped me a lot during my study.

I am grateful to my family for their support and love throughout my studies. I would also like to thank the schoolmates and friends who have accompanied me through these years.

Finally, the financial support from the National University of Singapore is gratefully acknowledged.

LIST OF PUBLICATIONS

1. Wei Chen*, Han Huang, Shi Chen, Yu Li Huang, Xing Yu Gao, and Andrew Thye Shen Wee*
   Molecular Orientation-Dependent Ionization Potential of Organic Thin Films
   Chemical Materials, Vol. ***20***, No. 22, 7017–7021, November, 2008

2. Yu Li Huang, Wei Chen*, Shi Chen, and Andrew Thye ShenWee*
   Low-temperature scanning tunneling microscopy and near-edge X-ray absorption fine structure investigation of epitaxial growth of $F_{16}CuPc$ thin films on graphite
   Applied Physics A: Materials Science & Processing, Vol. ***95***, 107–111, January, 2009

3. Yu Li Huang, Wei Chen*, Han Huang, Dong Chen Qi, Shi Chen, Xing Yu Gao, Jens Pflaum, and Andrew Thye Shen Wee*
   Ultrathin Films of Di-indenoperylene on Graphite and SiO_2
   Journal of Physical Chemistry C, Vol. ***113***, No. 21, 9251–9255, May, 2009

4. Wei Chen*, Shuang Chen, Shi Chen, Yu Li Huang, Han Huang, Dong Chen Qi, Xing Yu Gao, Jing Ma, and Andrew Thye Shen Wee
   Orientation-controlled charge transfer at CuPc/$F_{16}CuPc$ interfaces
   Journal of Applied Physics, Vol. ***106***, 064910, September, 2009

5. Han Huang, Yuli Huang, Jens Pflaum, Andrew Thye Shen Wee, and Wei Chen*
   Nanoscale phase separation of a binary molecular system of copper phthalocyanine and di-indenoperylene on Ag(111)

Appl. Phys. Lett., Vol. **95**, 263309, December, 2009

6. Yu Li Huang, Wei Chen*, Hui Li, Jing Ma, Jens Pflaum, and Andrew Thye Shen Wee*
   Tunable Two-Dimensional Binary Molecular Networks
   Small, Vol. ***6***, No. 1, 70–75, January, 2010

7. Yu Li Huang, Hui Li, Jing Ma, Han Huang, Wei Chen*, and Andrew T. S. Wee*
   Scanning Tunneling Microscopy Investigation of Self-Assembled CuPc/F_{16}CuPc Binary Superstructures on Graphite
   Langmuir, Vol. ***26***, 3329-3334, March, 2010

8. Yu Li Huang, Wei Chen*, and Andrew Thye ShenWee*
   Molecular Trapping on Two-dimensional Binary Supramolecular Networks
   (Submitted)

9. Swee Liang Wong, Han Huang, Yu Li Huang, Yu Zhan Wang, Xing Yu Gao, Toshiyasu Suzuki, Wei Chen*, and Andrew Thye Shen Wee*
   Effect of fluorination on the molecular packing of perfluoropentacene and pentacene ultrathin films on Ag(111)
   Journal of Physical Chemistry C, Vol. ***114***, No. 20, 9356–9361, May, 2010

10. Yu Li Huang, Rui Wang, Tian Chao Niu, Satoshi Kera, Nobuo Ueno, Jens Pflaum, Andrew Thye Shen Wee, and Wei Chen*,
    Molecular Dipole Chain Arrays on Graphite via nanoscale phase separation.
    (Accepted, *Chemical Communications*)

11. Yu Li Huang, Wei Chen*, Andrew Thye Shen Wee*, et. al.
    Reversible Single-molecule Switch Controlled by STM
    (Preparing)

TABLE OF CONTENTS

Summary

We represent a promising bottom-up approach to fabricate two-dimensional (2D) molecular nanostructures over macroscopic areas in this thesis. A wide range of 2D molecular self-assemblies on surfaces and their formations of regular supramolecular arrays are demonstrated by low-temperature scanning tunneling microscopy (LT-STM) in ultra-high vacuum (UHV) environments. Intensive effort is devoted to construct mono- and bi-component organic molecular networks via various intermolecular interactions and molecule-substrate interactions. This thesis aims for a comprehensive understanding of the underlying mechanisms that control the surface self-assemblies. Complementary experiments including photoelectron spectroscopy (PES) and near-edge X-ray absorption fine structure (NEXAFS) measurements are performed to investigate electronic energy alignments and supramolecular packing structures of organic thin films.

Epitaxial growth of organic π-conjugated molecular films on solid surfaces is investigated initially, including copper hexadecafluorophthalocyanine (F_{16}CuPc) and di-indenoperylene (DIP) ultra-thin films on graphite and/or SiO_2. The supramolecular packing structure and molecular orientation of the organic thin film, which is mainly governed by the balance between molecule-substrate interfacial interactions and intermolecular interactions, could determine its electronic properties. An understanding of the growth mechanism can facilitate

the fabrication of organic thin films with desired properties, and thereby improve the performance of organic devices based on organic thin films.

To increase the tunability and functionality of the surface-supported nanostructures, robust 2D binary molecular networks, whose overall arrangements could be tuned by varying molecular intermixing ratios as well as molecular building blocks, are constructed by co-adsorption of F_{16}CuPc with copper phthalocyanine (CuPc), *p*-sexiphenyl (6P), pentacene, and DIP respectively. The structural stability of the binary molecular arrays is enhanced by multiple intermolecular hydrogen bonds formed between the F_{16}CuPc molecules and the CuPc, 6P, pentacene or DIP molecules. Theoretical simulations based on molecular dynamics (MD) and density functional theory (DFT) are performed to estimate the hydrogen bonding interactions of each observed network. Some of the rigid hydrogen-bonded networks can be used to adsorb incoming guest molecules at specific adsorption sites and facilitate the formation of regular patterns on the underlying templates. The formation of 2^{nd} layer supramolecular patterns constrained by the underlying molecular networks, suggests a possible large scale method to fabricate organic nanostructure arrays with desired functionality for potential use in molecular nanodevices.

The chloroaluminum phthalocyanine (ClAlPc) molecule with electric dipole moment perpendicular to its molecular π-plane, is investigated in the last part of this thesis. The supramolecular packing structures of ClAlPc monolayer and bi-layer films are studied. Formations of molecular dipole chain arrays via nanoscale phase separation are observed in the binary molecular system of ClAlPc and DIP

on graphite. Reversible single-molecule manipulation is achieved by tip-induced configurational transformation of the ClAlPc molecule in the close-packed monolayer, which makes it a promising basic information bit candidate for ultrahigh density information storage.

LIST OF TABLES

LIST OF FIGURES

LIST OF ABBREVIATIONS

2D	Two-Dimensional
LT-STM	Low Temperature Scanning Tunneling Microscopy
STS	Scanning Tunneling Spectroscopy
MBE	Molecular Beam Epitaxy
FIM	Field Ion Microscopy
AFM	Atomic Force Microscope
SEM	Scanning Electron Microscopy
TEM	Transmission Electron Microscopy
NFSOM	Near-Field Scanning Optical Microscopy
LEEM	Low-Energy Electron Microscopy
PEEM	Photoemission Electron Microscopy
UHV	Ultra-High Vacuum
PTCDA	3,4,9,10-perylenetetracarboxylic dianhydride
TCNQ	Teracyanoquinonedimethane
BN	Boron Nitride
SiC	Silicon Carbide
PTCDI	3,4,9,10-perylenetetracarboxylic diimide
F_{16}CuPc	Copper Hexadecafluorophthalocyanine
CuPc	Copper phthalocyanine
ClAlPc	Chloroaluminum Phtholocyanine
DIP	Di-indenoperylene
6P	*p*-sexiphenyl
LDOS	Local Density of States
HOMO	Highest Occupied Molecular Orbital
LUMO	Lowest Unoccupied Molecular Orbital
IETS	Inelastic Tunneling Spectroscopy
PES	Photoelectron Spectroscopy

SECO	Secondary Electron Cut-Off
IP	Ionization Potential
UPS	Ultraviolet Photoelectron Spectroscopy
XPS	X-ray Photoelectron Spectroscopy
UV	Ultraviolet
ARUPS	Angle Resolved UPS
BE	Binding Energy
NEXAFS	Near-edge X-ray Absorption Fine Structure
EXAFS	Extended X-ray Absorption Fine Structure
AEY	Auger Electron Yield
PEY	Partial Electron Yield
TEY	Total Electron Yield
QCM	Quartz-Crystal-Microbalance
HOPG	Highly Orientated Pyrolytic Graphite
OLED	Organic Light-Emitting Diode
OFET	Organic Field-Effect Transistor
TFT	Thin Film Transistors
MD	Molecular Dynamics
DFT	Density Functional Theory
CVFF	Consistent Valence Force Field

Chapter 1

Introduction

Electronic device miniaturization to the size range of 0.1-10 nm (covering the atomic, molecular and macromolecular length scale) is believed to be an inevitable trend. This is driving the rapid development of nanoscience and nanotechnology over the last twenty years or so. A promising route to fabricate electronic devices and systems with nanometer dimensions is the autonomous assembly of atoms and/or molecules on atomically well-defined surfaces.[1] The spontaneous formation of the atomic and/or molecular self-assembly, is determined by a subtle balance of various adsorbate-adsorbate and adsorbate-substrate interactions. Selective coupling of the functional constituents to specific adsorption sites on supporting surfaces can facilitate the creation of long-range ordered two-dimensional (2D) nanostructures. To steer the atomic or molecular growth processes and create a wide range of surface nanostructures with desired properties, a comprehensive understanding of the mechanisms that control the surface self-assembly processes is required.

Since its invention by Binnig and Rohrer in 1981, scanning tunneling microscopy (STM) has been widely used in atomic real-space imaging and manipulation of adsorbed species on conducting or semiconducting surfaces.[2] It is

a very powerful tool in revealing surface phenomena. With STM imaging and electronic structure measurements from scanning tunneling spectroscopy (STS), the geometrical (surface morphology), electronic, and even magnetic properties of the 2D surface nanostructures as well as the supporting substrates can be imaged at the atomic scale.[3-5] A microscopic view of activated processes taking place on surfaces, such as atomic/molecular diffusion, adsorption, desorption, and chemical reactions, could be provided by STM studies.[6, 7] STM can even induce and manipulate such surface dynamic phenomena at the single atom/molecule level. Furthermore, the interplay of various interactions at different strength and length scales in self-assemblies could also be elucidated by STM.[8] This has enabled STM to become the tool of choice to study surface self-assembly and its underlying mechanisms.

Reported work on surface self-assembly has covered a wide range of atoms and/or molecules assembling in liquid, [9] ambient,[10] or vacuum environments.[11] The creations of 2D well-defined surface patterns over large areas have been demonstrated. Various covalent or non-covalent interactions have been utilized to construct surface-supported nanostructures.[12-14] However, the field of 2D self-assembly and the underlying mechanisms are not yet fully understood. Our studies on the self-assembly of various π-conjugated molecules on vacuum/solid interfaces via relatively weak non-covalent interactions, help to fill the gap in understanding. The ultimate goal is to construct robust and tunable supramolecular nanostructures over macroscopic areas with desired

functionalities. We also aim to achieve a comprehensive understanding of the mechanisms that control molecular self-assembly.

1.1 Introduction: a bottom-up approach for nanofabrication

A great deal of effort and resources have been allocated to the field of nanoscience and nanotechnology, which aims to understand and control matter at the atomic or molecular scale. The origin is often traced back to the talk "There's Plenty of Room at the Bottom", given by Richard P. Feynman in 1959.[15] In the talk, Feynman described a possible revolution in people's daily lives if we were able to manipulate individual atoms and molecules to build up nanometer scale functional systems. However, the takeoff of nano-related research and technological exploitation started from the early 1980s with two major developments. First, the invention of the STM made it possible to image and manipulate individual molecules and atoms in real space;[3, 16] second, the birth of cluster science enabled an understanding of how structural features control the properties of nanostructural materials.[17] There were also other important developments (some of them were invented before 1980s), including molecular beam epitaxy (MBE) to fabricate single crystalline inorganic and organic thin films, the synthesis and study of semiconductor nanocrystals and quantum dots,[18] and characterization tools such as high-resolution field ion microscopy (FIM), atomic force microscope (AFM), scanning electron microscopy (SEM), transmission electron microscopy (TEM), near-field scanning optical microscopy (NFSOM), low-energy electron microscopy (LEEM), and photoemission electron microscopy (PEEM). The invention and maturing of these fabrication and

characterization tools have been essential to the booming field of nanotechnology and nanoscience.

Nanostructured materials are of great interest for their unique properties as well as their great potential applications in future nano-devices. Nanostructures refer to material systems with length scale in the range of ~0.1-100 nm in at least one dimension. In the nanometer length scale, various physical phenomena, such as quantum effects and surface/interface effects, play critical roles in determining the properties and functionalities of the materials. The properties of nanostructures can be adjusted by changing their size, shape, and processing conditions, which are significantly different from bulk materials. The fabrication of nanostructured materials offers a promising route to construct nano-devices with high density of components, low cost, and high performance per device and per integrated circuit, which might meet the emerging industry needs that have thrived on continued device miniaturization.

There are two fabrication approaches used to generate nanoscale surface nanostructure arrays, which are characterized as "top-down" and "bottom-up" approaches.[19] In the top-down approach, various conventional methods are used to pattern, write or stamp a structure onto a substrate. The top-down fabrication techniques, including many photolithography and scanning beam (or maskless) lithography (e. g., electron beam, and ion beam) methods, are capable to create surface patterns down to the sub-100 nm range, but have the limitations in the atomic length scale. In contrast, the bottom-up approach relies on the cooperative interactions of small components (atoms, molecules or colloidal particles) to

assemble discrete nanoscale structures in two or three dimensions. It allows the construction of small functional systems at sub-molecular level over macroscopic areas, which has potential applications in future nano-devices, such as molecular and organic electronics, ultrahigh density data storages, biosensors, drug delivery, nano-optics, quantum computer and so on. The self-organized growth and self-assembly on well-defined surfaces (such as pre-patterned surfaces by top-down methods) have been considered as an ultimate, low-cost method for nano-manufacturing.

Bottom-up fabrication is a process involving the growth of atoms and/or molecules on substrates in vacuum, ambient atmosphere or solution environments and the subsequent formation of all kinds of surface-supported nanostructure arrays. The growth scenario is a non-equilibrium phenomenon governed by the competition between kinetics and thermodynamics. The self-assembly, which is referred to the spontaneous formation of a supramolecular architecture from its constituents without external force field,[20-23] is capable of fabricating long-range ordered supramolecular nanostructures over large macroscopic areas. The self-assembled nanostructure is stable under equilibrium conditions with minimized free-energy. In this thesis, we mainly focus on 2D molecular self-assembly under ultra-high vacuum (UHV) conditions.

1.2 Supramolecular self-assembly in two dimensions: background and literature review

1.2.1 Basic concepts in 2D surface assembly

The atomic and/or molecular self-assembly on solid surfaces involves fundamental processes of adsorption, diffusion, and interfacial and lateral interactions, all of which depend on the substrate atomic environment, adsorbate chemical nature as well as their geometrical parameters (e. g., shape, size, and symmetry).[24-26] Figure 1.1 is a schematic diagram illustrating the principles of 2D supramolecular assembly. A molecular beam of 3,4,9,10-perylenetetracarboxylic dianhydride (PTCDA) is deposited onto an atomically-flat single-crystal surface. The adsorbed molecules firstly go through thermally activated processes on the terrace, including surface migration and in-plane rotation associated with energy barriers E_m and E_{rot} respectively. That is, after adsorption, the molecules can thermally transport between different bonding sites before assembling at their formation energy minima. The migration and rotational motions largely depend on the configuration of the molecule and the substrate. The subsequent molecular recognition process may be directed by lateral intermolecular interactions between the neighboring molecules, which could be covalent bonding, van der Waals forces, hydrogen bonding, electrostatic ionic forces and so on. The typical supramolecular packing structure of a PTCDA monolayer on single crystal surfaces is depicted at the left of Figure 1.1, driving primarily by intermolecular hydrogen bonding.[26] Under nearly thermodynamic equilibrium, a uniform molecular nanostructure can be formed. In addition to the directional

intermolecular interactions, adsorbate-substrate interactions also influence the molecular self-assembly by offering specific energetically-favorable adsorption sites. The coupling of adsorbates to the substrate atomic lattice is another important factor that determines the characteristics of the supramolecular nanostructures, which is able to tune the intermolecular spacing and/or the molecular orientation. In general, adsorbate-adsorbate interactions and adsorbate-surface interactions are two key factors that determine the 2D surface self-assembly. A subtle balance of the lateral intermolecular interactions and molecule-substrate interfacial interactions allows the emergence of well-defined supramolecular architectures over macroscopic areas.

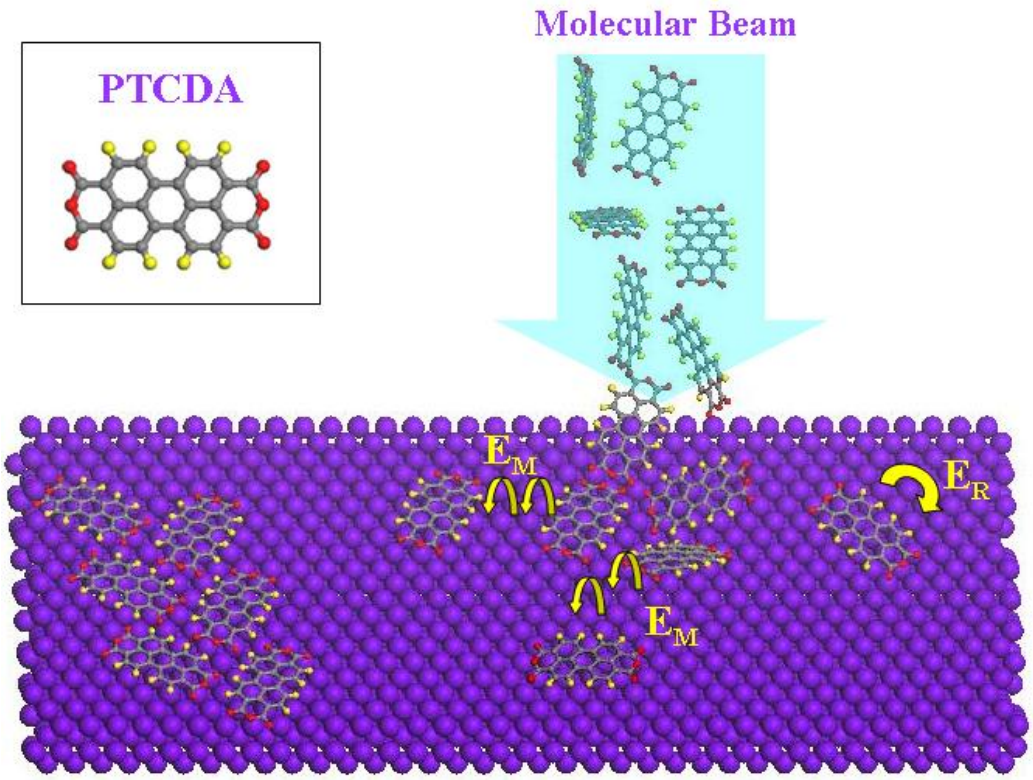

Figure 1.1 Atomic-scale view of assembly processes at surface. The substrate is exposed to a PTCDA molecular beam. The fundamental assembly processes include adsorption, thermal migration and rotational motions. The formation of the nanostructures is finally determined by direct lateral intermolecular interactions and indirect substrate mediations. The inset illustrates the

molecular structure of the PTCDA molecule, where yellow balls represent H atoms, red balls for O atoms, and gray balls for C atoms.[26]

1.2.2 The universal substrate effects

Supported surfaces play a critical role in tailoring the self-assembled molecular layers. The accommodation of incoming molecules strongly depends on the substrate reactivity, configuration and electronic properties. If molecules or atoms adsorb at solid surfaces, it can be either stabilized by chemical or physical bonding. Chemical adsorption, or chemisorption, is about the formation, and in some case (dissociative chemisorption) also the breaking, of chemical bonds. Chemisorption usually occurs on catalytically active surfaces such as Cu, Pt and Ru single crystals. For example, Cu adatoms on Cu(100) can serve as the metal cores to form coordination complexes,[27, 28] and Pt(111) surface can successfully catalyze the dehydrogenation reaction to synthesize fullerene in two dimensions.[29] In contrast, physical adsorption (physisorption) refers to unspecific adsorption based on dispersion interactions. The adsorption of large aromatic molecules on noble metal surfaces or chemically inert graphite surface usually belongs to this class.[26] Most molecular self-assemblies are constructed through non-covalent adsorbate-surface interactions with relatively low adsorption energies, and chemically reactive substrates involving high-energy covalent bonds are usually discarded.

The supporting substrates offer specific/unspecific adsorption sites to accommodate the adsorbates. At low coverage, the adsorbates may preferentially decorate surface defect sites such as steps, kinks or vacancies, because the

electron redistributions at these defects could affect the adsorption (or desorption), diffusion, and chemical reactivity of the adsorbates.[30-32] Depending on the electronic structure of the adsorbates, the electronic rich/deficient regions are preferred. For example, as a type of defect with definite structure, steps have an asymmetric electronic structure because of the formation of a local electronic dipole at the step sites.[33] Electron-donor-type molecules such as benzene prefer to bind to the electron-poor region at the upper step edges,[34] while electron-acceptor-type molecules such as teracyanoquinonedimethane (TCNQ) are found to reside at the lower edges of steps.[35] Other special adsorption geometries such as π-conjugated molecules lying across step edges or at the elbow position on Au(111) reconstructed surface have also been reported in literature.[36, 37]

When the molecules are bound to a surface, they can perturb the substrate electronic and strain field and further mediate the interactions between them.[11, 38, 39] The so-called indirect substrate-mediated interactions can be either of elastic or electronic origin, which are oscillatory in nature and typically extend in the 10 Å range.[11, 38] Over the intermediate range, the interactions are strong enough to influence the arrangement of adsorbates at surfaces. Reported studies cover many different atoms (e. g., Cu and Ce) and organic molecules adsorbed on close-packed noble-metal surfaces and the formations of surface structures with short-range or long-range ordering.[40-44] An outstanding example is the formation of one dimensional, unidirectional pentacene rows on Cu(110) surface, whose inter-chain spacing is evidently mediated by the oscillatory modulation of the adsorption energy due to charge-density waves related to a surface state.[43] Similar to the

interactions mediated by surface-state electrons, surface strain-field perturbations can also create long-range ordering on the 2D assemblied nanostructures.[45-47] With higher thermal activation, strong adsorbate-substrate interactions could even induce reconstructions of the substrate lattice, which further complicate the binding processes.[48, 49]

Other factors that can influence the supramolecular ordering on surface include the substrate symmetry, chirality, atomic lattice length and so on. Several studies have indicated that the self-assembled nanostructures can somehow reflect the two-fold, three-fold or four-fold symmetry of the underlying substrates.[50] The assembly of symmetric molecules on surfaces can become chiral because the adsorption occurs on a high-index chiral metal surface,[51, 52] or 2D confinement removes mirror symmetry in the plane of the substrate.[44] The coupling of adsorbates to the substrate atomic lattice could lead to a so-called 'point-on-line' registry for conjugated organic molecules on metal surfaces.[26, 53, 54] The term point-on-line registry refers to lattice relationships where all lattice points of the superstructure are located on lattice lines, but not lattice points, of the substrate.

The adsorbate-substrate interaction plays a vital role, though not always the dominant part, in determining the binding and ordering of 2D nano-patterns on surfaces. Single crystal substrates are often considered static checkerboards that simply provide bonding and specific adsorption sites to the molecules. However, when large organic molecules adsorb on metal surfaces, the complexity of the molecule-substrate interactions often increases dramatically. To minimize the substrate effect, atomically flat and chemically inert substrates are preferred, and

HOPG and Au(111) are two of the most frequently used substrates for their chemical inertness and ease of preparation. In contrast, pre-patterned surfaces, such as boron nitride (BN) nanomesh,[55, 56] carbon nanomesh on silicon carbide (SiC),[57] and supramolecular nanoporous[58-64], or non-porous surface templates,[65] can provide specific adsorption sites to accommodate the incoming species and hence facilitate the formation of nanostructures with designed patterns. The selection of the substrates is critical in achieving our objectives.

1.2.3 Directionality of lateral adsorbate-adsorbate interactions

We now turn to the directionality of lateral adsorbate-adsorbate interactions in 2D self-assembly. The 2D self-assembly is determined by the competition between the adsorbate-adsorbate interactions and adsorbate-surface interactions, where the former usually dominate over the later when the assembly happens on chemically inert surfaces. In addition to covalent synthesis, non-covalent synthesis using relatively weak intermolecular interactions, such as van der Waals forces, hydrogen bonding, electrostatic ionic forces and dipole-dipole interactions, has advantages in the creation of long-range ordered superstructures.[66-69] Most 2D supramolecular self-assemblies reported are formed by a single component. To increase the functionality and tunability of the nanostructures, increasing effort has recently been devoted to the construction of bi- or multi- component superstructures.[58-60, 70-72] For the multi-component assembly, the interaction characteristics of all the components must balance in order to obtain an ordered complex. A wide range of 2D regular networks have been successfully fabricated.

We will demonstrate the roles played by the directional and selective intermolecular hydrogen bonding, metal-ligand interactions (coordination bonding), as well as covalent bonding in the 2D self-assembly. A characteristic comparison of these interactions with van der Waals force is shown in Table 1.1.[13] The van der Waals force is rather weak and non-directional, but it universally exists in every material system. The directional hydrogen bonding, metal-ligand interaction (coordination bonding), and covalent bonding have increasing interaction strength in guiding surface assemblies. However, they are only available in specific systems. For example, the utilization of the hydrogen bonding requires the component molecules to offer electronegative (e. g., O) or electropositive (e. g., H) peripheral atoms; and the metal-ligand interaction only exists in the system comprising specific metal atoms and organic molecules with specific functional groups.

Interaction type	Interaction energy (kJ mol^{-1})	Directionality
van der Waals force	2 –10	No
Hydrogen bonding	5 – 70	Yes
Coordination interaction	50 – 200	Yes
Covalent bonding	>300	Yes

Table 1.1 A characteristic comparison of several typical non-covalent interactions.[13]

A number of studies on one- and bi-component 2D supramolecular networks driven by hydrogen bonding have been published in the last decade.[59, 61, 73-82] The molecules that form the hydrogen-bonded structures have special functional groups, such as carbonyl groups, or sulfur, oxygen, nitrogen, hydrogen, or

fluorine atoms attached to aromatic rings, to offer electronegative or electropositive peripheral atoms in the hydrogen bonding formation. One of the first breakthroughs in constructing large surface patterns came from the Beton Champness and coworkers, who created a hexagonal bi-component network by the co-deposition of 3,4,9,10-perylenetetracarboxylic diimide (PTCDI) and 2,4,6-triamino-1,3,5-triazine (melamine) on Ag-terminated silicon surface under UHV conditions.[59] The formation of the hexagonal PTCDI-melamine network has been revealed to be driven by the triple hydrogen bonding, N-H···N-C and N-H···O-C, between the PTCDI and melamine molecules. From then on, the fabrication of similar open networks via multiple intermolecular hydrogen bonds were reported from time to time by varying the molecular components, relative molecular ratio, and also the supporting substrate.[60, 76-82] Although the use of weak interactions has obvious disadvantages with regards to thermal stability, it allows other weak interactions – such as mediated effects of the substrate – to further tailor the supramolecular pattern leading to long-range ordering.

To further increase of the structural stability, the coordination of organic molecules by transition metal atoms has been used for the fabrication of surface-supported metal-organic coordination networks. A wide range of metal centers (e. g., cobalt,[83] copper,[84-86] iron,[87-89] and nickel[90]) and molecular linkers (e. g., carboxylic acid,[86, 91] hydroxyl,[89] cyano,[83, 85] and pyridine[92]) can be used to form rigid metal-organic networks. The fabricated coordination networks on metal surfaces can adopt a variety of sizes and shapes. The pore dimensions of metal-organic networks can be scaled by the length of the employed molecular linker.

As demonstrated by Kern, Barth, and colleagues, 2D honeycomb networks were constructed on Ag(111) from cobalt atoms and various ditopic dicarbonitrile-polyphenyl molecules with three, four or five phenyl rings, and the dimensions of the resultant pores were directly tailored by the ligand molecular length.[83] Square coordination networks on Ag(111), Ag(100) and Cu(100) formed by the use of 5,5'-bis(4-pyridyl)(2,2'-bipyrimidine) as a ligand and copper atoms as coordination centres were also fabricated by Kern and co-workers.[84] The metal-organic coordinated networks offer a promising approach for the design and construction of 2D surface patterns with desired functionalities. The multi-component systems formed through pure metal-ligand coordination are still in early stage of research.

Covalent bonds can also facilitate the formation of 2D supramolecular structures. The first work describing the formation of 2D covalent-bonded porous networks on surfaces is reported by Grill and coworkers in 2007.[94] In their work, the square tetraphenylporphyrins that carried bromine on one, two or four sides were covalently bound together to form dimers, 1D molecular rows and 2D extended networks at the Au(111) surfaces in vacuum. Similar surface polymerizations of single-component organic molecular layers at vacuum-solid interfaces were demonstrated by several groups.[95-100] For example, Grill and colleagues subsequently showed that linear polyfluorenes could be produced at a Au(111) surface in a similar manner and used as model molecular wires;[98] Rosei and co-workers demonstrated the polymerization of para- and meta-diiodobenzene on Cu(100) to form straight and meandering polyphenyl chains.[99]

The creation of covalent bonded networks relies on the polymerization reactions of deposited molecules. The progress in covalent-bonded surface patterns is very appealing, because it provides a promising approach for the construction of highly rigid organic nanostructures with high thermal stability. However, this strategy faces a practical challenge associated with the evaporation of adsorbates onto substrates in vacuum: because of their high reactivity and large masses, the reactants maybe polymerize during heating before a sufficient vapor pressure for the deposition is reached.

1.3 Objective and scope of this investigation

Numerous studies of atomic and/or molecular self-assemblies have been carried out in vacuum, ambient atmosphere or solution circumstances. However, the mechanisms that control molecular self-assembly are not yet fully understood. The ultimate goal of this study is to construct tunable and robust nanostructures at the vacuum/solid interface. To fabricate supramolecular architectures with desired patterns, we need to carefully select and control the molecular building blocks and supporting substrates. A comprehensive understanding of the underlying principles that determine the formations of 2D molecular self-assemblies is also needed.

Chemically inert substrates, such as graphite and single-crystal noble-metal surfaces, are commonly preferred to minimize the substrate effect. The adsorption of organic molecules on metal substrates are usually stabilized through the strong interfacial coupling between the metal surface electrons and molecular π-orbitals,

which can lock the adsorbed molecules at specific sites due to the corrugation of the potential energy surface of the metal substrates.[11] This could restrict the lateral degrees of freedom of the adsorbed molecules and hence reduce the structural tunability of molecular nanostructures on metal surfaces. The adsorption of large organic molecules on metal surface also can increase the complexity of the molecule-substrate interactions and prevent us from obtaining a comprehensive understanding of the interplay of various kinds of intermolecular interactions in molecular self-assembly. Herein, the inert graphite substrate is selected for its smooth potential energy surface and relatively weak interfacial interactions with adsorbed molecules. In this thesis, most of our studies are carried out on graphite surfaces.

Various covalent/non-covalent intermolecular interactions can successfully steer the formation of long-range ordered molecular arrays. 2D supramolecular arrays stabilized through relatively weak intermolecular interactions, such as intermolecular C-F···H-C hydrogen bonding, and dipole-dipole interactions, are of interest in this thesis. Organic π-conjugated molecules, including copper hexadecafluorophthalocyanine (F_{16}CuPc), copper phthalocyanine (CuPc), chloroaluminum phtholocyanine (ClAlPc), di-indenoperylene (DIP), *p*-sexiphenyl (6P), and pentacene, which are widely used in organic semiconductor devices, are selected as prototype molecules to construct various single or binary component nanostructures. Our approach represents a promising route to construct robust organic molecular arrays whose 2D arrangements can be controlled by the

molecular functionalities and other experimental parameters (e. g., coverage and relative molecular ratio for bi-component systems).

This thesis will be organized as follows. Chapter 2 provides an overview on the experimental methods, where operating principles of the characterization tools (both STM and photoemission measurements) are described. Experimental results and discussions are presented in Chapters 3 to 6. Chapter 3 investigates the epitaxial growth of ultra-thin organic molecular films, including F_{16}CuPc and DIP thin films on graphite and/or SiO_2. In chapter 4, we present the efficient bottom-up approach to the design and fabrication of tunable 2D binary molecular networks directed by weak hydrogen bonding on graphite surfaces, demonstrated with binary combinations of molecules with different geometries, namely, F_{16}CuPc with CuPc, 6P, pentacene, and DIP respectively. Some of the fabricated binary networks can serve as effective surface nanotemplates to selectively accommodate guest molecules (F_{16}CuPc) which further assemble to 2^{nd} layer supramolecular patterns, and this is discussed in chapter 5. Finally, the self-assembly of the dipolar molecule, ClAlPc on graphite, is investigated in chapter 6; the competition between intermolecular dipole-dipole interaction and molecule-substrate interactions is discussed. The reversible manipulation of single ClAlPc molecules by the STM tip is also demonstrated. Our studies advance the understanding and development of 2D molecular self-assembly and their potential applications in nano-devices.

Reference:

[1] J. V. Barth, G. Costantini, K. Kern, *Nature* **437**, 671-679 (2005).

[2] G. Binnig, H. Rohrer, Ch. Gerber, E. Weibel, *Appl. Phys. Lett.***40**, 178-180 (1982).

[3] G. Binnig, H. Rohrer, *Rev. Mod. Phys.* **59**, 615-625 (1987).

[4] R. Otero, F. Rosei, F. Besenbacher, *Annu. Rev. Phys. Chem.* **57**, 497–525 (2006).

[5] W. Wulfhekel, J. Kirschner, *Annu. Rev. Mater. Res.* **37**, 69–91 (2007).

[6] R. A. Wolkow, *Annu. Rev. Phys. Chem.* **50**, 413-441 (1999), and reference therein.

[7] H. Brune, *Surf. Sci. Rep.* **31**, 125-225 (1998), and reference therein.

[8] F. Vonau, D. Suhr, D. Aubel, L. Bouteiller, G. Reiter, L. Simon, *Phys. Rev. Lett.* **94**, 066103 (2005).

[9] S. De Feyter, F. C. De Schryver, *Chem. Soc. Rev.* **32**, 139-150 (2003).

[10] X. H. Qi, C. Wang, Q. D. Zeng, B. Xu, S. X. Yin, H. N. Wang, S D. Xu, C. L. Bai, *J. Am. Chem. Soc.* **122**, 5550-5556 (2000).

[11] J. V. Barth, *Annu. Rev. Phys. Chem.* 58, 375-407 (2007).

[12] D. Bonifazi, S. Mohnani, A. Llanes-Pallas, *Chem. Eur. J.* **15**, 7004-7025 (2009).

[13] H. Liang, Y. He, Y. Ye, X. Xu, F. Cheng, W. Sun, X. Shao, Y. Wang, J. Li, K. Wu, *Coordination Chem. Rev.* **253**, 2959-2979 (2009).

[14] L. Bartels, *Nat. Chem.* **2**, 87-95 (2010).

[15] R. P. Feynman, *Eng. Sci.* **23**, 22-36 (1960).

[16] D. M. Eigler, E. K. Schweizer, *Nature* **344**, 524-526 (1990).

[17] R. P. Andres, R. S. Averback, W. L. Brown, L. E. Brus, W. A. Goddard, A. Kaldor, S. G. Louie, M. Moscovits, P. S. Peercy, S. J. Riley, R. W. Siegel, F. Spaepen, Y. Wang, *J. Mater. Res.* **4**, 704-736 (1989).

[18] A. Rogach (editor), *Semiconductor nanocrystal quantum dots: synthesis, assembly, spectroscopy and applications* (Springer, 2008).

[19] B. D. Gates. Q. Xu, M. Stewart, D. Ryan, C. G. Willson, G. M. Whitesides, *Chem. Rev.* **105**, 1171-1196 (2005).

[20] J. S. Lindsey, *New J. Chem.* **15**, 153–180 (1991).

[21] G. M. Whitesides, J. P. Mathias, C. T. Seto, *Science* **254**, 1312–1319 (1991).

[22] D. Philp, J. F. Stoddart, *Angew. Chem. Int. Ed.* **35**, 1154–1196 (1996).

[23] J.-M. Lehn, *Angew. Chem. Int. Ed.* **29**, 1304–1319 (1990).

[24] J. K. Gimzewski, C. Joachim, *Science* **283**.1683–1688 (1999).

[25] S. M. Barlow, R. Raval R. *Surf. Sci. Rep.* **50**, 201–341 (2003).

[26] F. S. Tautz, *Prog. Surf. Sci.* **82**, 479–520 (2007).

[27] L. Nian, A. Dmitriev, J. Weckesser, J. V. Barth, K. Kern, *Angew. Chem. Int. Ed.* **41**, 4779-4783 (2002).

[28] S. L. Tait, A. Langner, N. Lin, S. Stepanow, C. Rajadurai, M. Ruben, K. Kern, J. *Phys. Chem. C* **111**, 10982-10987 (2007).

[29] G. Otero, G. Biddau, C. Snchez-Sanchez, R. Caillard, M. F. Lopez, C. Rogero, F. J. Palomares, N. Cabello, M. A. Basanta, J. Ortega, J. Mendez, A. M. Echavarren, R. Perez, B. Gomez-Lor, J. A. Martın-Gago, *Nature* 454, 865-868 (2008).

[30] T. Zambelli, P. Jiang, J. Lagoute, S. E. Grillo, S. Gauthier, A. Gourdon, C. Joachim, *Phys. Rev. B* **66**, 075410 (2002).

[31] A. Kuhnle, T. R. Linderoth, F. Besenbacher, J. *Am. Chem, Soc.* **128**, 1076-1077 (2006).

[32] O. Bikondoa, C. L. Pang, R. Ithnin, C. A. Muryn, H. Onishi, G. Thornton, *Nat. Mater.* **5**, 189-192 (2006).

[33] R. Smoluchowski, *Phys. Rev.* **60**, 661-674 (1941).

[34] M. M. Kamna, S. J. Stranick, P. S. Weiss, *Science* **274**, 118– 119 (1996).

[35] M. M. Kamna, T. M. Graham, J. C. Love, P. S. Weiss, *Surf. Sci.* **419**, 12–23 (1998).

[36] P. Ruffieux, K. Palotas, O. Gröning, D. Wasserfallen, K. Müllen, W.A. Hofer, P. Gröning, R. Fasel, *J. Am. Chem. Soc.* **129** 5007-5011 (2007).

[37] L. Gao, Q. Liu, Y. Y. Zhang, N. Jiang, H. G. Zhang, Z. H. Cheng, W. F. Qiu, S. X. Du, Y. Q. Liu, W. A. Hofer, H. J. Gao, *Phys. Rev. Lett.* **101**, 197209 (2008).

[38] M. L. Merrick, W. Luo, K. A. Fichthorn, *Prog. Surf. Sci.* **72**, 117-134 (2003).

[39] E. C. H. Sykes, P. Han, S. A. Kandel, K. F. Kelly, G. S. Mccarty, P. S. Weiss, *Acc. Chem. Res.* **36**, 945-953 (2003).

[40] F. Silly, M. Pivetta, M. Ternes, F, Patthey, J. P. Pelz, W. D. Schneider, *Phys. Rev. Lett.* **92**, 016101(2004).

[41] J. Repp, F. Moresco, G. Meyer, K. H. Rieder, P. Hyldgaard, M. Persson, *Phys. Rev. Lett.* **85**, 2981-2984 (2000).

[42] N. Knorr, H. Brune, M. Epple, A. Hirstein, M. A. Schneider, K. Kern, *Phys. Rev. B* **65**, 115420-115421 (2002).

[43] S. Lukas, G. Witte, Ch. Wöll, *Phys. Rev. Lett.* **88**, 028301(2002).

[44] J. V. Barth, J. Weckesser, G. Trimarchi, M. Vladimirova, A. De Vita, C. Cai, H. Brune, P. Günter, K. Kern, *J. Am. Chem. Soc.* **124**, 7991–8000 (2002).

[45] J. V. Barth, G. Costantini, K. Kern, *Nature* **437**, 671–679 (2005).

[46] J. V. Barth, H. Brune, G. Ertl, R. J. Behm, *Phys. Rev. B* **42**, 9307–9318 (1990).

[47] K. Kern, H. Niehus, A. Schatz, P. Zeppenfeld, J. George, G. Comsa, *Phys. Rev. Lett.* **67**, 855–858 (1991).

[48] M. Schunack, L. Petersen, A. Kuhnle, E. Lægsgaard, I. Steensga, I. Johannsen, F. Besenbacher, *Phys. Rev. Lett.* **86**, 456–459 (2001).

[49] M, Stengel, A. De Vita, A. Baldereschi, *Phys. Rev. Lett.* **91**, 166101 (2005).

[50] F. Rosei, M Schunack, Y. Naitoh, P. Jiang, A. Gourdon, E. Laegsgaard, I.Stensgaard, C. Joachim, F. Besenbacher, *Prog. Surf. Sci.* **71**, 95–146 (2003).

[51] A. Kuhnle, T. R. Linderoth, F. Besenbacher, *J. Am. Chem. Soc.* **128**, 1076-1077 (2006).

[52] T. Greber, Z. Sljivancanin, R. Schillinger, J. Wider, B. Hammer, *Phys. ReV. Lett*. **96**, 056103 (2006).

[53] D. E. Hooks, T. Fritz, M. D. Ward, *Adv. Mater*. **13**, 227–241 (2001).

[54] S. C. B. Mannsfeld, T. Fritz, *Phys. Rev. B* **69**, 075416 (2004).

[55] H. Dil, J. Lobo-Checa, R. Laskowski, P. Blaha, S. Berner, J. Osterwalder, T. Greber, *Science* **319**, 1824-1826 (2008).

[56] M. Corso, W. Auwärter, M. Muntwiler, A. Tamai, T. Greber, J. Osterwalder, *Science* **303**, 217-220 (2004).

[57] W. Chen, A. T. S. Wee, *J. Phys. D: Appl. Phys.* **40,** 6287-6299 (2007).

[58] S. Stepanow, M. Lingenfelder, A. Dmitriev, H. Spillmann, E. Delvigne, N. Lin, X. B. Deng, C. Z. Cai, J. V. Barth, K. Kern, *Nature Mater.* **3**, 229-233 (2004).

[59] J. A. Theobald, N. S. Oxtoby, M. A. Phillips, N. R. Champness, P. H. Beton, *Nature* **424**, 1029-1031 (2003).

[60] P. A. Staniec, L. M. A. Perdigao, A. Saywell, N. R. Champness, P. H. Beton, *ChemPhysChem* **8**, 2177-2181 (2007).

[61] L. M. A. Perdigao, A. Saywell, G. N. Fontes, P. A. Staniec, G. Goretzki, A. G. Phillips, N. R. Champness, P. H. Beton, *Chem. Eur. J.* **14**, 7600-7607 (2008).

[62] R. Madueno, M. T. Raisanen, C. Silien, M. Buck, *Nature* **454**, 618 (2008).

[63] L. Piot, F. Silly, L. Tortech, Y. Nicolas, P. Blanchard, J. Roncali, D. Fichou, *J. Am. Chem. Soc.* **131**, 12864-12865 (2009).

[64] H. L. Zhang, W. Chen, L. Chen, H. Huang, L. Chen, A. T. S. Wee, *J. Am. Chem. Soc.* **130**, 2702-2703 (2008).

[65] O. Ivasenko, J. M. MacLeod, K. Yu. Chernichenko, E. S. Balenkova, R. V. Shpanchenko, V. G. Nenajdenko, F. Rosei, D. F. Perepichka, *Chem. Commun.*, 1192–1194 (2009).

[66] J. M. Lehn, *Angew. Chem. Int. Ed.* **29**, 1304-1319 (1990).

[67] L. J. Prins, D. N. Reinhoudt, P. Timmerman, *Angew. Chem. Int. Ed.* **40**, 2382-2426 (2001).

[68] C. F. J. Faul, M. Antonietti, *Adv. Mater.* **15**, 673-683 (2003).

[69] S. De Feyter, F. C. De Schryver, *Chem. Soc. Rev.* **32**, 139-150 (2003).

[70] L. M. A. Perdigão, N. R. Champness, P. H. Beton, *Chem. Commun.*, 538-540 (2006).

[71] W. Xu, M. D. Dong, H. Gersen, E. Rauls, S. Vazquez-Campos, M. Crego-Calama, D. N. Reinhoudt, I. Stensgaard, E. Laegsgaard, T. R. Linderoth, F. Besenbacher, *Small* **3**, 854-858 (2007).

[72] S. B. Lei, M. Surin, K. Tahara, J. Adisoejoso, R. Lazzaroni, Y. Tobe, S. De Feyter, *Nano Lett.* **8**, 2541-2546 (2008).

[73] M. Stöhr, M. Wahl, C. H. Galka, T. Riehm, T. A. Jung, L. H. Gade, *Angew. Chem. Int. Ed.* **44**, 7394-7398 (2005).

[74] G. Pawin, K. L. Wong, K. Y. Kwon, L. Bartels, *Science* **313**, 961–962 (2006).

[75] U. Schlickum, R. Decker, F. Klappenberger, G. Zoppellaro, S. Klyatskaya, W. Auwarter, S. Neppl, K. Kern, H. Brune, M. Ruben, J. V. Barth, *J. Am. Chem. Soc.* **130**, 11778–11782 (2008).

[76] K. Suto, S. Yoshimoto, K. Itaya, *J. Am. Chem. Soc.* **125**, 14976–14977 (2003).

[77] J. C. Swarbrick, B. L. Rogers, N. R. Champness, P. H. Beton, *J. Phys. Chem. B* **110**, 6110-6114 (2006).

[78] S. Yoshimoto, Y. Honda, O. Ito, K. Itaya, *J. Am. Chem. Soc.* **130,** 1085–1092 (2008)**.**

[79] F. Silly, A. Q. Shaw, M. R. Castell, G. A. D. Briggs, *Chem. Commun.*, 1907-1909 (2008).

[80] J. Ma, B. L. Rogers, M. J. Humphry, D. J. Ring, G. Goretzki, N. R. Champness, P. H. Beton, *J. Phys. Chem. B* **110**, 12207-12210 (2006).

[81] S. H. Park, C. Pistol, S. J. Ahn, J. H. Reif, A. R. Lebeck, C. Dwyer, T. H. LaBean, *Angew. Chem. Int. Ed.* **45**, 735 –739 (2006).

[82] Q. Chen, N. V. Richardson, *Nat. Mater.* **2**, 324-328 (2003).

[83] U. Schlickum, R. Decker, F. Klappenberger, G. Zoppellaro, S. Klyatskaya, M. Ruben, I. Silanes, A. Arnau, K. Kern, H. Brune, J. V. Barth, *Nano Lett.* **7**, 3813-3817 (2007).

[84] S. L. Tait, A. Langner, N. Lin, R. Chandrasekar, O. Fuhr, M. Ruben, K. Kern, *Chem. Phys. Chem.* **9**, 2495–2499 (2008).

[85] G. Pawin, K. L. Wong, D. Kim, D. Sun, L. Bartels, S. Hong, T. S. Rahman, R. Carp, M. Marsella, *Angew. Chem. Int. Ed.* **47**, 8442–8445 (2008).

[86] N. Lin, A. Dmitriev, J. Weckesser, J. V. Barth, K. Kern, *Angew. Chem. Int. Ed.* **41**, 4779–4783 (2002).

[87] S. Stepanow, M. Lingenfelder, A. Dmitriev, H. Spillmann, E. Delvigne, N. Lin, X. Deng, C. Cai, J. V. Barth, K. Kern, *Nat. Mater.* **3**, 229 - 233 (2004).

[88] A. Langner, S. L. Tait, N. Lin, C. Rajadurai, M. Ruben, K. Kern, *Proc. Natl Acad. Sci. USA* **104**, 17927–17930 (2007).

[89] S. Stepanow, N. Lin, D. Payer, U. Schlickum, F. Klappenberger, G.

Zoppellaro, M. Ruben, H. Brune, J. V. Barth, K. Kern, *Angew. Chem. Int. Ed.* **46**, 710–713 (2007).

[90] S. Jensen, C. J. Baddeley, *J. Phys. Chem. C* **112**, 15439–15448 (2008).

[91] A. Dmitriev, H. Spillmann, N. Lin, J. V. Barth, K. Kern, *Angew. Chem. Int. Ed.* **42**, 2670–2673 (2003).

[92] A. Langner, S. L.Tait, N. Lin, R. Chandrasekar, M. Ruben, K. Kern, *Angew. Chem. Int. Ed.* **47**, 8835–8838 (2008).

[93] L. Grill, M. Dyer, L. Lafferentz, M. Persson, M. V. Peters, S. Hecht, *Nat. Nanotechnol.* **2**, 687-691 (2007).

[94] N. A. A. Zwaneveld, R. Pawlak, M. Abel, D. Catalin, D. Gigmes, D. Bertin, L. Porte, *J. Am. Chem. Soc.* **130**, 6678-6679 (2008).

[95] S. Weigelt, C. Bombis, C. Busse, M. M. Knudsen, K. V. Gothelf, E. Laegsgaard, F. Besenbacher, T. R. Linderoth, *ACS Nano* **2**, 651-660 (2008).

[96] S. Weigelt, C. Busse, M. M. Knudsen, K. V. Gothelf, T. Strunskus, C. Wöll, M. Dahlboom, B. Hammer, E. Laegsgaard, F. Besenbacher, T. R. Linderoth, *Angew. Chem.Int. Ed.* **46**, 9227-9230 (2007).

[97] S. Weigelt, C. Busse, C. Bombis, M. M. Knudsen, K. V. Gothelf, E. Laegsgaard, F. Besenbacher, T. R. Linderoth, *Angew. Chem. Int. Ed.* **47**, 4406-4410 (2008).

[98] L. Laferentz, F. Ample, H. Yu, S. Hecht, C. Joachim, L. Grill, *Science* **323**, 1193–1197 (2009).

[99] J. A. Lipton-Dufn, O. Ivasenko, D. F. Perepichka, F. Rosei, *Small* **5**, 592–597 (2009).

[100] S. Boz, M. Stohr, U. Soydaner, M. Mayor, *Angew. Chem. Int. Ed.* **48**, 3179–3183 (2009).

Chapter 2

Experimental Methods

2.1 Scanning tunneling microscopy

The first STM was invented by G. Binnig, H. Rohrer and coworkers at the IBM Zürich Research Laboratory in 1981.[1] Only five years later, the STM earned its inventors the Nobel Prize in Physics in 1986. STM has since been a very powerful tool for atomic resolution real-space imaging to study surface phenomena. The resolution of STM images can easy resolve the atomic scale, i.e., 0.1 nm laterally and 0.01 nm in depth. It can be performed not only in ultra high vacuum but also in air, water, and various other liquids or gas ambient, and at temperatures ranging from near zero Kelvin to a few hundred degrees Celsius. Besides real-space imaging and electronic structure measurements, the STM is also capable of manipulating single atoms or molecules, and thereby building nanometer-scale structures with desired properties.[2-12] Furthermore, localized chemical reactions or dynamic motions can be induced and controlled by the STM at the atomic length scale, which have potential applications in supramolecular arrays in future nano-devices.[13-16] With STM measurements, we are able to study the morphological and electronic properties of 2D surface nanostructures, and also to monitor

various surface phenomena caused by thermal, optical, plasmon excitation or STM tip at single molecular level.

2.1.1 Operating principle of STM

A STM system is usually constructed with a scanning tip, piezoelectric controlled *xyz* scanner, coarse sample-to-tip controller, vibration isolation system, and a computer for data storage and display.[17] The schematic drawing in Figure 2.1 shows the setup and working principle of the STM.[18] The probe tip, usually made of tungsten (W) or platinum-iridium (Pt-Ir) alloy, is attached to a piezoelectric transducer which controls the *x*, *y*, *z* positioning. Being driven by the coarse controller firstly and piezoelectric *z* scanner subsequently, the tip can be brought sufficiently close to the sample (typically 4 ~ 10 Å) by detecting the tunneling current via a feed-back circuit. When a small voltage bias (tens of mV to several V) is between the tip and sample, electrons can tunnel through the vacuum between them. Since the tunneling current depends on the tip-sample separation *Z* as well as the local density of states of the sample surface, a 2D image containing both morphological and electronic information can be obtained by recording the tunneling current (*I*) as a function of the tip position (*x* and *y*). The recorded 2D STM images can be saved and displayed in the computer, and different color-scales could be adopted for easy visualization. In order to achieve good resolution, vibration isolation is essential to reduce the background noise from environmental vibrations.

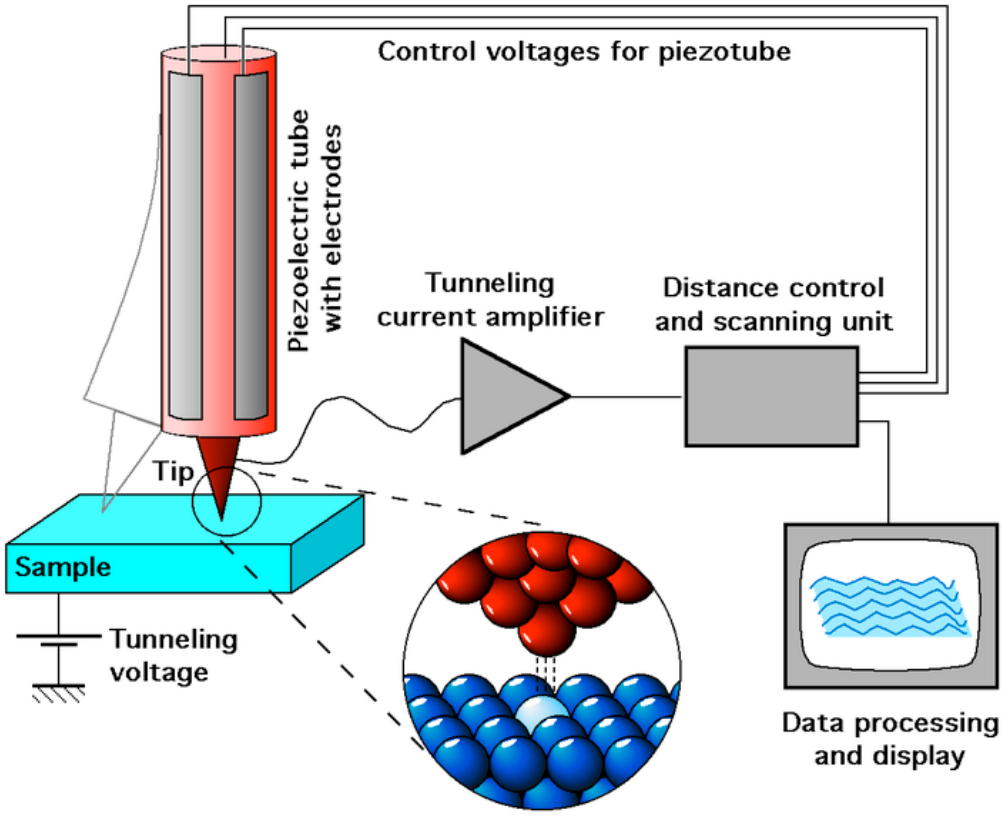

Figure 2.1 STM system setup and working principle (free copyright from Wikipedia website: http://en.wikipedia.org/wiki/Scanning_tunneling_microscope).[18]

There are two operating modes used in STM, namely constant current mode and constant height mode (shown in Figure 2.2). The constant current mode is the most commonly used, in which the feedback system keeps the tunneling current at a pre-set value by adjusting the tip-sample separation via a piezoelectric driver (Figure 2.2a). By recording the height of the tip $Z(x, y)$ as a function of position, a 2D topographical image including electronic information can be obtained.[19] In constant height mode, the voltage and height are both held constant while the variations in the tunneling current are recorded as a function of location (Figure 2.2b).[19] A faster scan rate can be achieved in this mode, as the response time of

the feed back loop is largely shortened or the feedback loop is turned off completely. However, the disadvantage of the constant height mode is the surface has to be very flat since there is a possibility of the tip crashing into surface asperities.[19] In both constant current and height modes, information of the surface topography as well as density of state is recorded.

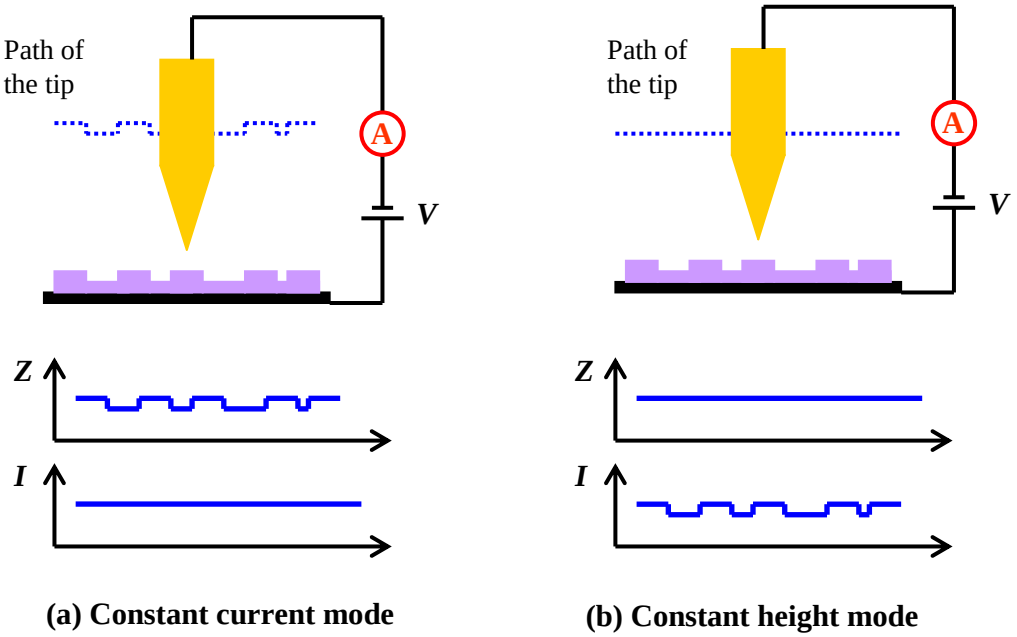

(a) Constant current mode **(b) Constant height mode**

Figure 2.2 Two operation modes used in STM system: (a) constant current mode and (b) constant height mode.

2.1.2 Theory of electron tunneling

The underlying principle of STM is based on the quantum mechanical phenomenon of tunneling, which has been known for more than eighty years. A simple understanding of the transmission of electrons through the vacuum barrier between the tip and the sample can be understood using a simplified 1D barrier

model.[20] As shown in the schematic drawing of Figure 2.3, the tip is considered a free electron metal with a constant density of states, and the sample contains a distribution of surface density of states as shown. When the tip and the sample are isolated far from each other, they have the same vacuum levels but different Fermi energies, which lie below the vacuum level by an energy equivalent to their respective work functions ϕ_T and ϕ_S (Figure 2.3a). The quantum-mechanical wave functions of the electrons are periodic in the solid (either tip or sample here) and decay exponentially into the vacuum region according to $\Psi = A\exp(-\kappa Z)$, where $\kappa = \left(2\sqrt{2m(\phi - E)}\right)/\hbar$ is the inverse decay length, Z is the distance perpendicular to the surface and E is the electron energy with respect to the Fermi level. This solution is derived from the Schrödinger equation for a 1D square barrier. If the tip and sample are brought closed together (few Å apart) and in thermodynamic equilibrium, their Fermi levels must align (Figure 2.3b). Electrons attempting to travel from sample to tip (or *vice versa*) will encounter an energy barrier ϕ_T (or ϕ_S), but the quantum tunneling could occur if the barrier is sufficiently narrow. When a voltage is applied to the tip (or sample), its energy levels will be rigidly shifted upward (negative bias, Figure 2.3c) or downward (positive bias, Figure 2.3d) by an amount $|eV|$. At negative tip bias (Figure 2.3c), the detected current arises from the electrons that tunnel from occupied states of the tip into unoccupied states of the sample; at positive tip bias (Figure 2.3d), the electrons tunnel from occupied states of the sample into unoccupied states of the tip. When the bias voltage is applied to the sample, the situations are reserved. The STM image obtained by scanning the tip line by line across the surface is a

convolution of both the local electronic density of states and geometrical morphology of the surface.

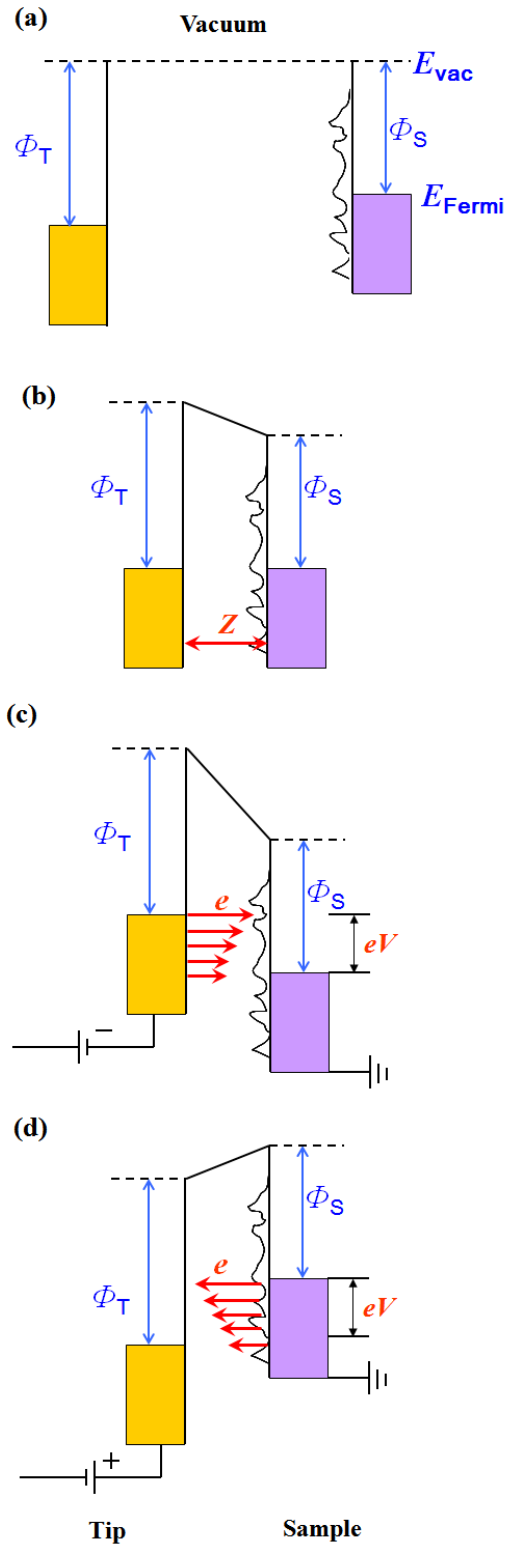

Figure 2.3 Schematic drawing of the energy level diagrams for electron tunneling in a simplified 1D barrier. (a) and (b) display the tip and sample system with large and small vacuum gap respectively; (c) and (d) demonstrate the tunneling processes at negative tip bias and positive tip bias respectively.

2.1. 3 Electronic structure measurements

The STM image is a contour map of constant surface local density of states (LDOS).[21] For any given lateral position of the tip above the sample, the tunneling current (I) is determined by the tip-sample separation (Z) and the electronic structure of the sample and tip. When a voltage V is applied to the tip (or sample), only the states lying between E_F and E_F+eV contribute to the detected tunneling current. That is, the sign and magnitude of the applied voltage determine which states contribute to the resulting topographic images. Thus, quantitative information regarding the symmetry properties and the spatial distribution of electronic states can be measured by changing the applied voltage. Information about sample electronic structures can be obtained in different ways. Voltage-dependent STM imaging is the simplest method to obtain electronic information by acquiring conventional STM topographic images at different applied voltages. More complete information can be obtained from STS measurements over a wider energy range at a specific location, including the measurements of local conductivity I-V, differential conductivity $\mathrm{d}I/\mathrm{d}V$ as a function of V, and so on. A 2D image of the differential conductivity over the sample surface can also be captured by scanning across the surface. In contrast to the constant-current topographic images containing both geometric and electronic

features, the differential (dI/dV, or d^2I/dV^2) imaging allows the extraction of contributions from electronic structures through a modulation technique.[22]

In addition to the measurements of the surface morphology and the LDOS, STM can be used to study the local tunneling barrier, which is related to the work functions of both tip and sample.[1, 19] The tunneling current is exponentially dependent on the tip-sample distance (Z): $I \propto \exp\left(-2\sqrt{2m\phi}\right)/\hbar \times Z$, where m is the electron mass and $\phi = (\phi_T + \phi_S)/2$ is the averaged work function of the tip and sample. Thus, the averaged work function can be extracted from the measurements of tunneling current relative to tip-sample separation. The slope of the logarithmic current can be plotted as a function of Z and we have $d\ln I/dZ \propto -\sqrt{\phi}$. Therefore, by recording the $d\ln I/dZ(x,y)$ over the surface, a map of the local tunneling barrier height can be obtained with atomic resolution.[23]

2.1.4 Tunneling through adsorbates

When atoms, molecules or clusters adsorb on solid surfaces, the tunneling process between tip and sample becomes more complex. Here, we only consider the case of a molecule adsorbed on a single-crystal surface, for STM experiments performed under UHV conditions. When the adsorbate is infinitely far from the surface, its electronic states consist of a series of occupied electronic molecular orbitals as well as a series of unoccupied or virtual molecular orbitals, where the HOMO represents the highest occupied molecular orbital, and the LUMO represents the lowest unoccupied molecular orbital. When a molecule is brought

in contact with a surface, several physical effects will influence its electronic structure. First, the interactions between the molecule and surface could rearrange the electron density and modify the alignment of frontier occupied or unoccupied orbital energies. In the case of physisorption with relatively weak adsorbate-substrate interactions, the energy shifts are generally very small. In the case of chemisorption, the shifts could be large. Second, electronic coupling to extended states in the metal will further shift orbital energies and broaden discrete molecular levels into resonances. Third, strong intermolecular interactions, such as chemical covalent bonding and metal-ligand coordination bonding, can also result in a re-distribution of the LDOS.[23] Finally, the energy levels of the adsorbed species can even be shifted by the electric field induced by the applied bias between the sample and the tip during STM operation. In general, the STM images of molecules assembled on surfaces contain information of both the adsorbates and the substrate. There is no simple way to accurately depict the displacement of the energy levels of the adsorbate relative to the substrate Fermi level. An accurate electronic structure calculation for a real adsorbate-surface system involving full-scale molecule-surface interactions is also too complicated to achieve.

Figure 2.4 represents two typical tunneling processes that could happen when the molecules or clusters adsorb on a surface. Only the case of a negative bias applied to the tip is discussed here. As the tunneling direction is essentially arbitrary and depends on the sign of the bias, the tunneling direction between the tip and sample can be symmetrically interchanged by simply changing the sign of

the bias. It has been known that the tunneling process depends on the available unoccupied electron states of the adsorbed molecules in the energy window eV_{bias}. In the first situation illustrated in Figure 2.5a, electrons will directly tunnel from the tip to the sample as there are no unoccupied electronic states of the molecule in the eV_{bias} window. Typical examples for this case are small molecules (e. g., O_2, N_2, and H_2) adsorbed on metal or semiconductor surfaces.[24] In the second situation depicted in Figure 2.4b, electrons will first tunnel from the tip to the unoccupied states of the absorbed molecules and then to the substrate, when there are some available electronic states of the molecule in the energy window. Most tunneling processes that occur in adsorbed conducting or semiconducting conjugated molecules belong to the later category.[25] The electron transport processes involved in tunneling from the tip to molecule first and then to the substrate or *vice versa*, have attracted great interest because they critically determine the performance of future molecular electronics devices.[26-30]

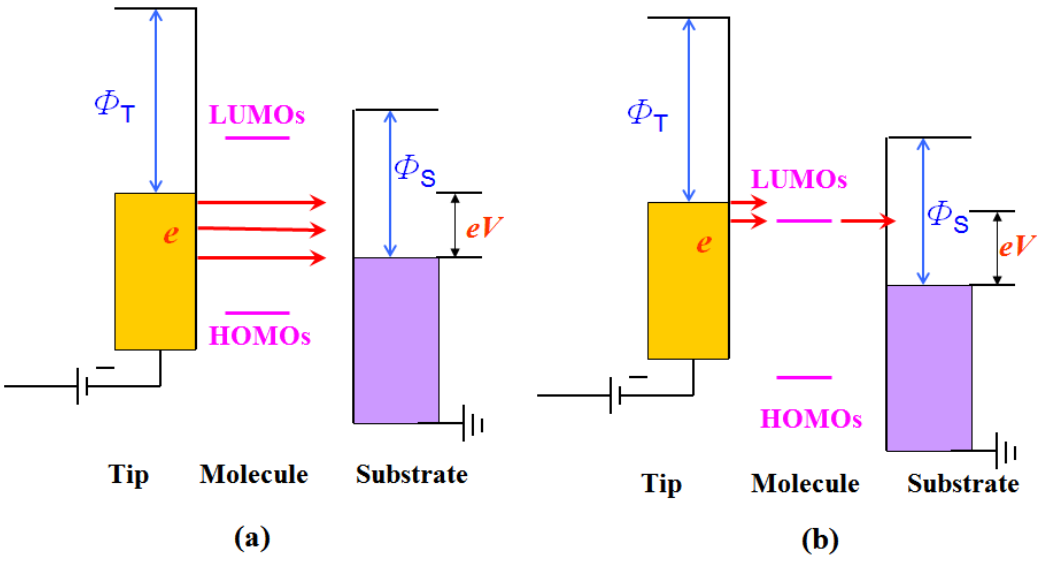

Figure 2.4 Two typical tunneling processes may occur in the adsorbate/substrate system: (a) electrons directly tunnel from the tip the substrate as no available unoccupied electronic states in the energy window eV_{bias}; and (b) electrons first tunnel to the molecule and finally to the substrate when there are unoccupied electronic states of the adsorbed molecules in the energy window eV_{bias}.

In a classical tunneling process, the electrons from the tip will tunnel into the electronic states with equivalent energy level in the substrate or the molecule without energy loss. Such conventional phenomena are known as elastic electron tunneling, as depicted in Figure 2.4. There is an alternative process shown in the schematic drawing of Figure 2.5a: the tunneling electron loses some energy ($h\nu$) during the tunneling by exciting a vibrational mode or releasing a photon, and subsequently transmits into the lower energy electronic state and finally tunnels into the substrate. Such inelastic tunneling only happens when the electron energy exceeds a certain value ($V_0 > h\nu$). The appearance of new channels in inelastic tunneling will result in an increase of the conductance (dI/dV) for $V > 0$ but a decrease for $V < 0$ (the bias voltage is applied to the sample, as shown in Figure 2.5b).[31] Thereby, extra peaks could be observed in the spectra of d^2I/dV^2-V curves as evidence of inelastic tunneling (Figure 3.5b).[32, 33] The measurements of inelastic tunneling spectroscopy (IETS) by STM can be used for chemical analysis at the atomic scale as every chemical bond has specific vibration modes. This is a significant technique that can overcome the general lack of chemical sensitivity of the STM technique.

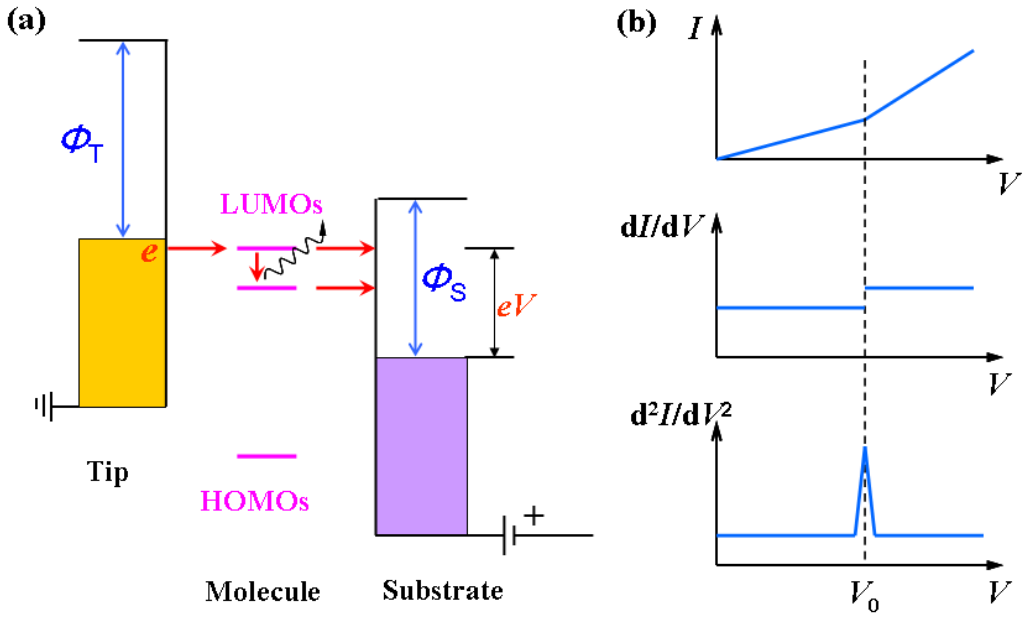

Figure 2.5 (a) Schematic drawing shows the inelastic tunneling process by exciting a vibration mode or releasing a photon. (b) Corresponding electronic spectra for the inelastic tunneling.[31]

2.1.5 Further applications of STM

The unique characters of STM, however, are not limited to the real space imaging of the topographical and electronic structure of surfaces. Intensive attention has been paid to the use of tunneling current as an electron source. Because the STM tip is very sharp (an idea tip has only one atom at its apex), and the tunneling electrons are spatially localized in an atomic scale area, it could cause a large current density whose magnitude can reach ~1×10^6 A/cm^2, which cannot be obtained by other conventional electron sources. It has been demonstrated in section **2.1.4** that the tunneling electrons can induce some vibration modes in the adsorbate via inelastic tunneling. Beside the measurements of IETS which can be used to analyze the chemical bonds of the adsorbates, the

vibrational excitation can induce various surface phenomena, such as molecular desorption,[34-36] hopping,[37-39] rotation[40] as well as chemical reactions[41-45] (e. g., isomerization). Though the possibility of each electron to induce such reaction is very low (~ 10^{-9} – 10^{-12}), the STM is an efficient tool to study these surface dynamic phenomena due to its high current density.[46-51]

By bringing the STM tip close to the adsorbates, it is possible to move the adsorbed atom or molecule via strong tip-adsorbate repulsive or attracted interactions.[15, 52, 53] Such lateral manipulation of single atoms or molecules allows the construction of artificial surface nanostructures with desired properties.[11, 52, 53] Moreover, as the STM experiment is operating at a tip-sample separation of less than 10 Å and a low bias of few V or less, adsorbates at the surface are actually subjected to an electric field of the order of 10^7 V/cm. Such strong electric fields can induce dynamic motion of the adsorbate if it is a dipolar molecule. The control of single-atom or single-molecule dynamical motion or chemical reaction is of significance for nanoscale electronic devices, where each single constituent serves as memory element, diode, transistor, or switch. With the capabilities of real-space atomic imaging and manipulation, the STM is a powerful tool for monitoring surface phenomena, characterizing geometrical and electronic properties of nanostructures and even building atomic scale patterns, which make it a unique technique in advancing the development of nanoscience and nanotechnology.

2.2 Complementary surface analytical tools

2.2.1 Photoelectron spectroscopy

Photoelectron spectroscopy (PES) is an established experimental tool extensively used in surface investigations.[54] The physical principle behind PES is the well-known photoelectric effect, which was explained by Albert Einstein in 1905.[55] When a matter is exposed to a light source, the electrons that occupy a certain initial energy state (E_i) can absorb a photon and escape from the material into vacuum as photoelectrons with kinetic energy of E_K (as shown in Figure 2.6a). A flow of emitted electrons will be detected only when the photon energy is above a certain threshold frequency. For photon energy of $h\nu$, the maximum kinetic energy of the electron ejected from the sample is $E_K^{\max} = h\nu - \phi_S$, where ϕ_S is the work function of the sample. As the electron is usually released from an initial occupied state below the Fermi level, the kinetic energy should be:

$$E_K = h\nu - E_B - \phi_S \qquad (1)$$

where the electron binding energy E_B corresponds to the energy difference between the initial energy state of the electron and the Fermi energy. Equation (1) can be expressed as $E_B = h\nu - E_K - \phi_S$. Thus, by measuring the kinetic energy (E_K) spectrum of the emitted photoelectrons, the binding energy of the sample can be determined simultaneously.

Figure 2.6b shows a typical PES spectrum. The low kinetic energy part is the secondary-electron region, and the high kinetic energy part corresponds to the valence region. $E_{K,SECO}$, $E_{K,EF}$ and $E_{K,HOMO}$ represent the linear extrapolations of the kinetic energy onsets of the secondary electron cut-off (SECO), substrate

Fermi level and HOMO for organic thin films. *W* is the spectrum width equal to the kinetic energy difference between the $E_{K,SECO}$ and $E_{K,EF}$. From the spectrum, we have

$$\phi_S = h\nu - W = h\nu - (E_{K,E_F} - E_{K,SECO}) \quad (2)$$

It should be noted that the photoelectrons measured by the analyzer must overcome the work function difference between the spectrometer and the sample. A negative sample bias (e.g., -5 eV) is usually applied to the sample to facilitate the measurement of the SECO.

The HOMO for the organic thin film can be determined from the PES spectrum as shown in Figure 2.6b, and the hole injection barrier (Δ_h) is defined as the energy difference between the substrate Fermi level and the HOMO leading edge:

$$\Delta_h = E_{K,E_F} - E_{K,HOMO} \quad (3)$$

The ionization potential (IP) of the organic thin film, which is the energy difference between the HOMO and the vacuum level or the sum of the sample work function and the hole injection barrier, can also be determined via the equation:

$$IP = \phi_S + \Delta_h = h\nu - (E_{K,HOMO} - E_{K,SECO}) \quad (4)$$

Through PES measurements, we are able to depict the energy level alignments of organic thin films at organic-substrate interfaces or organic-organic heterojunctions, which play a crucial role in determining the performance of organic thin-film-based electronics.

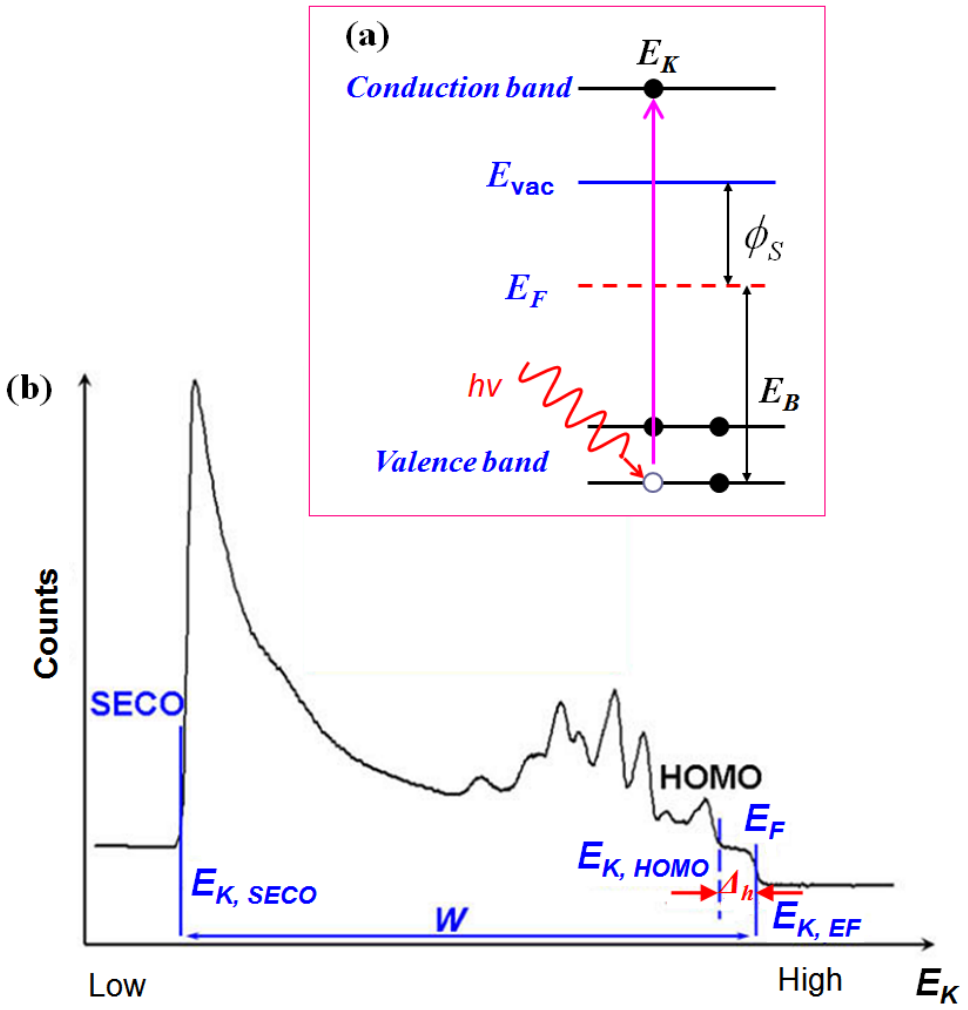

Figure 2.6 (a) A schematic drawing shows the photoelectron emission process in the PES measurement. (b) A typical PES spectrum of an organic thin film.[56]

A typical experiment set-up for PES measurements is schematically shown in Figure 2.7, composing a light beam, an electron energy analyzer and a data collection system. The light source of the PES could be a gas-discharge lamp (visible or ultra-violet light), an X-ray tube, or a synchrotron radiation source (intensive light source with tunable photon energy). According to the photon energy of the radiation source, PES can be divided into two main categories,

namely ultraviolet photoelectron spectroscopy (UPS) and X-ray photoelectron spectroscopy (XPS). The ultraviolet (UV) light source ($h\nu$ = 10 ~ 100 eV) for UPS is commonly a gas discharge lamp, and the helium discharge lamp is the most commonly used source. The He discharge lamp can emit He I spectral line at 21.1 eV and He II line at 40.82 eV depending on the gas pressure and discharge current conditions. Due to its relatively low photon energy, UPS is only able to ionize valence electrons from the outermost energy levels of the sample materials. It is usually used to study the work function (ϕ_S) and valence energy levels of semiconducting materials, as well as the electronic characteristics of molecular occupied orbitals. With detailed angle resolved UPS (ARUPS) measurements, the complete valence band structures in *k*-space can be mapped out. A good resolution of several meV can be achieved in UPS owing to the very narrow line width of the He radiation source.

In XPS, higher photon energies are used to study core-level excitations. Mg Kα (1253.6 eV) and Al Kα (1486.6 eV) radiations are two most common X-ray laboratory sources. XPS can provide information on the chemical composition of the studied materials by examining the energies of the characteristic peaks in the spectrum, as the binding energy E_B of the core-level electrons are usually element specific. The E_B of the core-level electrons can be altered by the local chemical (e. g. number of valence electrons) or physical environment (e. g. crystal symmetry) around the excited atom. The changes to the E_B recorded in the XPS spectrum are referred as binding energy shifts (BE shift).[54] Thus, XPS can be used to distinguish the chemical state or valence state of the elements by the BE shift.

Furthermore, detailed analysis of the peak intensity can be used to estimate the thickness of the prepared thin film or the relative concentration of the constituents.[54]

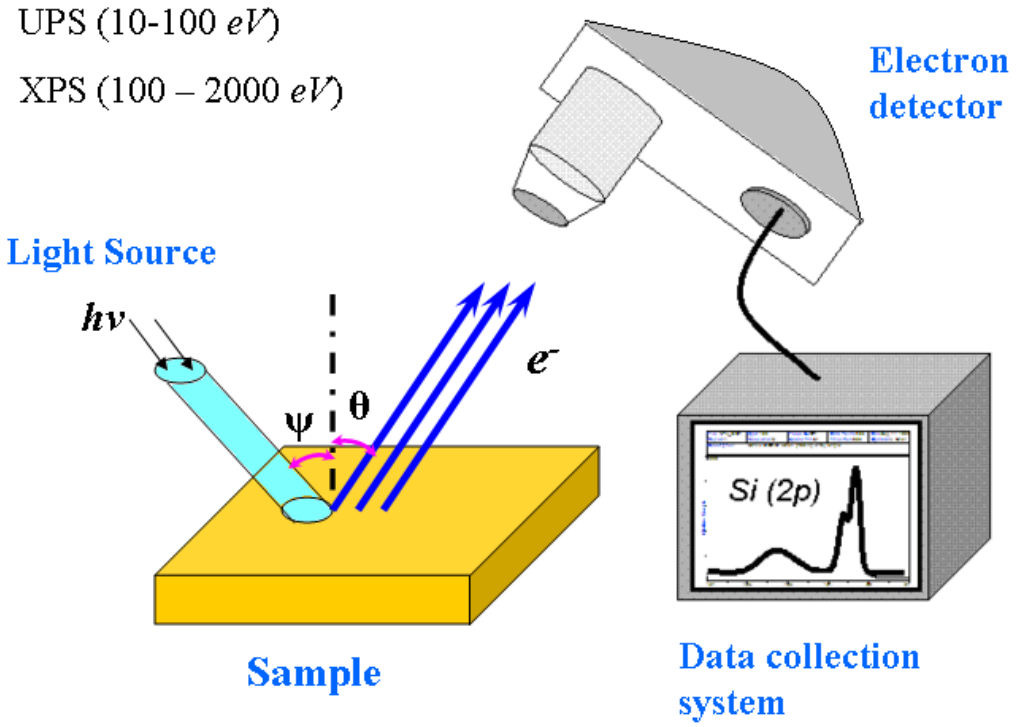

Figure 2.7 A typical experimental set-up for PES measurements, including a light source, an electron detector and a data collection system.

2.2.2 Near-edge X-ray absorption fine structure measurements

Near-edge X-ray absorption fine structure (NEXAFS) is another widely used surface characterization technique to probe the unoccupied electronic states of materials.[57] As shown in Figure 2.8, when an electron residing in the core-level of an atom adsorbs an X-ray photon and is excited into an unoccupied energy state, the resulting core hole is subsequently filled by a capture of an electron from the outer shell level and followed by either a creation of an Auger electron (Figure

2.8b) or an emission of a fluorescent photon (Figure 2.8c).[57] Information of the initial photoelectron, fluorescent photon, Auger electron or even the inelastically scattering photoelectron are all measured in the X-ray absorption spectrum (Figure 2.8d). The structures close to the X-ray absorption edge (10 – 50 eV) are known as the NEXAFS region. The extended region with higher photon energies (50 – 1000 eV above the absorption edge) are known as the extended X-ray absorption fine structure (EXAFS) region, which usually exhibits weak oscillations due to interference between back-scattered electron waves with forward-propagating electron waves (Figure 2.8d). There are many methods used to record NEXAFS spectra, including fluorescent yield by monitoring the emitted photons, auger electron yield (AEY), partial electron yield (PEY), and total electron yield (TEY). The TEY method is used in our NEXAFS measurements, where the sample is connected to ground through an ammeter and the neutralization current is measured.

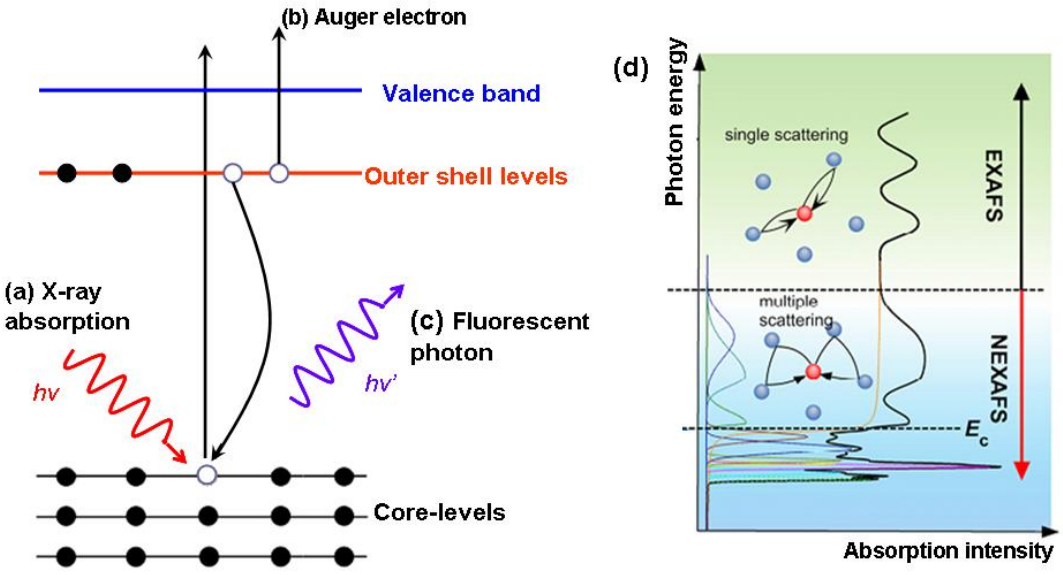

Figure 2.8 Schematic diagram demonstrates the principle of the X-ray absorption measurement, involving (a) X-ray absorption, and subsequent excitation of (b) Auger electrons or (c) fluorescent photon. (d) shows a typical X-ray absorption spectrum including both NEXAFS (low energy region) and EXAFS (high energy region).

The NEXAFS spectrum is element specific as XPS, because every element has its specific absorption energy edge, and NEXAFS allows the extraction of the signals in the presence of a large background signal. The NEXAFS measurement is able to study buried atoms due to the integration over all final states including inelastic scattering electrons.[57] In contrast, for photoemission or Auger spectroscopy, only the few surface layers are sampled. Furthermore, NEXAFS measurement is highly sensitive to bond angles, bond lengths and the presence of adsorbates.[57] One important application of NEXAFS studies is the determination of the molecular orientation in organic thin films. Planar organic molecules have unoccupied π^* and σ^* molecular orbitals, where the orientation of π^* orbitals are typically perpendicular to the molecular plane and σ^* orbitals are parallel to the molecular plane. The relative direction between a particular molecular orbital and the electric field vector of the incident light can enhance (parallel) or weaken (perpendicular) the related resonant transitions.[57] Therefore, by performing angular-dependent NEXAFS measurements, the orientation of the adsorbed molecules relative to the substrate can be determined. Synchrotron radiation with a natural polarization is typically used for NEXAFS studies.

2.3 Our experimental systems

2.3.1 Multi-chamber low-temperature STM system

Our STM setup is a custom-built multi-chamber UHV system with base pressure better than 1.0×10^{-10} mbar, and housing an Omicron LT-STM interfaced to a Nanonis controller.[58-61] Figure 2.9 displays the picture of our LT-STM system, where the STM chamber (right) is attached to a preparation chamber (left) through a gate valve. Under UHV conditions, we can avoid contaminating the sample surface and ensure the measurements under well controlled conditions. Our LT-STM is equipped with a cryostat for liquid N_2 or He, which can cool the sample down to 77 K or 4 K respectively for STM imaging. At low temperatures, the adsorbed molecules have low thermal energy and are more stable. The background noise originating from thermal vibration is also reduced, which makes it become easier to obtain atomically resolved images. Most STM images were recorded at 77 K in this thesis, and the ones recorded at 4 K (e. g., single-molecule manipulation in section **6.4**) are highlighted. The tunneling current we used for 2D STM imaging is usually in the range of 60 pA to100 pA, and the tip voltages for all STM images are specified in the text.

The sample preparation chamber is also kept at UHV (base pressure $< 5.0 \times 10^{-10}$ mbar) to avoid contamination. It is mounted with several Knudsen effusion cells, a sputtering gun, a quartz-crystal-microbalance (QCM), a manipulator (x, y, z, θ) with heating filament, and a long-arm transporter. Before molecular deposition, freshly-cleaved highly orientated pyrolytic graphite (HOPG) substrates (MaTecK, grade ZYB, mosaic spread of 0.8°) were thoroughly

degassed in the preparation chamber at around 500 ℃ overnight; the single crystal metal substrates, such as Au(111) and Ag(111), were cleaned by repeated Ar^+ sputtering and annealing (500 ℃) circles to obtain clean, atomically flat surfaces. Molecules were thermally evaporated from the Knudsen cells onto the clean substrates kept at room temperature. Prior to deposition, all the molecular sources were purified twice by gradient vacuum sublimation. The deposition rates were monitored by the QCM during evaporation, and were further calibrated by counting the molecular coverage in large-scale LT-STM images. In our experiments, all the depositions were performed at slow, constant rates, typically about 10^{-2} ML per minute (1 ML = one close packed monolayer with the molecular π-plane oriented parallel to the substrate). For example, the deposition rates of F_{16}CuPc and CuPc are about 0.05 ML min^{-1}, DIP, 6P and pentacene are about 0.02 ML min^{-1}, and so on. For the fabrication of binary molecular networks, different molecules were sequentially deposited from separated Knudsen cells onto the substrates. Further treatment of the samples, such as annealing, can also be performed in the preparation chamber. The prepared samples were immediately transferred into the LT-STM scanning chamber via the UHV gate valve for STM measurements.

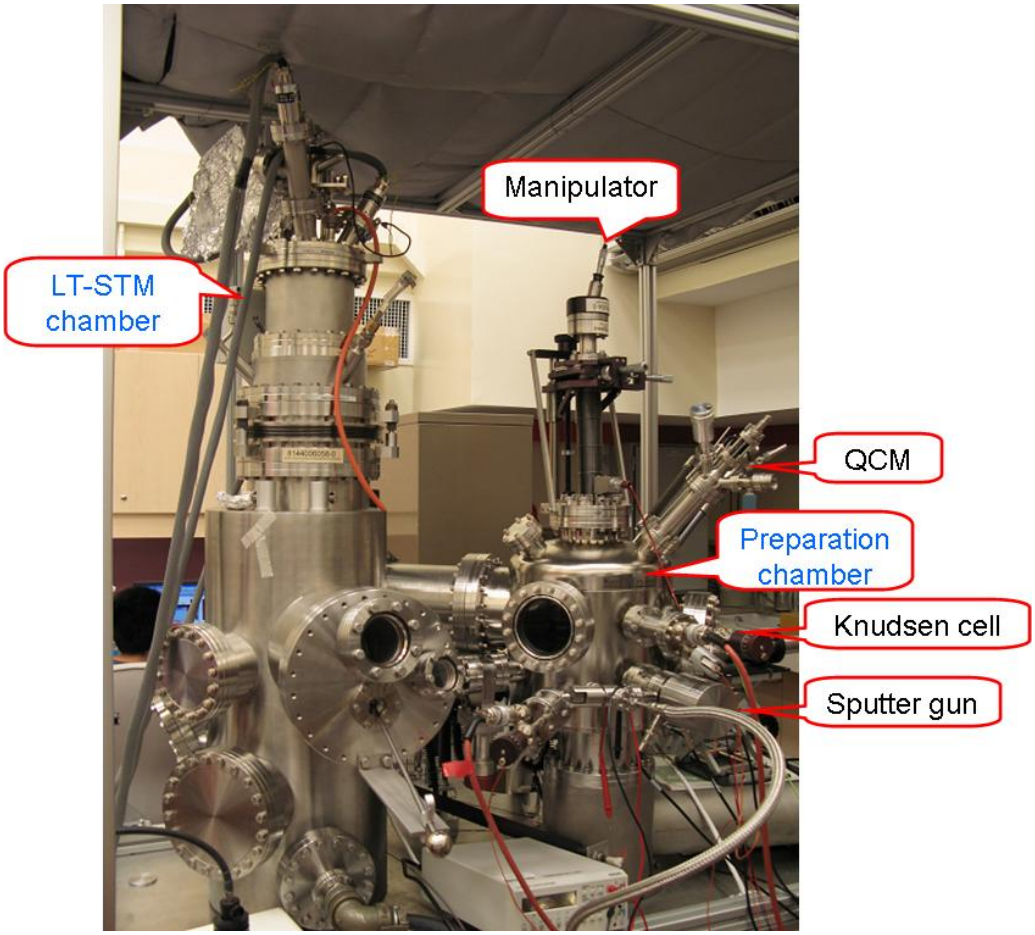

Figure 2.9 The setup of LT-STM chamber (left) and the attached preparation chamber (right).

2.3.2 Synchrotron photoemission measurements

Synchrotron radiation is an important light source in photoemission measurements due to its intense electromagnetic radiation with tunable photon energy. It has a wide energy spectrum from the far infrared to the hard X-ray regime, which enables us to continuously tune the wavelength of the photon beam to desired energies. The schematic drawing in Figure 2.10 shows the setup of our Singapore Synchrotron Light Source (SSLS) facility. The synchrotron radiation is generated by the acceleration of relativistic charged particles through a magnetic

field, which can be achieved artificially in a storage ring. Each end station is connected to a beamline, where the energy of the photon beam can be selected.

Our PES and NEXAFS measurements were carried out at the Surface, Interface and Nanostructure Science (SINS) beamline of the SSLS, which is a second generation light source comprising a compact 700 MeV superconducting storage ring (Helios 2) with 4.5 T bending magnets to produce synchrotron radiation (Figure 2.10). The radiation spectrum extends from about 10 keV down to the far infrared at wavenumbers of less than 10 cm^{-1}. The NEXAFS measurements were performed in TEY mode with a photon energy resolution of 0.1 eV. The organic molecular thin films were prepared in a separate preparation chamber attached to the analytic chamber (Figure 2.11). The sample preparation processes are similar to that in the STM system discussed previously. Here, the deposition rates were further calibrated by monitoring the attenuation in intensity of the Au $4f_{7/2}$ peak before and after deposition on a sputter-cleaned poly Au sample.

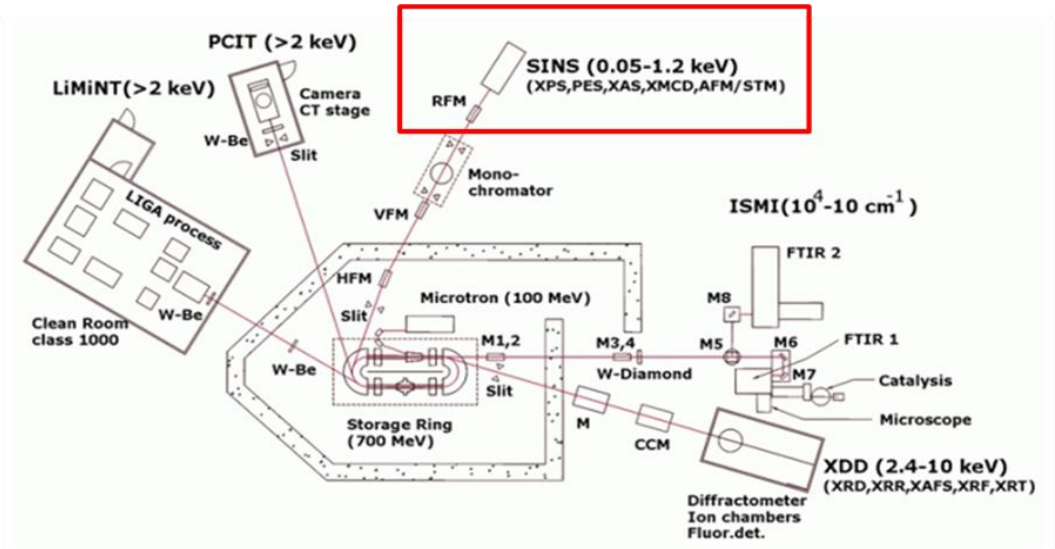

Figure 2.10 The facility layout of the beamlines of SSLS.[62]

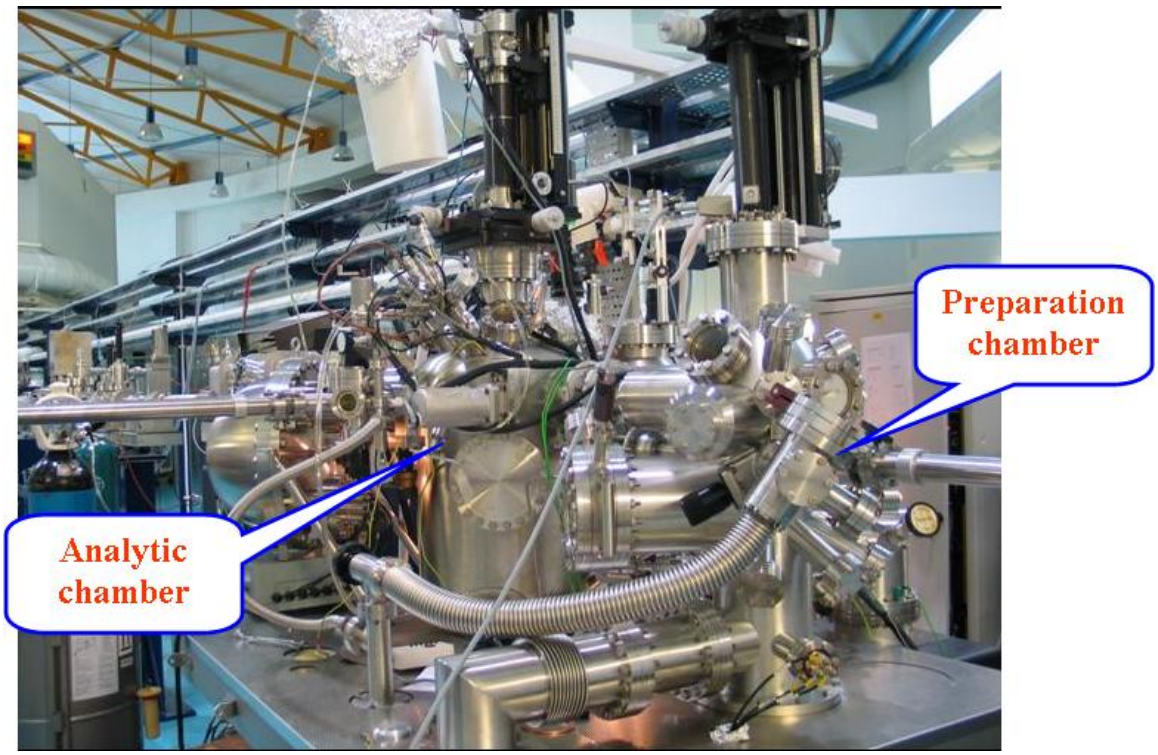

Figure 2.11 Photograph showing the end-station of SINS beamline at SSLS.

Reference:

[1] G. Binnig, H. Rohrer, Ch. Gerber, E. Weibel, *Appl. Phys. Lett.***40**, 178-180 (1982)

[2] D. M. Eigler, E. K. Schweizer, *Nature* **344**, 524-526 (1990).

[3] M. Ringger, H. R. Hidber, R. Schlögl, P. Oelhafen, H.-J. Güntherodt, *Appl. Phys. Lett*. **46**, 832-834 (1985).

[4] H. Fuchs, R. Laschinski, T. Schimmel, *Europhys. Lett.* **13**, 307-311 (1990).

[5] C.W. Lin, F.-R. Fan, A. J. Bard, *J. Electrochem. Soc.* **134**, 1038- 1039 (1987).

[6] E. E. Ehrichs, R. M. Silver, A. L. de Lozanne, *J. Vac. Sci. Technol. A* **6**, 540-543 (1988).

[7] R. S. Becker, J. A. Golovchenko, B. S. Swartzentruber, *Nature* **325**, 419-421 (1987).

[8] H. J. Mamin, P.H. Guethner and D. Rugar, *Phys. Rev. Lett.* **65**, 2418-2421 (1990).

[9] J. A. Stroscio, D. M. Eigler, *Science* **254**, 1319-1326 (1991).

[10] I.-W. Lyo, P. Avouris, *Science* **253**, 173-176 (1991).

[11] D. M. Eigler, C. P. Lutz, W. E. Rudge, *Nature* **352**, 600-603 (1991).

[12] H. Fuchs, T. Schimmel, *Adv. Mater.* **3**, 112-113 (1991).

[13] R. A. Wolkow, *Annu. Rev. Phys. Chem.* **50**, 413-441 (1999), and references therein.

[14] H. Brune, *Surf. Sci. Rep.* **31**, 125-225 (1998), and references therein.

[15] S. W. Hla, K. H. Rieder, *Annu. Rev. Phys. Chem.* **54**, 307-330 (2003). and reference therein.

[16] J. I. Pascual, N. Lorente, Z. Song, H. Conrad, H. P. Rust, *Nature* **423**, 525-528 (2003).

[17] K. Oura, V. G. Lifshits, A. A. Saranin, A. V. Zotov, and M. Katayama, *Surface science: an introduction*. (Berlin: Springer-Verlag, 2003).

[18] http://en.wikipedia.org/wiki/Scanning_tunneling_microscope.

[19] R. Wiesendanger, H.-J. Guntherodt, et al., *Scanning tunneling microscopy I: general principles and applications to clean and adsorbate-covered surfaces*, (Berlin; New York: Springer , c1992).

[20] R. J. Hamers, *Annu. Rev. Phys. Chem.* **40**, 531-559 (1989).

[21] J. A. Kubby, J. J. Boland, *Surf. Sci. Rep.* **26**, 61-204 (1996).

[22] D. W. Abraham, C. C. Williams, H. K. Wickramasinghe, *Appl. Phys. Lett.* **53**, 1503-1505 (1988).

[23] L. Vitali, G. Levita, R. Ohmann, A. Comisso, A. De Vita, K. Kern, *Nat. Mater.*, **9**, 320-323 (2010).

[24] R. Martel, P. Avouris, I.-W. Lyo, *Science* **272**, 385-388 (1996).

[25] R. A. Wolkow, *Annu. Rev. Phys. Chem*. **50**, 413-441 (1999), and reference therein.

[26] G. V. Nazin, X. H. Qiu, W. Ho, *Science* **302**, 77-81 (2003).

[27] S. Datta, W. Tian, S. Hong, R. Reifenberger, J. Henderson, C. P. Kubiak, *Phys. Rev. Lett.* **79**, 2530-2533 (1997).

[28] N. D. Lang, Ph. Avouris, *Phys. Rev. B*, **64**, 125323 (2001).

[29] J. Heurich, J. C. Cuevas, W. Wenzel, G. Schőn, *Phys. Rev. Lett.* **88**, 256803 (2002).

[30] L. Patrone, S. Palacin, J. Charlier, F. Armand, J. P. Bourgoin, H. Tang, S. Gauthier, *Phys. Rev. Lett.* **91**, 096802 (2003).

[31] T. Komeda, *Prog. Surf. Sci.* **78**, 41–85 (2005), and preferences there in.

[32] T. Komeda, Y. Kim, M. Kawai, *Riken Rev*. 26–33 (2001).

[33] B. C. Stipe, M. A. Rezaei, W. Ho, *Science* **280**, 1732–1735 (1998).

[34] K. Stokbro, C. Thirstrup, M. Sakurai, U. Quaade, B.Y. K. Hu, F. Perez-Murano, F. Grey, *Phys. Rev. Lett.* **80**, 2618–2621 (1998).

[35] J. A. Misewich, T. F. Heinz, D. M. Newns, *Phys. Rev. Lett.* **68**, 3737–3740 (1992).

[36] D. M. Eigler, C. P. Lutz, W. E. Rudge, *Nature* **352**, 600–603 (1991).

[37] A. G. Fedorus, V. V. Gonchar, O. V. Kanash, E. V. Klimenko, A. G. Naumovets, I. N. Zasimovich, *Surf. Sci*. **251**, 846–850 (1991).

[38] T. Komeda, Y. Kim, M. Kawai, B. N. J. Persson, H. Ueba, *Science* **295**, 2055–2058 (2002).

[39] T. Komeda, Y. Kim, Y. Fujita, Y. Sainoo, M. Kawai, *J. Chem. Phys.* **120**, 5347–5352 (2004).

[40] B. C. Stipe, M. A. Rezaei, W. Ho, *Phys. Rev. Lett.* **81**, 1263–1266 (1998).

[41] F. F. Crim, *Acc. Chem. Res.* **32**, 877–884 (1999).

[42] S. W. Hla, L. Bartels, G. Meyer, K. H. Rieder, *Phys. Rev. Lett.* **85**, 2777–2780 (2000).

[43] B. C. Stipe, M. A. Rezaei, W. Ho, S. Gao, M. Persson, B. I. Lundqvist, *Phys. Rev. Lett.* **78**, 4410–4413 (1997).

[44] V. Simic-Milosevic, M. Mehlhorn, K. H. Rieder, J. Meyer, K. Morgenstern, *Phys. Rev. Lett*. **98,** 116102 (2007).

[45] P. Liljeroth, J. Repp, G. Meyer, *Science* **317**, 1203-1206 (2007).

[46] C. Nacci, J. Lagoute, X. Liu, S. Fölsch, *Phys. Rev. B* **77**, 121405 (2008).

[47] B. C. Stipe, M. A. Rezaei, W. Ho, *Phys. Rev. Lett.* **81**, 1263-1266 (1998).

[48] T. Komeda, Y. Kim, M. Kawai, B. N. J. Persson, H. Ueba, *Science* **295**, 2055-2058 (2002).

[49] B. C. Stipe, M. A. Rezaei, W. Ho, S. Gao, M. Persson, B. I. Lundqvist, *Phys. Rev. Lett.* **78**, 4410-4413 (1997).

[50] Y. Kim, T. Komeda, M. Kawai, *Phys. Rev. Lett.* **89**, 126104 (2002).

[51] T. Komeda, Y. Kim, Y. Fujita, Y. Sainoo, M. Kawai, J. Chem. Phys. 120, 5347-5352 (2004).

[52] L. Bartels, G. Meyer, K.-H. Rieder, *Phys. Rev. Lett*. **79**, 697-700 (1997).

[53] R. Otero, F. Rosei, F. Besenbacher, *Annu. Rev. Phys. Chem*. **57**, 497–525 (2006), and references therein.

[54] S. Hüfner, *Photoelectron Spectroscopy: Principles and Applications* (Springer, 2003).

[55] A. Einstein, *Ann. Phys.* **17**, 132-148 (1905).

[56] W. Chen, D. C. Qi, X. Y. Gao, A. T. S. Wee, *Prog. Surf. Sci.* **84**, 279–321 (2009).

[57] J. Stöhr, *NEXAFS spectroscopy* (Springer, Berlin, 1992).

[58] W. Chen, H. L. Zhang, H. Huang, L. Chen, A. T. S. Wee, *Appl. Phys. Lett.* **92**, 193301 (2008).

[59] W. Chen, H. L. Zhang, H. Huang, L. Chen, A. T. S. Wee, *ACS Nano*, **2**, 693-698 (2008).

[60] L. Chen, W. Chen, H. Huang, H. L. Zhang, J. Yuhara, A. T. S. Wee, *Adv. Mater.* **20**, 484-488 (2008).

[61] H. L. Zhang, W. Chen, L. Chen, H. Huang, J. Yuhara, A. T. S. Wee, *Small*. **3**, 2015-2018 (2007).

[62] http://ssls.nus.edu.sg/index.html.

Chapter 3

Epitaxial Growth of Ultra-thin Organic Molecular Films

3.1 Introduction

Over the past several years, developments in thin film based organic electronic devices have attracted much attention due to their potential applications in low-cost, large-scale and flexible electronic devices, such as organic light-emitting diodes (OLEDs), organic field-effect transistors (OFETs), and organic solar cells.[1-7] It is known that the interfaces between the active organic layers and the substrate, i.e., molecule/electrode or molecule/dielectric interfaces, play a crucial role in determining the device performance.[8-13] For example, in sexithienyl thin film transistors (TFTs), it has been demonstrated that only the first two molecular layers next to the dielectric interface determine the charge transport.[14] As thus, it is very critical to understand the molecule-substrate interface properties in order to improve the device performance. The factors that can affect the organic devices include the supramolecular packing, molecular orientation of the thin films, interfacial electronic energy level alignment, hole or electron injection barriers, interfacial charge or energy transfer, charge carrier trapping at the interface, surface transfer doping of organic active layers, and son on.[8-34]

The molecular orientation near the interface which is one of the important factors in determining the electronic properties of organic thin films, is mainly governed by the balance between molecule-substrate interfacial interactions and intermolecular interactions.[21, 34-38] For example, the molecular orientation of organic thin films, i.e., standing-up vs. lying-down, can be controlled by manipulating the substrate electronic structure, i.e., the effective coupling between molecular orbitals and substrate valence or conduction bands.[34] Much research has been devoted to the engineering of interface properties to improve device performance via various surface modification schemes.[39-41] In order to understand the thin film growth mechanism and hence to facilitate the fabrication of organic thin films with desired properties, it is necessary to carry out systematic investigations of the growth and electronic structures of organic molecules on well-defined substrates.

In this chapter, we study the supramolecular packing and molecular orientation of π-conjugated organic molecules on solid surfaces, where F_{16}CuPc and DIP molecules are selected as prototype systems. Both F_{16}CuPc and DIP molecules are promising organic semiconductors with potential applications in organic electronic devices. Phthalocyanines (e. g., CuPc) and their derivatives (e. g., F_{16}CuPc) have widespread applications in optoelectronic devices, chemical sensors, organic solar cells, and so on.[35-38] F_{16}CuPc is an *n*-type semiconducting molecule with good chemical-, thermal- and air-stability, which makes it suitable for use in organic semiconductor devices, in particular *n*-channel and bipolar OFETs.[23, 42-45] The long exciton diffusion length of at least 100 nm in DIP thin

films facilitates potential applications in excitonic organic photovoltaic cells.[46] A balanced charge carrier transport along the *c'* direction in DIP single crystals enables its use in ambipolar OFETs.[47] Here, the epitaxial growth of F_{16}CuPc and DIP thin films on graphite surfaces are investigated by LT-STM and NEXAFS measurements.

3.2 LT-STM and NEXAFS investigation of F_{16}CuPc thin films on graphite

Previously reported studies focused on the growth of F_{16}CuPc on inert dielectrics such as SiO_2.[48-50] On these substrates, F_{16}CuPc molecules adopt a standing up configuration with their molecular π-plane oriented nearly perpendicular to the substrate surface. In contrast, on single crystalline metal substrates such as Cu(111) and Ag(111), F_{16}CuPc molecules lie flat as suggested by STM studies.[51, 52] Here, LT-STM and NEXAFS measurements are used to study the epitaxial growth and molecular orientation of F_{16}CuPc thin films on HOPG.[53] Our results show that F_{16}CuPc molecules lie flat on HOPG up to 5 nm thickness, stabilized by interfacial and interlayer π-π interactions.

3.2.1 STM studies of F_{16}CuPc monolayer and bilayer on HOPG

At submonolayer coverages, F_{16}CuPc molecules predominantly decorate the step edges and then aggregate into single-layer islands with irregular-shapes on the graphite terraces (images are not shown here). At 1ML coverage, a closed-

packed monolayer phase of F_{16}CuPc on HOPG is formed, as shown by the molecularly-resolved STM images in Figure 3.1. The characteristic F_{16}CuPc STM image with a four-leaved pattern is similar to that of other Pc molecules and their derivatives that contain a central metal atom surrounded by a planar ligand shell formed by carbon, nitrogen, and hydrogen/halogen atoms.[37] F_{16}CuPc molecules lie flat on HOPG with their molecular planes parallel to the substrate, arising from the directional interfacial π-π interaction. Figures 3.1c-f show the bias-dependent and molecularly resolved 9 × 9 nm^2 STM images of F_{16}CuPc monolayer on HOPG, with tip bias ranging from 2.0V to -2.0V. The STM images at positive tip-bias originate from electron tunneling from HOMOs of the F_{16}CuPc molecules, and the images at negative tip-bias come from tunneling into the F_{16}CuPc LUMOs. It is worth noting that the central Cu atom site appears dark at positive tip bias (HOMOs, Figures 3.1 c and d), but it is brighter at negative tip bias (LUMOs, Figures 3.1 e and f). Such contrast inversion was not observed in case of CuPc, which is normally imaged with an apparent hole in the center of the molecules.[54, 55] Since STM imaging is sensitive to local density of electronic states, we propose that such inversion in the STM image contrast at opposite tip bias originates from the modulation of density-of-states at the Cu atom site by the fluorination of peripheral benzene rings.

The dashed lines in Figures 3.1a and b indicate that the F_{16}CuPc molecules pack into long stripes of different domains extending over the HOPG terraces. Each molecular row possesses the same in-plane orientation with a periodicitiy of about 1.55 nm; while in the direction perpendicular to the stripes, the in-plane

molecular orientation varies. It is useful to define an azimuthal angle θ between the molecular axis and the stripe direction, indicated by arrows in Figure 3.1b. Two different molecular orientations are observed for F_{16}CuPc monolayer on HOPG, denoted as α-orientation with θ_1=32 °±3 ° and β-orientation with θ_2=62 °±3 °. The molecular stripes with α- or β- domains are referred to as α- or β-stripe, respectively. The percentages of α- and β- domains are nearly equivalent. This suggests that both domains are two similar local energetic minima. There appears to be no long range ordering in the stacking sequence of these α- or β-stripes, as shown in Figure 3.1a. The coexistence of two orientations observed on HOPG is similar to that for F_{16}CuPc monolayer on Cu (111).[52] This is in contrast to the assembly behavior of CuPc on HOPG, where all molecules possess the same in-plane molecular orientation and form a closed-packed structure.[56, 57] The difference in the in-plane molecular orientation for unfluorinated and fluorinated copper phthalocyanine monolayers on HOPG most likely originates from the large repulsive forces between the negatively charged F atoms of the neighboring F_{16}CuPc molecules.

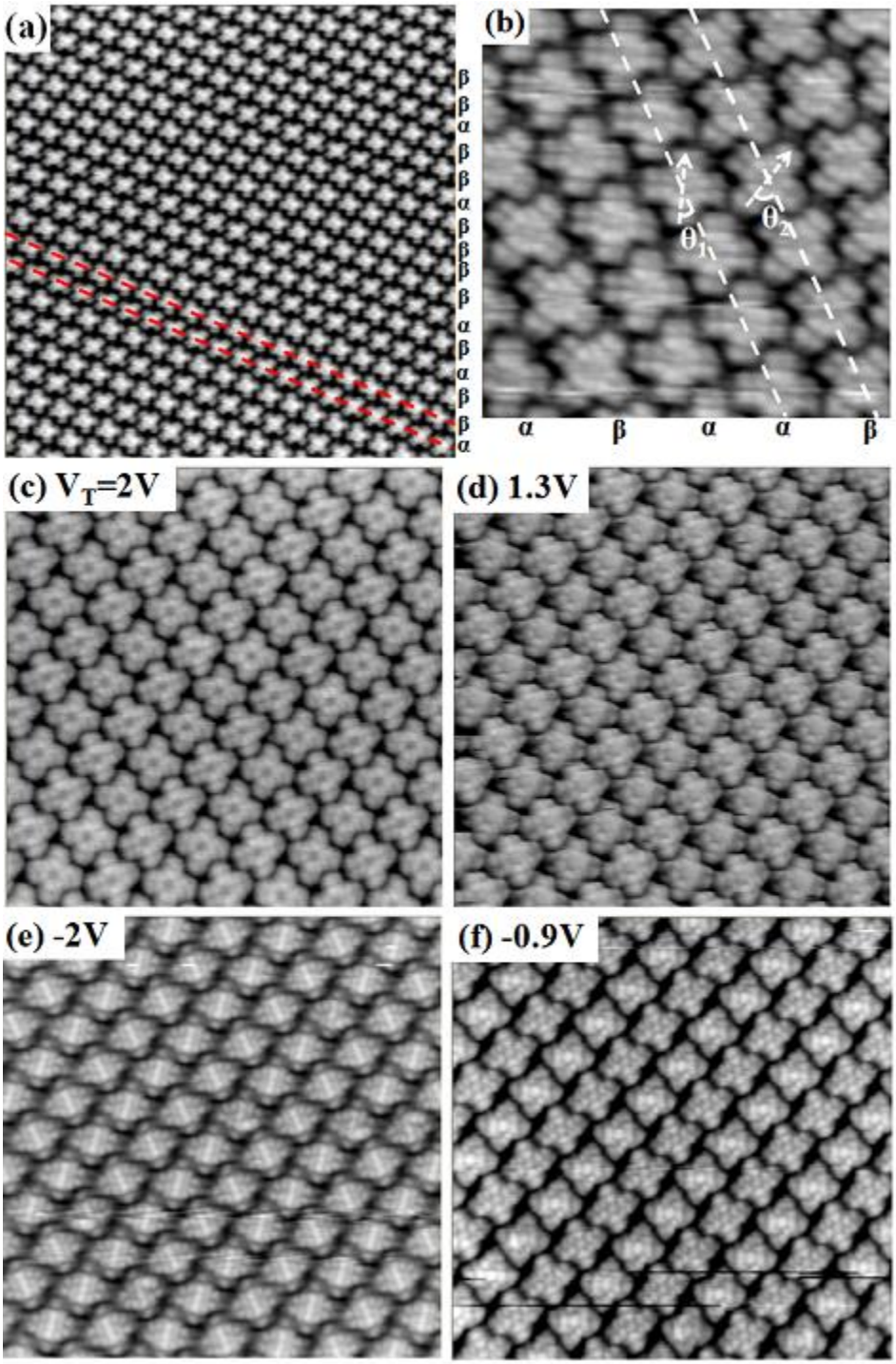

Figure 3.1 (a) STM image of $F_{16}CuPc$ monolayer on HOPG (V_{tip} = 2.3V, 30×30nm^2), and (b) its corresponding high-resolution image (V_{tip} = 2.5V, 9×9nm^2), where dashed lines indicate orientations of molecular rows and arrows indicate molecular axes. (c) - (f) are the bias-dependent images with V_{tip} = 2.0V, 1.3V, -0.9V and -2.0V respectively; the areas are 15×15nm^2 and I_{set} = 0.1nA.

The second layer starts to grow only after the substrate is fully covered by the F_{16}CuPc monolayer. Figure 3.2a is a large-scale STM image of monolayer F_{16}CuPc decorated with a few 2nd layer F_{16}CuPc molecules. Correspondingly, Figure 3.2b and c are 20×20 nm^2 STM images enlarged from the regions highlighted by the squares in Figure 3.2a. The molecules in the second monolayer are also flat lying, which is attributed to the interfacial π-π attractive interactions between the first and second layers. Some horizontal tip-induced diffusion streaks due to mobile F_{16}CuPc molecules on the first layer are observed during STM scanning, suggesting a weak bonding between the second and first F_{16}CuPc layers. It is also worth to note that the adsorbed 2nd layer F_{16}CuPc molecules preferentially adopt the α-orientation and perch atop the underlying ones with the same orientation (α-strip), as noted by the blue arrows in Figure 3.2b and c. The incomplete 2nd layer molecular stripe also reveals a lateral displacement (about 0.46 nm) between the 2nd layer and its underlying α-orientated F_{16}CuPc molecules along the molecular stripe direction. Such lateral displacement is suggested to maximize the interfacial π-π interaction, which has been reported in other phthalocyanines multi-layer films.[58, 59]

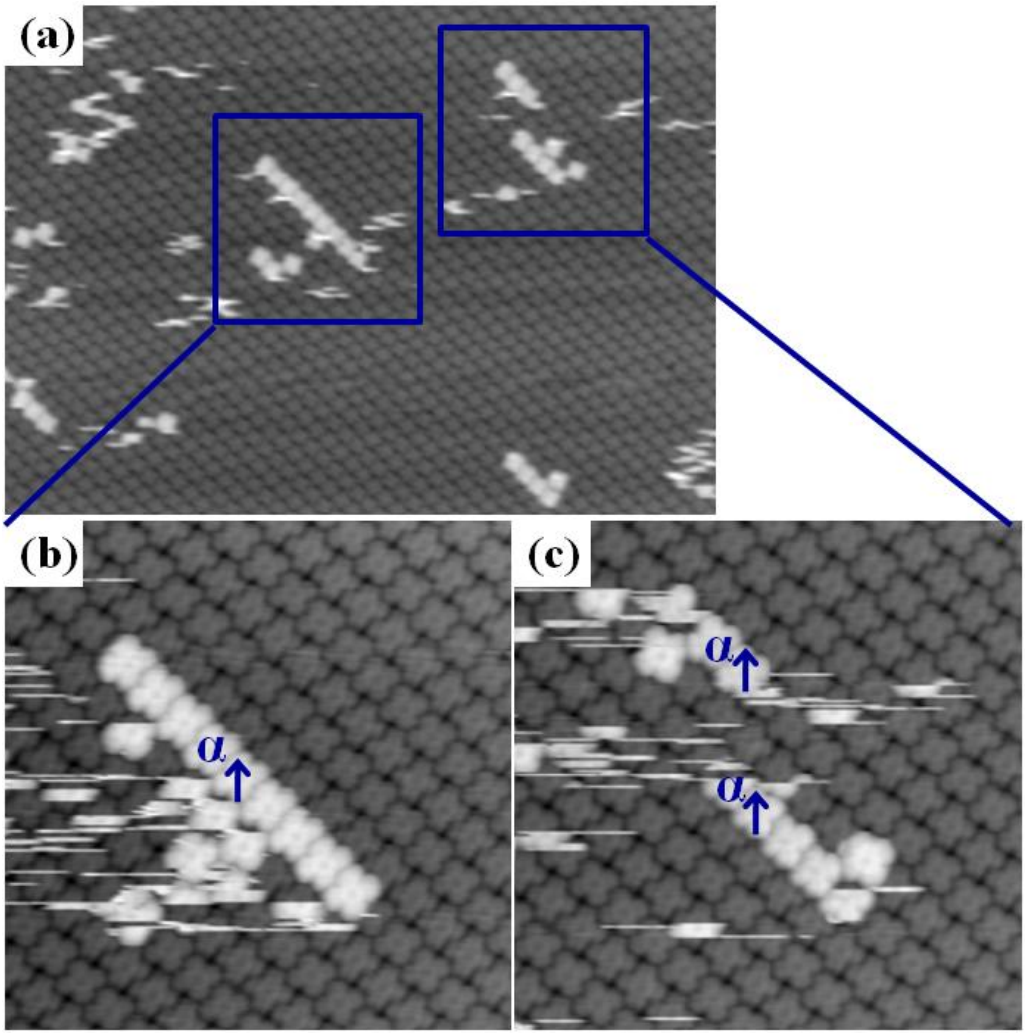

Figure 3.2 (a) Large-scale STM image shows that the F_{16}CuPc second layer starts to grow after the substrate is fully covered by a monolayer (V_{tip} = 2.3 V, 70×50 nm^2). (b) and (c) correspond to zoom-in images enlarged from the regions marked by two blue squares in panel (a) (V_{tip} = 2.5 V, 20×20 nm^2). The 2nd layer F_{16}CuPc molecules preferentially adopt the *α*-orientation.

As the coverage of the 2nd layerF_{16}CuP increases, large bi-layer islands are formed. Figure 3.3a shows the large-scale STM image of the F_{16}CuPc bilayer at 1.6 ML coverage, where most of the molecules in the second layer form large islands with a few vacancy defects. Figure 3.3b is a close-up of the island edge, enlarged from the region highlighted by the rectangle in Figure 3.3a. Horizontal

tip-induced diffusion streaks are still observable in the STM image, suggesting that the lateral bonding of individual F_{16}CuPc molecules to the step edges of the second F_{16}CuPc layer is rather weak. The most notable difference in the growth behaviors of the first and second monolayer lies in their in-plane molecular orientation. As indicated by the blue arrows in Figure 3.3b, the molecules in the second monolayer all adopt the same in-plane orientation, the α-orientation of the underlying layer shown in Figure 3.2. The 2nd layer F_{16}CuPc α-stripe stacks atop the α-phase with lateral displacement between them, while the ones atop the β-stripe adopt an in-plane orientation change to α-phase. Both the slipped and rotational stacking geometries maximize the interlayer π-π interactions between the F_{16}CuPc molecules. After annealing the sample at 150^{o}C for 30mins, the second layer undergoes structural rearrangement and forms a highly ordered phase as shown in Figure 3.3c. A proposed model is shown in Figure 3.3d with rhombic unit cell of $a = b = 1.55 \pm 0.05$ nm and $\varphi = 75 \pm 3°$, and azimuthal angle $\theta = 32 \pm 3°$. Since the in-plane intermolecular interactions in the first and second layer F_{16}CuPc are similar, the different in-plane molecular orientations in these two layers suggest that the interfacial interactions between HOPG and the first F_{16}CuPc layer differ from that between the first and second F_{16}CuPc layers. The coexistence of two different in-plane molecular orientations in the first F_{16}CuPc layer is attributed to the balance between F_{16}CuPc-HOPG interfacial interactions and F_{16}CuPc-F_{16}CuPc intermolecular interactions.

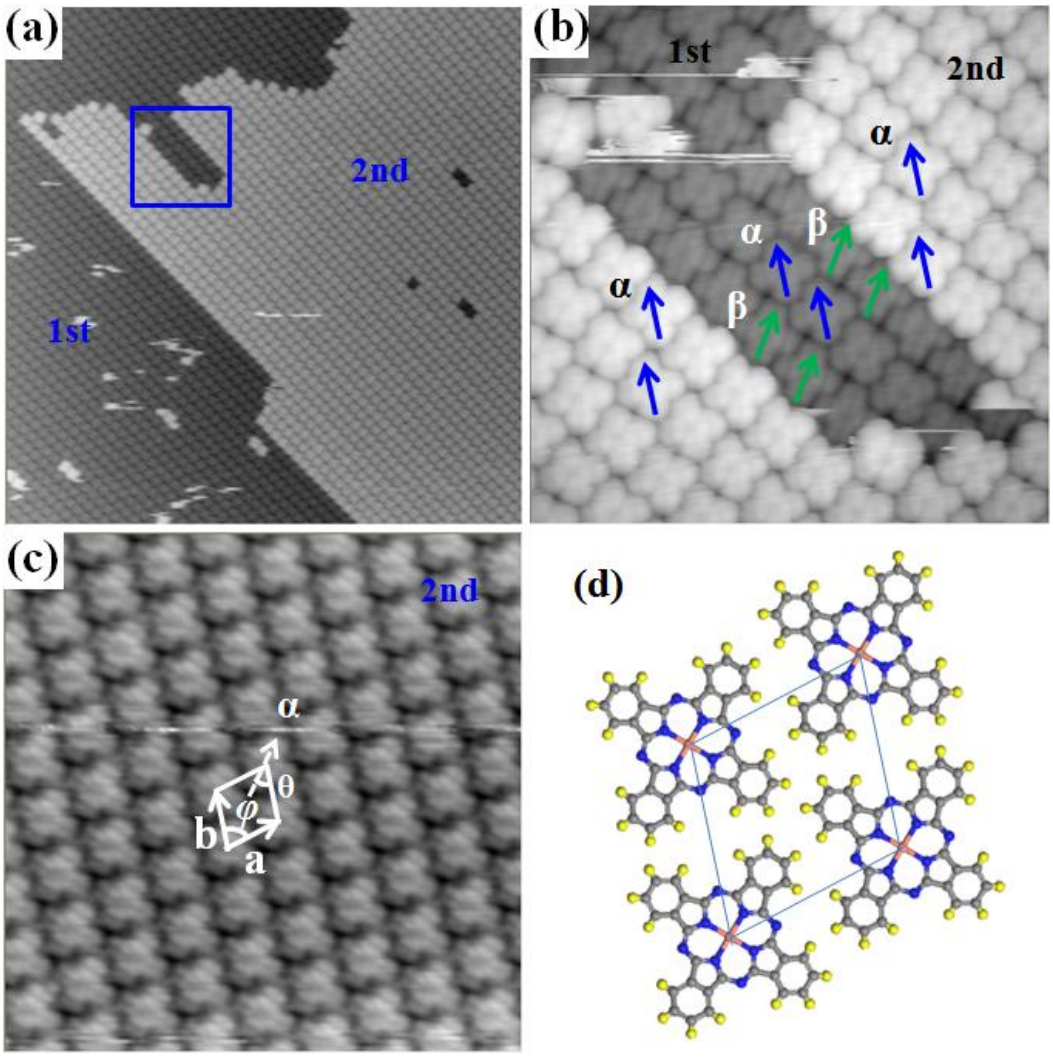

Figure 3.3 (a) STM images of 1.6ML F_{16}CuPc (V_{tip} = 2.5V, 80×80 nm^2), (b) its corresponding close-up at the island edge, as marked by a rectangle in panel (a) (V_{tip} = 2.5V, 15×15 nm^2), and (c) the image of the second layer after annealing (V_{tip} = 2.5V, 15×15 nm^2). (d) The proposed model represents the supramolecular packing structure of the second layer of F_{16}CuPc on HOPG after annealing, as highlighted by the unit cell in panel (c).

3.2.2 NEXAFS measurements of the F_{16}CuPc films

The molecular orientation of a thick F_{16}CuPc film on HOPG is investigated by *in-situ* NEXAFS measurements. NEXAFS is used to monitor the resonance from the core level of a specific atomic species of a molecule (for example, the *K*-shell of nitrogen atoms) to its unoccupied molecular orbitals (π^* and σ^* orbitals).[60] In

principle, the resonance to the unoccupied π^* or σ^* orbital is strong when the electronic field vector ***E*** of the incident linear polarized synchrotron light has a large projection along the direction of the π^* or σ^* orbital, and it vanishes when ***E*** is perpendicular to the π^* or σ^* orbital.[62] For the planar F_{16}CuPc molecule, the σ^* and π^* orbitals are directed essentially in-plane and out-of-plane respectively. Figures 3.4a and b show the angle-dependent N K-edge NEXAFS spectra of 0.5 and 5 nm F_{16}CuPc on HOPG, respectively. The first three sharp absorption peaks (397–404 eV) are assigned to excitations from N 1s core level to individual π^* states, and the broad absorption peaks (404–415 eV) at higher photon energies are transitions to the σ^* states.[23-25, 43-45] The π^* resonances (N K-edge) of F_{16}CuPc are greatly enhanced at grazing incidence and suppressed at normal incidence. As such, the angular dependence of NEXAFS spectra in Figure 3.4 confirms that the F_{16}CuPc molecules in both thin (0.5 nm) and thick (5 nm) films generally adopt the lying-down configuration on HOPG.

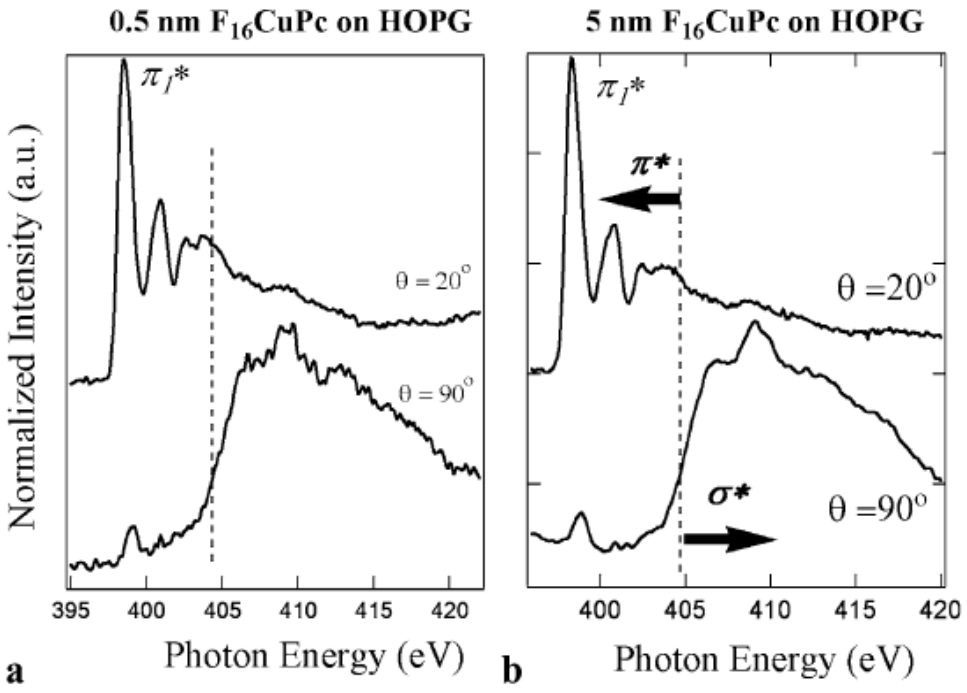

Figure 3.4 Angle-dependent N K-edge NEXAFS spectra of (a) 0.5 nm and (b) 5 nm F_{16}CuPc films on HOPG.

3.3 Ultrathin films of DIP on graphite and SiO_2

The molecular structure of DIP is shown in Figure 3.5. The different growth behaviors of DIP on different surfaces have been reported by other research groups. During the growth on top of F_{16}CuPc thin films, DIP molecules self-organize into organic nanodots with high crystallinity.[61] The growth of DIP on inert substrates such as SiO_2 induces a strong tendency of self-ordering along the long molecular axis to form highly ordered thin films.[62] In the following, we use *in-situ* LT-STM, synchrotron-based high resolution PES and NEXAFS measurements to study the supramolecular packing, molecular orientation and electronic structures of DIP ultrathin films on graphite and SiO_2.[63]

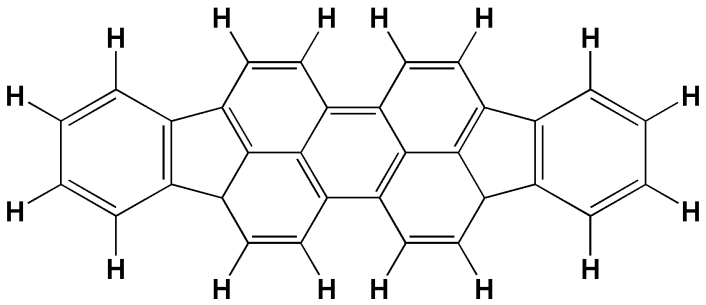

Figure 3.5 Schematic drawing of the DIP molecular structure.

3.3.1 Lying-down DIP monolayer on HOPG studied by STM

We first use LT-STM to understand the molecular packing structure of DIP on HOPG at submonolayer coverages. All the STM images were recorded at 77K. The planar DIP molecules spontaneously aggregate to form single layer islands on HOPG upon deposition at RT. Figure 3.6a shows a typical molecularly resolved 20×20 nm^2 STM image for the long-range ordered DIP monolayer phase, which adopts a distinct "brick-wall" supramolecular arrangement. Figure 3.6b displays the corresponding high resolution STM image, clearly revealing the sub-molecular features of individual DIP molecules originating from their HOMOs. The unit cell is highlighted in Figure 3.6b with $a = 1.23 \pm 0.05$ nm, $b = 1.73 \pm 0.05$ nm, and $\alpha = 40^{o} \pm 2^{o}$. The ellipse in Figure 3.6b represents a single DIP molecule, whose size coincides well with the previously observed flat-lying DIP on Au(111) with their extended π-plane oriented parallel to the substrate surface.[64, 65] Similar to other planar molecules such as PTCDA and CuPc on HOPG,[15, 22, 23] the flat-lying configuration of the planar DIP molecules on HOPG is mainly stabilized through the molecular-substrate interfacial π-π interactions, in particular the

dispersion force. The "brick-wall" supramolecular arrangement also facilitates the close-packing of the monolayer DIP on HOPG.

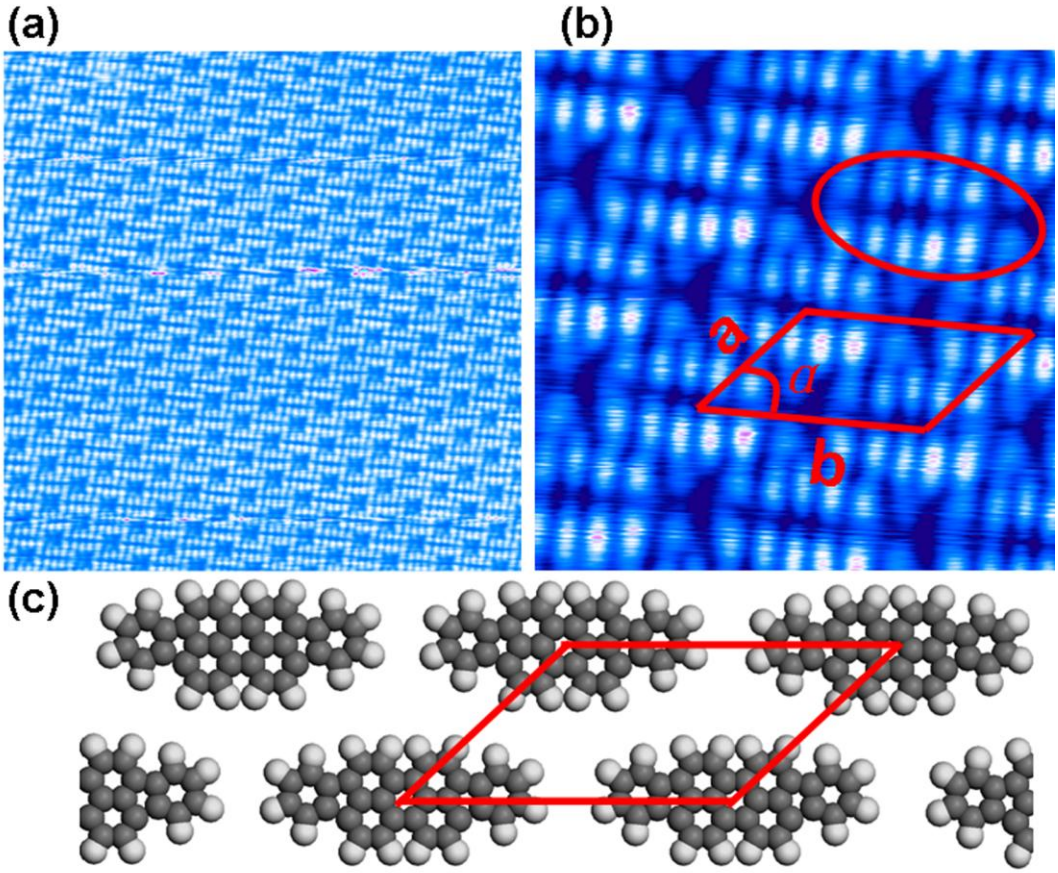

Figure 3.6 STM images for the lying-down DIP monolayer on HOPG: (a) 20 × 20 nm^2 (V_{tip} = 2.4 V) and (b) its corresponding detailed 5×5 nm^2 images (V_{tip} = 2.4 V). (c) Schematic drawing for the proposed molecular packing structure of the lying-down DIP monolayer on HOPG.

3.3.2 DIP thin films on HOPG and SiO_2: PES and NEXAFS measurements

The preferential lying-down configuration of DIP on HOPG was further confirmed by angle-dependent NEXAFS measurements for a thicker DIP film. Figure 3.7a shows the angle-dependent C K-edge NEXAFS spectra of 10 nm DIP on HOPG. The first three sharp absorption peaks at the absorption edge from 284

to 289 eV with grazing incidence light (θ = 20^o) are due to resonant transitions from the C 1s core levels of the various carbon atoms into unoccupied molecular orbitals. As discussed in section **3.2.2**, π^* resonance peaks of planar π-conjugated molecules with a lying-down configuration will be greatly enhanced at grazing incidence since the electronic field vector ***E*** of the incident linear polarized synchrotron light has a large projection along the direction of the π^* orbitals.[60] In Figure 3.7a, the maximum intensity of the π^* resonances is observed at grazing incidence (θ = 20^o); whereas the maximum intensity of the σ^* resonances is observed at normal incidence (θ = 90^o). This indicates that the DIP molecules adopt a lying-down configuration on HOPG with the molecular π-plane slightly tilting away from the HOPG surface plane. In contrast, DIP molecules stand upright on the inert SiO_2 substrate, as revealed by the NEXAFS spectra in Figure 3.7b with a reversed angular dependence. Such standing-up molecular orientation is commonly observed for other planar molecules such as pentacene and CuPc on SiO_2, resulting from the weak interfacial interactions with the inert SiO_2 substrate.[22-25, 33]

Figure 3.7c shows the thickness dependent C K-edge NEXAFS spectra of DIP on HOPG near the π^* absorption region, using clean HOPG and DIP on SiO_2 as references. In order to enhance the contrast of these π^* absorption peaks, we choose the grazing incidence absorption spectra for DIP on HOPG, while using the normal incidence absorption spectrum for DIP on SiO_2. Obviously, the intensity of the first (at 284.4 ± 0.1 eV) and third (at 287.3 ± 0.1 eV) peaks gradually increase upon the sequential deposition of DIP. Figure 3.7d shows the C

1s core level spectrum for 10 nm DIP on HOPG, which possesses a single core level peak at the binding energy of 284.3 ± 0.05 eV. This suggests that the observed three π^* absorption peaks originate from the resonant excitation from this C 1s core level to different unoccupied peaks (π^* peaks). In order to assign these three π^* absorption peaks, we compare the NEXAFS spectra of DIP on HOPG with that of PTCDA thin film on HOPG, which has a similar molecular structure with a perylene core terminated by two anhydride groups.[22, 23, 66, 67] We attribute the first two absorption peaks to the resonance excitation from the C 1s core level to the π^* unoccupied orbitals mainly localized on the perylene core, and the third absorption peak to the resonant excitation to the π^* unoccupied orbitals mainly localized on the two indeno groups.

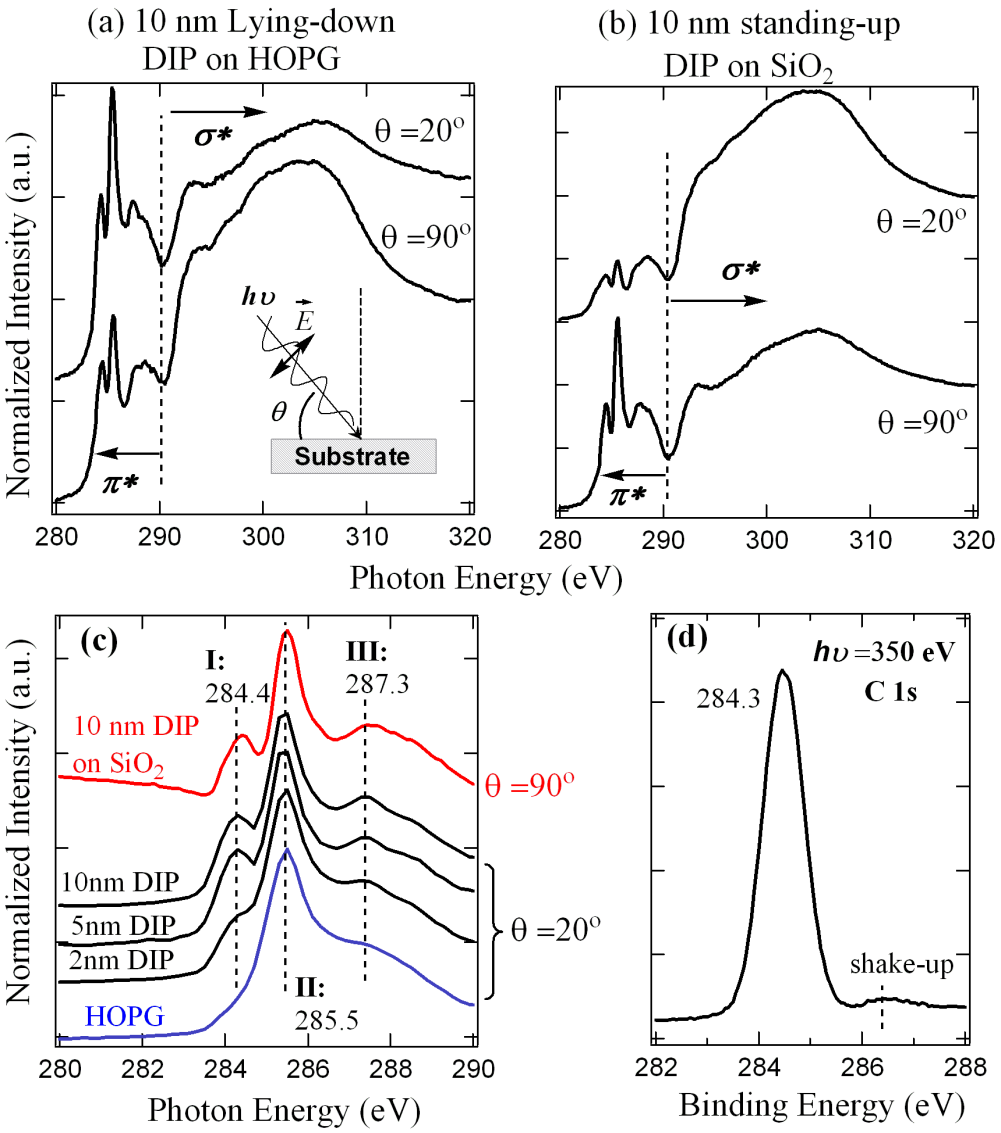

Figure 3.7 C K-edge NEXAFS spectra of 10 nm DIP on (a) HOPG and (b) SiO_2. (c) Thickness dependent C K-edge NEXAFS spectra of DIP on HOPG and on SiO_2. (d) C 1s core level spectrum for 10 nm DIP on HOPG. The binding energy is relative to the Fermi level position of the electron analyzer.

We use *in-situ* high resolution PES to study the orientation-dependent energy level alignment of the standing-up (on SiO_2) and lying-down (on HOPG) DIP thin films. The sample vacuum level shift was determined from PES spectra at the low-kinetic energy onset (secondary electron cut-off) using a photon energy of 60 eV with negative 5 V sample bias. The sample work function ϕ was obtained

through the equation $\phi = h\upsilon - W$, where W is the spectrum width (the energy difference between the substrate Fermi level and low kinetic energy onset).[8-13] Figure 3.8 shows the PES valence band spectra at the low-binding energy region (Figure 3.8a and b), and spectra at the low-kinetic energy region (Figure 3.8c). The hole injection barrier (Δ_h) can be measured from the energy difference between the substrate Fermi level and the HOMO leading edge.[8-13] The IP equals to the sum of Δ_h and sample work function of Φ. As shown in Figure 3.8a, the PES spectra show the apparent angle dependence of the valence band features for DIP films. Both the Φ and Δ_h of the standing up DIP are 0.20 ± 0.05 eV lower than that of the lying-down film. This leads to the deduction that the IP of the standing-up DIP film is 0.40 ± 0.05 eV lower than that of the lying-down film, as shown by the re-plotted valence band PES spectra relative to the vacuum level for both lying-down and standing-up thin films of DIP in Figure 3.8d. The linear extrapolations of the low-binding energy onset correspond to the IP of the films, which are highlighted in Figure 3.8d. The IP is 5.0 ± 0.05 eV for the standing-up DIP film and 5.4 ± 0.05 eV for the lying-down DIP film. Such orientation-dependent IP can be attributed to the intrinsic surface dipoles that originate from the intramolecular dipolar C-H bonds exposed at the surfaces of the standing-up thin film, i.e., an upward pointing surface dipole that reduces the IP, and which has been reported in other ordered molecular thin films.[27, 28, 68-72]

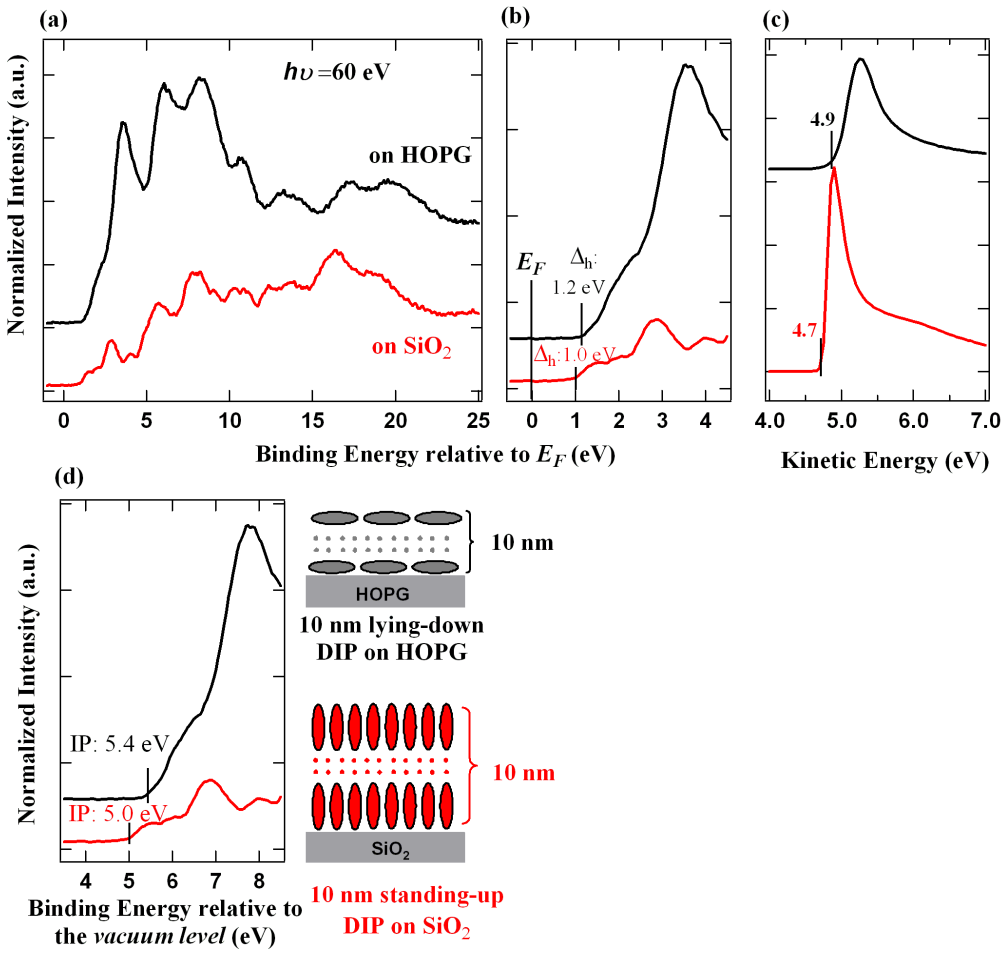

Figure 3.8 Synchrotron PES spectra for lying-down DIP on HOPG and standing-up DIP on SiO_2: (a) valence band spectra at the low-binding energy part and (b) corresponding near the E_F region spectra (all binding energy are relative to the Fermi level position of the electron analyzer), and (c) PES spectra at the low-kinetic energy part (secondary electron cut-off). All spectra are measured with photon energy of 60 eV. (d) Replotted valence band spectra relative to the vacuum level.

3.4 Summary

The initial growth behaviors and the molecular orientations of $F_{16}CuPc$ thin films and DIP thin films on chemically inert HOPG have been studied by LT-STM and NEXAFS measurements. STM images show that the $F_{16}CuPc$ monolayer and DIP monolayer on HOPG adopt the lying-down configuration facilitated by molecule-graphite interfacial π–π interaction. The in-plane

molecular orientations of the F_{16}CuPc and DIP monolayers were also investigated. In the first F_{16}CuPc layer, two different in-plane molecular orientations coexist; in the second layer, all F_{16}CuPc molecules possess the same in-plane orientation. For the DIP monolayer on HOPG, all the molecules are unidirectional and form a long-range ordered "brick-wall" arrangement. NEXAFS measurements revealed that the F_{16}CuPc molecules lie flat on the substrate below 5 nm thickness, and the DIP molecules adopt the lying-down configuration with the molecular plane slightly tilting away from the HOPG surface below 10 nm thickness. In contrast, DIP molecules stand upright on inert SiO_2 due to the weak interfacial interaction. PES experiments were also performed to study the orientation dependence of IPs for the standing-up (on SiO_2) and lying-down (on HOPG) DIP films. The IP for the standing-up DIP film is 0.40 ± 0.05 eV lower than that of the lying-down film, attributed to the intrinsic surface dipoles originating from the intramolecular dipolar C-H bonds exposed at the surfaces of the standing-up thin film.

These detailed investigations of the epitaxial growth of organic molecular films can help us better understand the supramolecular stacking mechanism of π-conjugated planar molecules on surfaces. Such an understanding will enable us to better control the film properties such as supramolecular packing structure and molecular orientation, and hence electronic energy level alignment, which have potential applications in organic electronic devices based on π-conjugated molecules, such as air-stable OFETs or organic solar cells.

Reference:

[1] L. L. Chua, J. Zaumseil, J. F. Chang, E. C. W. Ou, P. K. H. Ho, H. Sirringhaus, R. H. Friend, *Nature* **434**, 194-199 (2005).

[2] S. R. Forrest, *MRS Bulletin* **30**, 28-32 (2005).

[3] F. Yang, M. Shtein, S. R. Forrest, *Nat. Mater*. **4**, 37-41 (2005).

[4] M. A. Muccini, *Nat. Mater*. **5**, 605-613 (2006).

[5] J. A. Rogers, *Science* **291**, 1502-1503 (2001).

[6] J. A. Rogers, Z. Bao, K. Baldwin, A. Dodabalapur, B. Crone, V. R. Raju, V. Kuck, H. Katz, K. Amundson, J. Ewing, P. Drzaic, *Proc. Natl. Acad. Sci. U.S.A*. **98**, 4835-4840 (2001).

[7] C. D. Dimitrakopoulos, P. R. L. Malenfant, *Adv. Mater*. **14**, 99-117 (2002).

[8] H. Ishii, K. Sugiyama, E. Ito, K. Seki, *Adv. Mater*. **11**, 605-625 **(**1999).

[9] A. Kahn, N. Koch, W. Y. Gao, *J. Polymer. Sci. B.* **41**, 2529- 2548 (2003).

[10] C. Cahen, A. Kahn, *Adv. Mater*. **15**, 271-277 (2003).

[11] N. Koch, *ChemPhysChem.* **8**, 1438-1455 (2007).

[12] J. X. Tang, C. S. Lee, S. T. Lee, *J. Appl. Phys.* **101**, 064504 (2007).

[13] N. Koch, *J. Phys. Condens. Matter.* **20**, 184008 (2008).

[14] F. Dinelli, M. Murgia, P. Levy, M. Cavallini, F. Biscarini, *Phys. Rev. Lett*. **92** , 116802 (2004).

[15] S. R. Forrest, *Chem. Rev*. **97**, 1793-1896, (1997).

[16] A. Kraft, R. Temirov, S. K. M. Henze, S. Soubatch, M. Rohlfing, F. S. Tautz, *Phys. Rev. B.* **74**, 041402 (2006).

[17] M. Eremtchenko, J. A. Schaefer, F. S. Tautz, *Nature* **425**, 602-605 (2003).

[18] R. Temirov, S. Soubatch, A. Luican, F. S. Tautz, *Nature*, **444**, 350-353 (2006).

[19] A. Hauschild, K. Karki, B. C. C. Cowie, M. Rohlfing, F. S. Tautz, M. Sokolowski, *Phys. Rev. Lett.* **94**, 036106 (2005).

[20] M. A. Loi, E. Da Como, F. Dinelli, M. Murgia, R. Zamboni, F. Biscarini, M. Muccini, *Nat. Mater.* **4**, 81-85 (2005).

[21] S. Kowarik, A. Gerlach, S. Sellner, F. Schreiber, L. Cavalcanti, O. Konovalov, *Phys. Rev. Lett*. **96**, 125504 (2006).

[22] W. Chen, H. Huang, S. Chen, L. Chen, H. L. Zhang, X. Y. Gao, A. T. S. Wee, *Appl. Phys. Lett*. **91**, 114102 (2007).

[23] W. Chen, H. Huang, S. Chen, L. Chen, H. L. Zhang, X. Y. Gao, A. T. S. Wee, *J. Phys. Chem. C*. **112**, 5036-5042 (2008).

[24] W. Chen, C. Huang, X. Y. Gao, L. Wang, C. G. Zhen, D. C. Qi, S. Chen, H. L. Zhang, K. P. Loh, Z. K. Chen, W. T. S. Wee, *J. Phys. Chem. B.* **110**, 26075-26080 (2006).

[25] W. Chen, S. Chen, D. C. Qi, X. Y. Gao, Z. K. Chen, A. T. S. Wee, *Adv. Funct. Mater*. **17**, 1339-1344 (2007).

[26] N. Koch, A. Gerlach, S. Duhm, H. Glowatzki, G. Heimel, A. Vollmer, Y. Sakamoto, T. Suzuki, J. Zegenhagen, J. P. Rabe, F. Scheiber, *J. Am. Chem. Soc*. **130**, 7300-7304 (2008).

[27] S. Duhm, G. Heimel, I. Salzmann, H. Glowatzki, R. L. Johnson, A. Vollmer, J. P. Rabe, N. Koch, *Nat. Mater*. **7**, 326-332 (2008).

[28] I. Salzmann, S. Duhm, G. Heimel, M. Oehzelt, R. Kniprath, R. L. Johnson, J. P. Rabe, N. Koch, *J. Am. Chem. Soc.* **130**, 12870-12871 (2008).

[29] N. Koch, A. Vollmer, *Appl. Phys. Lett*. **89**, 162107 (2006).

[30] N. Koch, S. Duhm, J. P. Rabe, A. Vollmer, R. L. Johnson, *Phys. Rev. Lett*. **95**, 237601 (2005).

[31] N. Koch, S. Duhm, J. P. Rabe, S. Rentenberger, R. L. Johnson, J. Klankermayer, F. Schreiber, *Appl. Phys. Lett*. **87**, 101905 (2005).

[32] N. Koch, A. Elschner, J. P. Rabe, R. L. Johnson, *Adv. Mate*r. **17**, 330-335 (2005).

[33] S. E. Fritz, S. M. Martin, C. D. Frisbie, M. D. Ward, M. F. Toney, *J. Am. Chem. Soc*. **126**, 4084-4085 (2004).

[34] G. E. Thayer, J. T. Sadowski, F. M. zu Heringdorf, T. Sakurai, R. M. Tromp, *Phys. Rev. Lett*. **95**, 256106 (2005).

[35] B. Crone, A. Dodabalapur, Y.-Y. Lin, R. W. Filas, Z. Bao, A. LaDuca, R. Sarpeshkar, H. E. Katz, W. Li, *Nature* **403**, 521-523 (2002).

[36] F. Zhao, F. Harnisch, U. Schröder, F. Scholz, P. Bogdanoff, I. Herrmann, *Electrochem. Commun.* **7**, 1405-1410 (2005).

[37] M. F. Craciun, S. Rogge, A. F. Morpurgo, *J. Am. Chem. Soc.* **127**,12210-12211 (2005).

[38] N. Papageorgiou, E. Salomon, T. Angot, J.-M. Layet, L. Giovanelli, G. L. Lay, *Prog. Surf. Sci.* **77**, 139-170 (2004).

[39] N. Koch, S. Duhm, J. P. Rabe, A. Vollmer, R. L. Johnson, *Phys. Rev. Lett.* **95**, 237601 (2005).

[40] B. de Boer, A. Hadipour, M. M. Mandoc, T. van. Woudenbergh, P. W. M. Bolm, *Adv. Mater.* **17**, 621-625 (2005).

[41] S. Khodabakhsh, B. M. Sanderson, J. Nelson, T. S. Jones, *Adv. Funct. Mater.* **16**, 95-100 (2006).

[42] Z. A. Bao, A. J. Lovinger, J. Brown, *J. Am. Chem. Soc.* **120**, 207-208 (1998).

[43] W. Chen, L. Wang, D. C. Qi, S. Chen, X. Y. Gao, A. T. S. Wee, *Appl. Phys. Lett.* **88**, 184102 (2006).

[44] W. Chen, H. Huang, S. Chen, L. Chen, H. L. Zhang, X. Y. Gao, A. S. T. Wee, Appl. Phys. Lett. **91**, *114102* (2007).

[45] W. Chen, S. Chen, H. Huang, D. C. Qi, X. Y. Gao, A. T. S. Wee, *Appl. Phys. Lett.* **92**, 063308 (2008).

[46] D. Kurrle, J. Pflaum, *Appl. Phys. Lett.* **92**, 133306 (2008).

[47] A. K. Tripathi, J. Pflaum, *Appl. Phys. Lett*. **89,** 082103 (2006).

[48] J. O. Osso, F. Schreiber, M. I. Alonso, M. Garriga, E. Barrena, H. Dosch, *Org. Electron.* **5**, 135-140 (2004).

[49] D. G. de Oteyza, E. Barrena, *Appl. Phys. Lett*. 87, 183504 (2005).

[50] J. O. Osso, F. Schreiber, V. Kruppa, H. Dosch, M. Garriga, M. I. Alonso, F. Cerdeira, *Adv. Funct. Mater*. **12**, 455-460 (2002).

[51] A. Gerlach, F. Schreiber, S. Sellner, H. Dosch, I. A. Vartanyants, B. C. C. Cowie, *Phys. Rev. B* **71**, 205425 (2005).

[52] Y. Wakayama, *J. Phys. Chem. C* **111**, 2675-2678 (2007).

[53] Y. L. Huang, W. Chen, S. Chen, A. T. S. Wee, *App. Phys. A* **95**, 107-111 (2009).

[54] P. H. Lippel, R. J. Wilson, M. D. Miller, Ch. Wöll, S. Chiang, *Phys. Rev. Lett.* **62**, 171 (1989).

[55] K. W. Hipps, X. Lu, X. D. Wang, U. Mazur, *J. Phys. Chem.* **100**, 11207-11210 (1996).

[56] C. Ludwing, R. Strohmaier, J. Petersen, B. Gompf, W. Eisenmenger, *J. Vac. Sci. Technol. B* **12**,1963-1966 (1993).

[57] S. D. Wang, X. Dong, C. S. Lee, S. T. Lee, *J. Phys. Chem. B* **108**, 1529-1532 (2004).

[58] H. Huang, W. Chen, A. T. S. Wee, *J. Phys. Chem. C.* **112,** 14913-14918 (2008).

[59] X. Chen, Y. S. Fu, S. H. Ji, T. Zhang, P. Cheng, X. C. Ma, X. L. Zou, W. H. Duan, J. F. Jia, Q. K. Xue, *Phys. Rev. Lett.* **101**, 197208 (2008).

[60] J. Stöhr, *NEXAFS spectroscropy*, Springer-Verlag: Berlin; New York (1992).

[61] E. Barrena, D. G. de Oteyza, S. Sellner, H. Dosch, J. O. Ossó, B. Struth, *Phys. Rev. Lett*. **97**, 076102 (2006).

[62] A. C. Durr, F. Schreiber, M. Munch, N. Karl, B. Kause, V. Kruppa, H. Dosch, *Appl. Phys. Lett*. **81**, 2276 (2002).

[63] Y. L. Huang, W. Chei, H. Huang, D. C. Qi, S. Chen, X. Y. Gao, J. Pflaum, A. T. S. Wee, *J. Phys. Chem. C* **113**, 9251-9255 (2009).

[64] E. Barrena, D. G.de Oteyza, H. Dosch, Y. Wakayama, *ChemPhyChem*, *8*, 1915-1918 (2007).

[65] D. G. de Oteyza, E. Barrena, M. Ruiz-Oses, L. Silanes, B. P. Doyle, J. E. Ortega, A. Arnau, H. Dosch, Y. Wakayama, *J. Phys. Chem. C*. **112**, 7168-7172 (2008).

[66] Y. Zou, L. Kilian, A. Schöll, Th. Schmidt, R. Fink, E. Umbach, *Surf. Sci*. 6**00**, 1240-1251 (2006).

[67] A. Schöll, Y. Zou, D. Huebner, S. G. Urquhart, Th. Schmidt, R. Fink, E. Umbach, *J. Chem. Phys.* **123**, 044509 (2005).

[68] J. Ivanco, B. Winter, F. P. Netzer, M. G. Ramsey, *Adv. Mater.* **15**, 1812-1815 (2003).

[69] J. Ivanco, F. P. Netzer, M. G. Ramsey, *J. Appl. Phys*. **101**, 103712 (2007).

[70] J. Ivanco, T. Haber, J. P. Krenn, F. P. Netzer, R. Resel, M. G. Ramsey, M. G. *Surf. Sci.* **601**, 178-187 (2007).

[71] H. Fukagawa, H. Yamane, T. Kataoka, S. Kera, M. Nakamura, K. Kudo, N. Ueno, N. *Phys. Rev. B.* **73**, 245310 (2006).

[72] W. Chen, H. Huang, S. Chen, Y. L. Huang, A. T. S. Wee, *Chem. Mater*. **20**, 7017-7021 (2008).

Chapter 4

2D Binary Molecular Networks Stabilized by Intermolecular Hydrogen-bonding on Graphite

4.1 Introduction

Molecular self-assembly on surfaces or surface-supported nanotemplates represents a versatile way to create tunable supramolecular architectures with desired functionality for potential applications in nano-devices, such as biosensors, molecular and organic electronics.[1-9] Selective coupling of functional molecules to preferential adsorption sites on supporting surfaces facilitates the creation of long-range ordered 2D molecular arrays.[6-16] By rational design and selection of molecular building blocks, various non-covalent/covalent intermolecular interactions can be utilized to steer the formation of supramolecular networks with good structural stability. A wide range of 2D molecular nanostructures, such as molecular supergratings, porous networks, and other regular molecular arrays, have been constructed by the directionality of selective intermolecular hydrogen bonding, metal-ligand interactions as well as covalent bonding (Chapter **1.2.3**).[17-36] To increase the functionality and tunability of molecular nanostructure arrays, intensive effort has been devoted to the construction of multi-component nanostructures, whose overall arrangements could be tuned by varying the

molecular intermixing ratios as well as the molecular building blocks.[37-43] In this chapter, a novel approach to construct tunable and robust 2D binary molecular nanostructures stabilized by intermolecular hydrogen bonding on graphite surfaces will be demonstrated.

The binary molecular systems studied here include F_{16}CuPc intermixing with CuPc, 6P, pentacene and DIP, respectively. The F_{16}CuPc molecule could offer electronegative peripheral F atoms and the rests offer electropositive peripheral H atoms to form intermolecular C-F···H-C hydrogen bonds in these binary systems. Strong molecule-substrate interfacial interactions can induce the locking of adsorbed molecules at specific adsorption sites on the substrates, and thereby the final supramolecular arrangements are constrained by the substrate symmetry.[44-46] In contrast, on the inert graphite surface, π-conjugated organic molecules have less tendency to bind to specific adsorption sites, and thereby have greater lateral degrees of freedom to assemble at their formation energy minima.[47, 48] Using *in-situ* LT-STM imaging, we find that the supramolecular packing structure of the binary networks can be effectively controlled by experimental parameters such as the molecular geometry (size and shape) and relative molecular ratios. Furthermore, theoretical simulations based on molecular dynamics (MD) and density functional theory (DFT) were employed to evaluate the intermolecular binding energies and to rationalize the stability of these networks. The simulated results further confirm that these tunable binary molecular arrays are stabilized by intermolecular hydrogen bonding.

4.2 Self-assembled CuPc/F_{16}CuPc binary superstructures

4.2.1 The F_{16}CuPc monolayer and CuPc monolayer on HOPG

We first investigate the packing structures of monolayer F_{16}CuPc and monolayer CuPc adsorbed separately on HOPG (detailed analysis of monolayer F_{16}CuPc on HOPG has been discussed in Chapter **3.2**). In Figure 4.1, the left column shows the F_{16}CuPc monolayer while the right column shows the CuPc monolayer.[49, 50] Both F_{16}CuPc and CuPc molecules lie flat on HOPG with their molecular planes parallel to the substrate due to the interfacial π-π interaction. Similar to other phthalocyanines and their derivatives, the characteristic STM images of both F_{16}CuPc and CuPc single molecules appear as four-leaved patterns.[45, 51] The supramolecular arrangement of the F_{16}CuPc monolayer comprises alternating α- and β- stripes, where α and β refer to two different in-plane molecular orientations. An azimuth angle θ is defined as the angle between the molecular axis and the strip direction (dashed line). As denoted by the blue arrows in Figure 4.1c, the α-stripe has $\theta_1 = 32 \pm 3°$ and β-stripes with $\theta_2 = 62 \pm 3°$ respectively. Though the percentages of α- and β- stripes are nearly equivalent, the packing sequence of these α- and β- stripes lacks long-range ordering. The periodicity along the F_{16}CuPc α- or β- stripe is about 1.55 nm. The CuPc molecules are unidirectionally orientated and form a close-packed monolayer with four-fold symmetry (Figure 1b and 1d); the 1.50×1.50 nm^2 square unit cell is highlighted in Figure 1d. The difference in the packing structures for the unfluorinated and fluorinated copper phthalocyanine monolayers on HOPG is

attributed to the large repulsive forces between the negatively charged peripheral F atoms of neighboring F_{16}CuPc molecules.

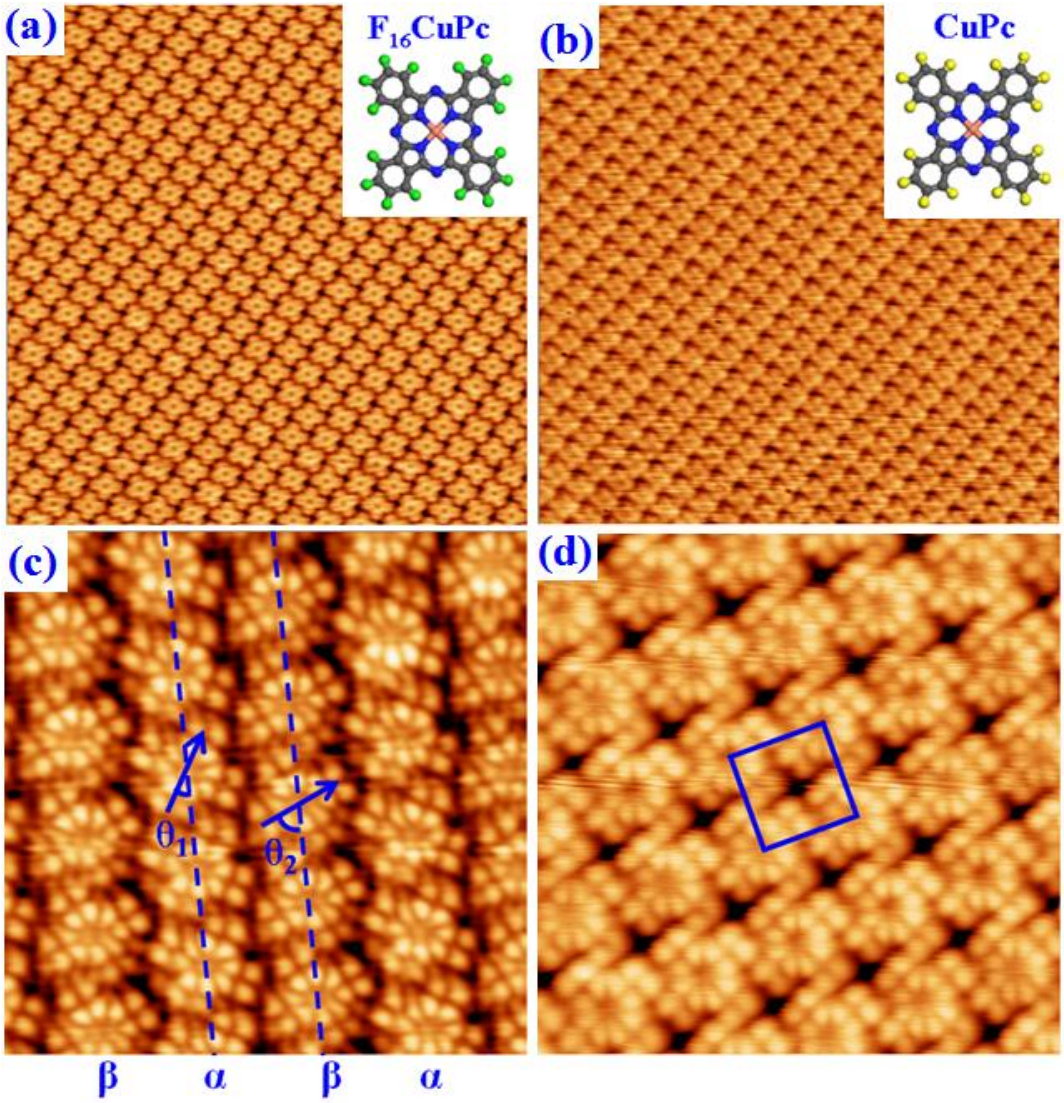

Figure 4.1 STM images of (a) F_{16}CuPc monolayer (V_{tip}= 2.0 V, 30×30 nm^2) and (b) CuPc monolayer (V_{tip}= 1.9 V, 30×30 nm^2) on HOPG; (c) and (d) are the corresponding 8×8 nm^2 close-ups. The insets in (a) and (b) show the molecular structures of F_{16}CuPc and CuPc, where green spheres represent F atoms and yellow ones represent H atoms.

4.2.2 CuPc/F_{16}CuPc packing structures at different molecular coverages

In Figure 4.2a, the molecularly resolved 50×25 nm^2 STM image shows the F_{16}CuPc monolayer randomly decorated by the insertion of a low coverage of

CuPc molecules (~ 0.05 ML). The few brighter features are assigned to CuPc molecules. The overall arrangement of F_{16}CuPc monolayer on HOPG, namely alternating α- and β- stripes, is preserved. As highlighted in the insert of Figure 4.2a (circled area), the orientations of the CuPc molecules are determined by the host F_{16}CuPc stripes. That is, the CuPc molecule adopts α- or β- orientation (green or purple arrows), according to the orientation of the F_{16}CuPc stripe. The population of CuPc molecules inserted into the F_{16}CuPc α-strip is much larger than that inserted into the β-strip (~70% for α-orientation and ~30% for β-orientation counted over less than 100 CuPc molecules; these insertion probabilities are estimated to about 10% accuracy), suggesting that the insertion of CuPc molecules into α-domain of F_{16}CuPc is more energetically favorable. The bias-dependent images in Figure 4.2b-e correspond to the blue square in panel 2a, where the two arrows in each image indicate the CuPc molecules. In the tip-bias range of -1.3 V to 2.0 V, the CuPc molecules appear brighter at positive bias (Figure 4.2b, c), but dimmer at negative bias (Figure 4.2d, e) as compared to the surrounding F_{16}CuPc molecules. Visual inspection of the high resolution STM images of CuPc and F_{16}CuPc indicates that they both have four-fold symmetry and lie flat on HOPG. The contrast difference between the CuPc and F_{16}CuPc molecules is not due to charge transfer or polarization at the molecule/graphite interfaces, since CuPc and F_{16}CuPc interact with inert graphite mainly via π-π interactions. The observed reversed image contrast of CuPc, i.e., brighter features at positive tip bias and dimmer features at negative tip bias, precludes the explanation that CuPc molecules adsorb at different geometrical height as

compared to F_{16}CuPc. STM images recorded at positive tip bias originate from electrons tunneling from the HOMOs into the tip Fermi level, while the images recorded at negative tip bias are due to the electrons tunneling from the tip Fermi level into the LUMOs. As measured from PES, the energy difference between the substrate Fermi level and the CuPc HOMO is smaller than that for F_{16}CuPc.[52, 53] Hence, a larger available population of electrons from the CuPc occupied states could tunnel to the tip Fermi level under positive tip bias, leading to the brighter CuPc images. By a similar argument, the CuPc molecules appear dimmer at negative tip bias because the LUMO of CuPc is further away from the Fermi level than F_{16}CuPc LUMO.

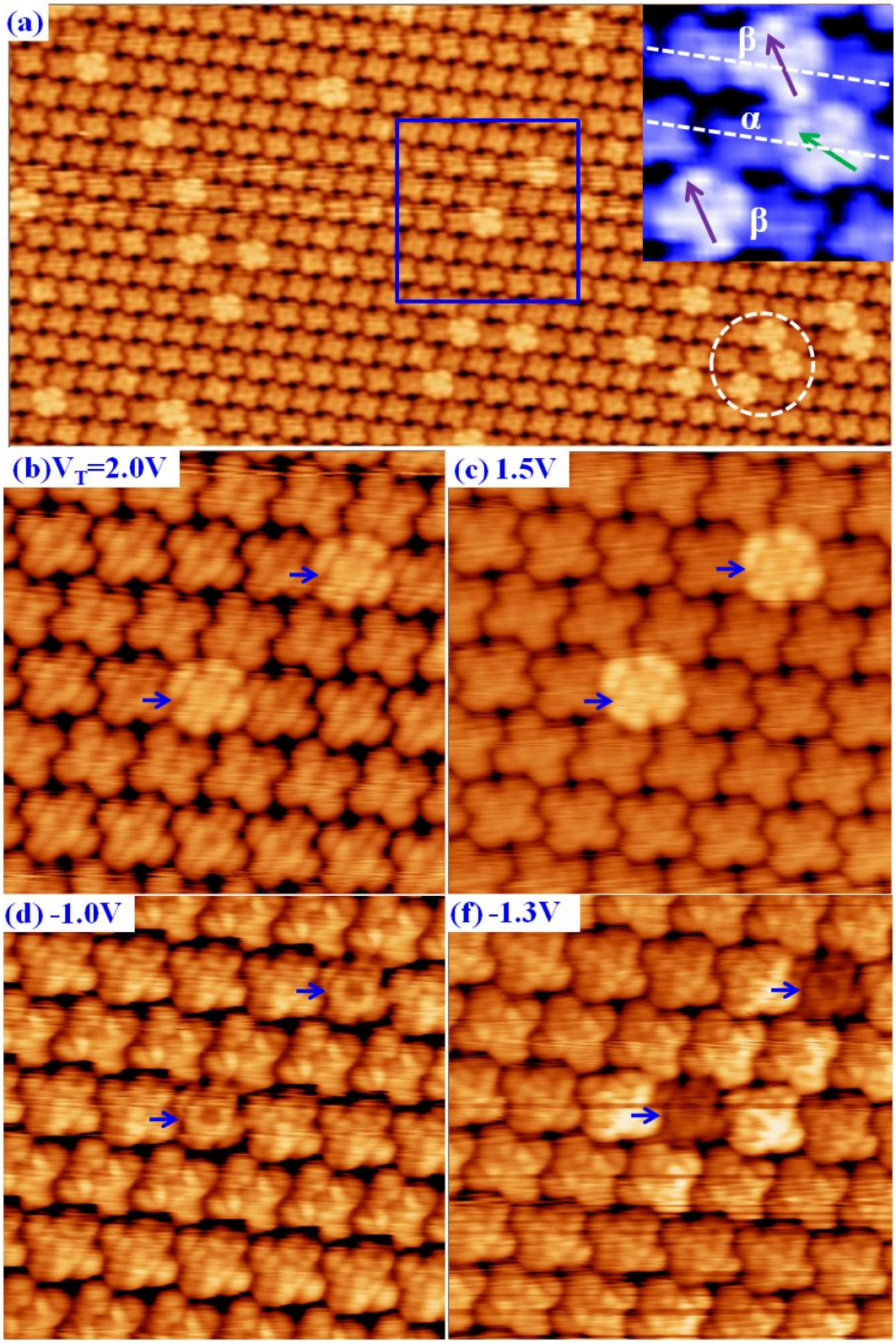

Figure 4.2 (a) STM images of 0.05ML CuPc randomly embedded into the F_{16}CuPc monolayer on HOPG, where CuPc molecules appearing as brighter features at V_{tip}= 2.0 V (25×50 nm^2). The 5×5 nm^2 inset highlights that the CuPc molecules adopt two different in-plane molecular orientations. (b)-(e) are bias-dependent 10×10 nm^2 images (I_{set}=0.1nA for all four images) with V_{tip}=2.0, 1.5, -

1.0 and -1.3 V, respectively, highlighted by the blue square in panel a, where the CuPc molecules are indicated by blue arrows in each image.

The packing structure of the CuPc/F_{16}CuPc monolayer on HOPG is dynamic and is modified at different molecular coverages. As shown in Figure 4.3a, when the local molecular coverage is about 0.4 ML for CuPc (brighter molecules) and 0.6 ML for F_{16}CuPc, short-range ordered binary domains comprising alternate bright and dim molecules form, coexisting alongside predominantly F_{16}CuPc domains with irregular boundaries. The 8×8 nm^2 high resolution image in Figure 4.3b displays the molecularly-resolved packing structure of the ordered domain marked by the blue rectangle in panel 4.3a. This CuPc/F_{16}CuPc binary network assembles into a chessboard-like pattern at the intermixing ratio of 1:1, where the in-plane orientation of both CuPc and F_{16}CuPc molecules are unidirectional. As each F_{16}CuPc molecule is surrounded by four CuPc molecules, the lateral binding interactions between the neighboring CuPc and F_{16}CuPc molecules is maximized. The lower left of Figure 4.3a shows the predominantly F_{16}CuPc domain, comprising F_{16}CuPc stripes decorated by a few CuPc molecules in their original α- or β- in-plane orientation. The white dashed lines in Figure 4.3a and b mark the alignment of F_{16}CuPc stripes. We note that in the chessboard-like CuPc/F_{16}CuPc network, all the molecules adopt the α-orientation as indicated by the arrow in Figure 4.3b. The random insertion of CuPc molecules at low CuPc coverages is due to the geometrical similarity (shape and size) of CuPc and F_{16}CuPc, ensuring that the replacement of individual host molecule (F_{16}CuPc) by the guest molecule (CuPc) does not induce any local structural rearrangement. Some bright

protrusions (indicated by the white circle in Figure 4.3a) appear as single molecules or in four-molecule clusters are due to F_{16}CuPc or CuPc molecules adsorbed on the second layer.

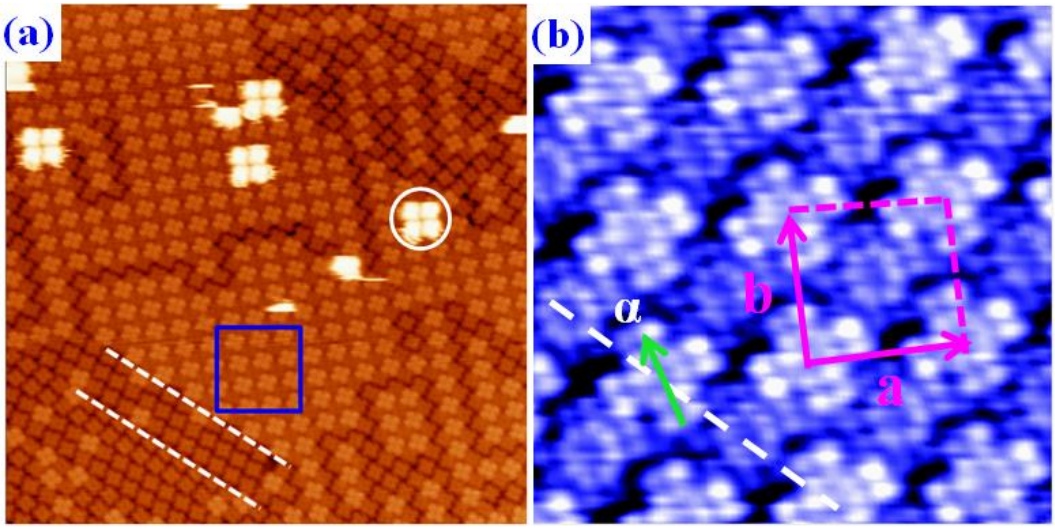

Figure 4.3 (a) STM images showing the self-assembled superstructures of 0.6ML F_{16}CuPc with 0.4ML CuPc (V_{tip}= 3.0V, 50×50 nm^2) and (b) the molecular-resolved image corresponds to the blue square in panel (a) (V_{tip}=3.0V, 8×8 nm^2). The white dashed lines present the orientation of F_{16}CuPc α- or β-stripes.

The large-scale 100×100 nm^2 STM image in Figure 4.4a shows that 1:1 CuPc/F_{16}CuPc islands with irregular shape form after the co-deposition of 0.75ML CuPc and 0.85ML F_{16}CuPc on HOPG. The line profile in Figure 4.4b corresponding to the blue line in panel 4.4a, reveals that the height of this island is about 0.28nm. This coincides well with the layer height of the F_{16}CuPc or CuPc monolayer with flat-lying configuration. As such, these bright islands can be attributed to a second layer. The molecularly resolved STM image in Figure 4.4c demonstrates that the island is composed of a chessboard-like network, similar to that observed in Figure 4.3b for the first monolayer. Their rhombic cells are

drawn in Figure 4.3b and 4.4c with dimensions of $a = b = 2.20 \pm 0.05$ nm and $\alpha = 88° \pm 3°$. The supramolecular arrangement in the exposed first layer is a mixture of chessboard-like networks with less-intermixing domains, similar to that shown in Figure 4.3a. STM is unable to image the molecular superstructure of the first layer underneath the islands, which is believed to play an important role in facilitating the formation of the chessboard-like second layer.

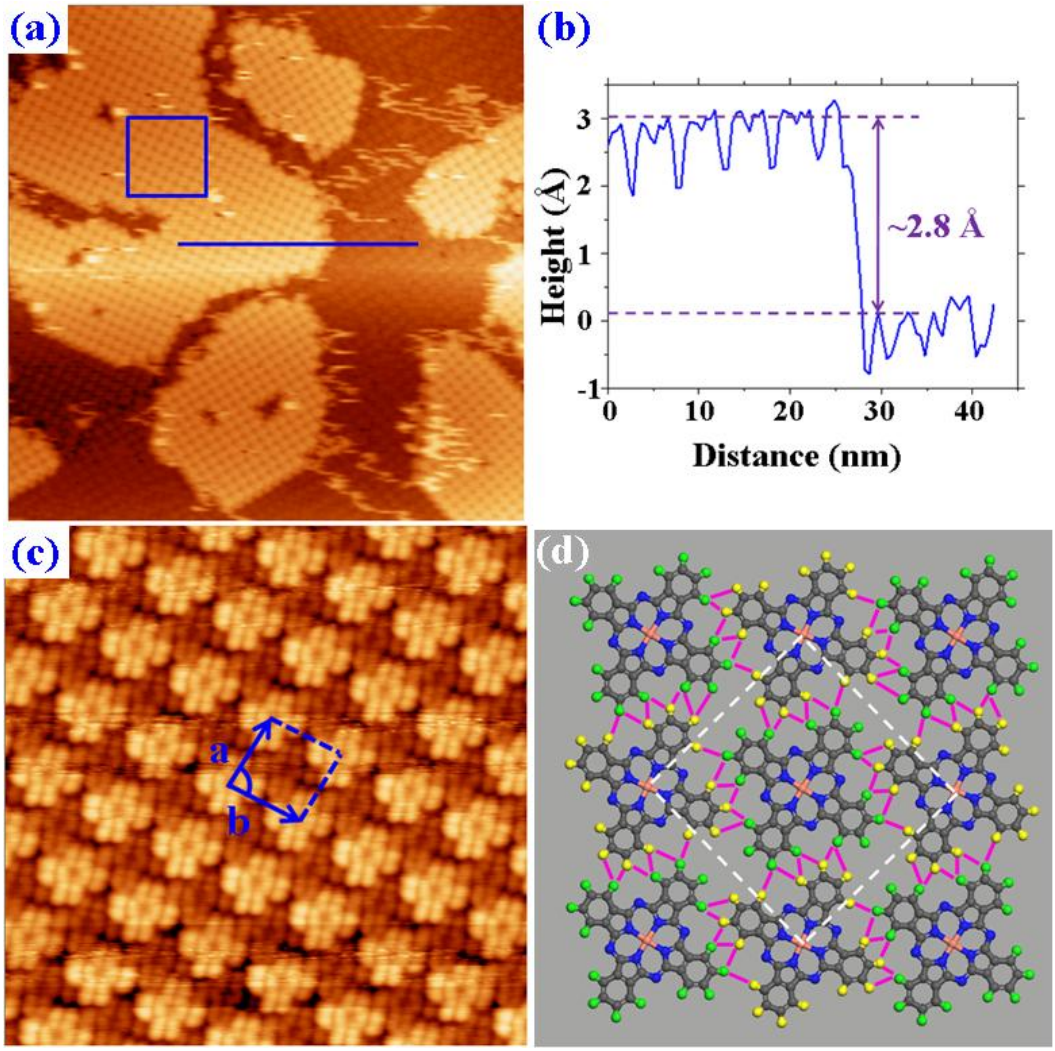

Figure 4.4 (a) The large scale STM image shows the self-assembled superstructure of 0.85ML F_{16}CuPc with 0.75ML CuPc (V_{tip}= 2.6V, 100×100 nm^2), and (b) its corresponding line profile. (c) The high-resolution STM image corresponds to the blue rectangle in panel (a) illustrates the detailed supramolecular packing structure of CuPc/F_{16}CuPc binary network with intermixing ratio of 1:1. The MD simulated model is shown in (d), where pink lines highlight the possible intermolecular hydrogen bonds.

4.2.3 Simulated packing structure of the chessboard-like pattern

To investigate the structural stability and flexibility of the 1:1 CuPc/F_{16}CuPc networks, we performed a force field based MD simulation on the chessboard-like pattern on HOPG slabs. The MD simulation is performed in NVT ensemble at 77 K. A modified consistent valence force field (CVFF) is employed in the Material Studio package,[54] and the atomic charges are the Mulliken[55] charges obtained from DFT calculations of a single molecule, which is calculated on B3LYP[56, 57]/6-31G(d) level with Gaussian03[58] package. The MD snapshot is shown in Figure 4.4d, where every F_{16}CuPc (CuPc) molecule is surrounding by four CuPc (F_{16}CuPc) molecules side-by-side to form a square unit cell. The dimensions of the simulated unit cell are $a = b = 2.30$ nm and $\alpha = 89°$, in agreement with STM experimental measurements (2.20 ± 0.05 nm and $\alpha = 88° \pm 3°$). In the simulation, the partial charges of C-F (C: 0.27, F: -0.26) bonds in F_{16}CuPc and C-H (C: -0.16, H: 0.14) bonds in CuPc cause them to have opposite bond polarization directions, so the chessboard-like structure is stabilized by attractive dipole-dipole interaction between neighboring CuPc and F_{16}CuPc molecules. This electrostatics interaction is a hydrogen bonding interaction, since the average F···H distance (the distance between F_{16}CuPc peripheral fluorine atoms and the CuPc peripheral hydrogen atoms) is ~ 2.65 Å, with the C-H···F-C angle larger than 120°, which falls within the range of the weak hydrogen bond.[59] The possible intermolecular hydrogen bonds are highlighted by the purple short lines in Figure 4.4d. These electrostatic interactions preserve the F_{16}CuPc α- and β- stripes in the dilute CuPc domains as the F_{16}CuPc-F_{16}CuPc intermolecular interactions are still dominant. When the

CuPc:F_{16}CuPc ratio is 1:1, the unidirectional chessboard-like pattern is preferred as it maximizes CuPc-F_{16}CuPc interactions and minimizes the formation energy.

4.3 Tunable 2D binary molecular networks

4.3.1 Flexible F_{16}CuPc dot arrays with different embedding molecular spacer

As discussed in the CuPc/ F_{16}CuPc binary system, the intermolecular C-H···F-C hydrogen bonding can be utilized to fabricate well-ordered supramolecular structures with good structural stability. It also demonstrated that the local molecular environment is very crucial to control the arrangement of the binary molecular self-assembly. In the following sections, we will investigate the tunability of binary molecular networks by varying the molecular geometry (size and shape) as well as the relative molecular ratios, demonstrated by binary combinations of F_{16}CuPc with 6P, pentacene, or DIP, whose molecular structures are shown in Figure 4.5a. It is expected that the formation of multiple intermolecular C-F···H-C hydrogen bonds between the electronegative peripheral F atoms of F_{16}CuPc and the electropositive peripheral H atoms of 6P, pentacene or DIP, could facilitate the ordered supramolecular assemblies of these binary molecular systems. As illustrated in Figure 4.5b, the intermolecular separations of F_{16}CuPc dot arrays could be tuned by embedding different molecular spacers for their different shapes and sizes.

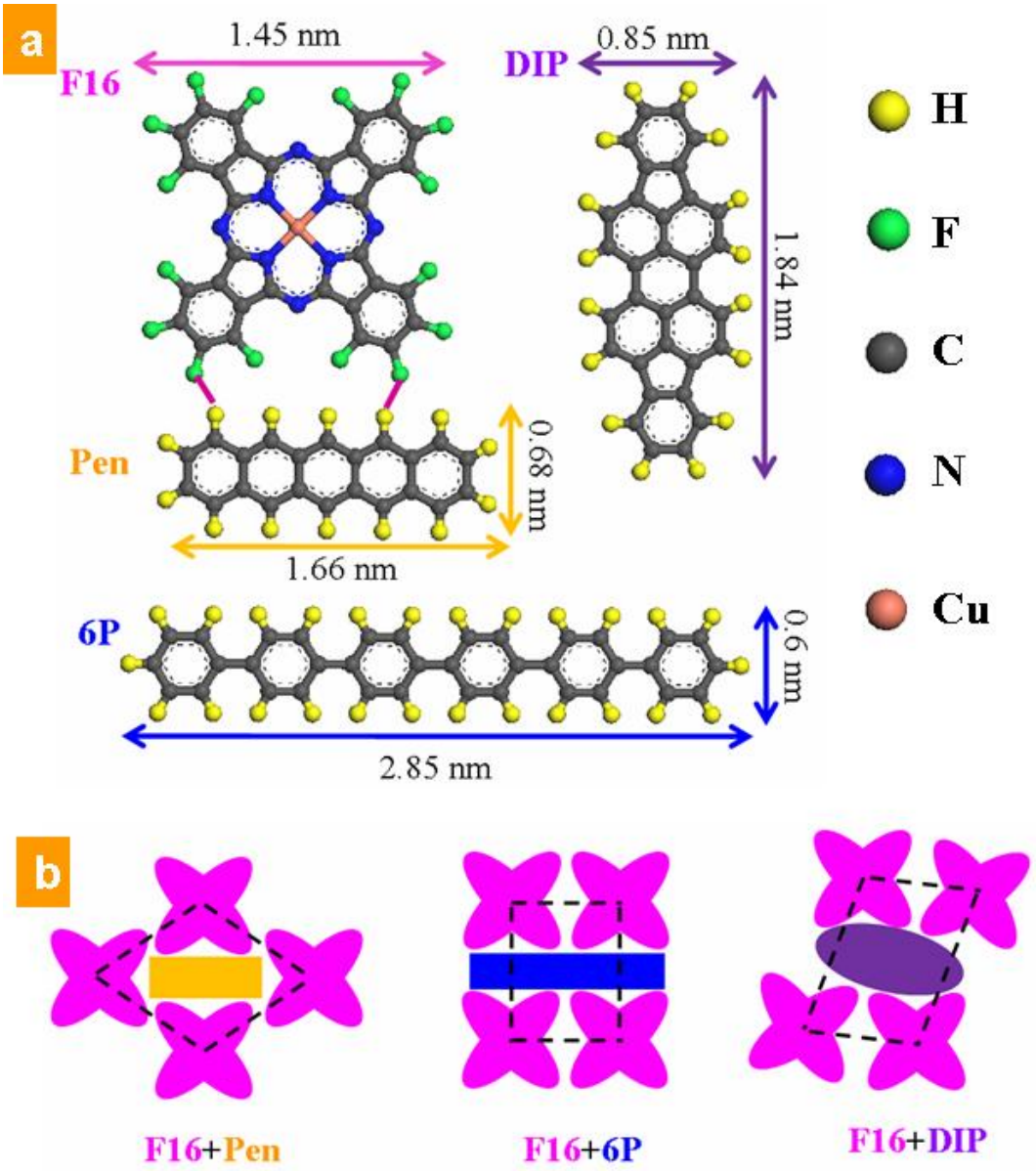

Figure 4.5 (a) Molecular structures of F_{16}CuPc (F16), pentacene (Pen), 6P and DIP. The short pink lines between F_{16}CuPc and pentacene represent the possible C-F···H-C intermolecular hydrogen bonds. (b) The proposed arrangements of F_{16}CuPc dot arrays with pentacene (**F16+Pen**), 6P (**F16+6P**) and DIP (**F16+DIP**) respectively. The intermolecular seperations indicated by black dashed lines are tunable by varying the geometrical parameters of the embedded molecules.

4.3.2 6P:F_{16}CuPc binary networks

The first binary system presented is F_{16}CuPc embedded in 6P molecular matrix. As shown by the high-resolution STM images in Figure 4.6a-c, the long rod-like

feature represents a single 6P molecule, and four-lobe feature represents an F_{16}CuPc molecule. Both F_{16}CuPc and 6P molecules lie flat on HOPG with their conjugated π-plane oriented parallel to the HOPG surface due to interfacial π-π interactions, consistent with previous reports.[60, 61] Figure 4.6a shows the molecularly resolved STM image (15×15 nm^2) of the binary molecular packing structure with 6P:F_{16}CuPc ratio of 1:2. Two F_{16}CuPc doublets are interlinked by a single 6P molecule, forming oblique F_{16}CuPc molecular dot arrays with well-defined intermolecular distances represented by an approximately rectangular cell with a_1 = 1.55±0.05 nm, b_1 = 2.27±0.05 nm and α_1 = 92.0°±2° (the tetragon cells noted in the STM images of Figure 4.6, 4.7 and 4.9 are referred to the separations of two F_{16}CuPc dimmers, but not primitive cells of the molecular arrays). The supramolecular packing structure of this F_{16}CuPc dot array is consistent with the expected tessellation for the 6P:F_{16}CuPc binary system (denoted as **F16+6P** in Figure 4.5b). The smooth surface potential of HOPG ensures that the 2D network can tolerate small lateral and rotational molecular motion to reach the formation energy minima during self-assembly. The intermolecular distance of the F_{16}CuPc dot array can be manipulated by controlling the 6P:F_{16}CuPc molecular ratio. At higher 6P:F_{16}CuPc molecular ratio of 1:1, a 6P doublet bridges two F_{16}CuPc doublets, thereby forming an F_{16}CuPc array with larger oblique cell with a_2 = 1.60±0.05 nm, b_2 = 2.99±0.05 nm and α_2 = 96.0°±4° as shown in Figure 4.6b. By further increasing the 6P:F_{16}CuPc molecular ratio to 3:1 (Figure 4.6c), the enlarged oblique F_{16}CuPc molecular dot array forms two F_{16}CuPc doublets interconnected by a 6P triplet forming an approximately rectangular cell with a_3 =

2.35 ±0.05 nm, b_3 = 3.91 ±0.05 nm and α_3 = 91.0 °±2 °. This series of experiments clearly demonstrate the geometrical tunability of the F_{16}CuPc molecular dot arrays by controlling the 6P:F_{16}CuPc molecular ratios. The corresponding simulated molecular superstructures are given below each STM image in Figure 4.6 (simulation details will be discussed later). The possible intermolecular C-F···H-C hydrogen bonds with F···H distances of ~2.5-2.6 Å are highlighted by the pink lines, the bond lengths of which are typical of weak hydrogen bonds.[59]

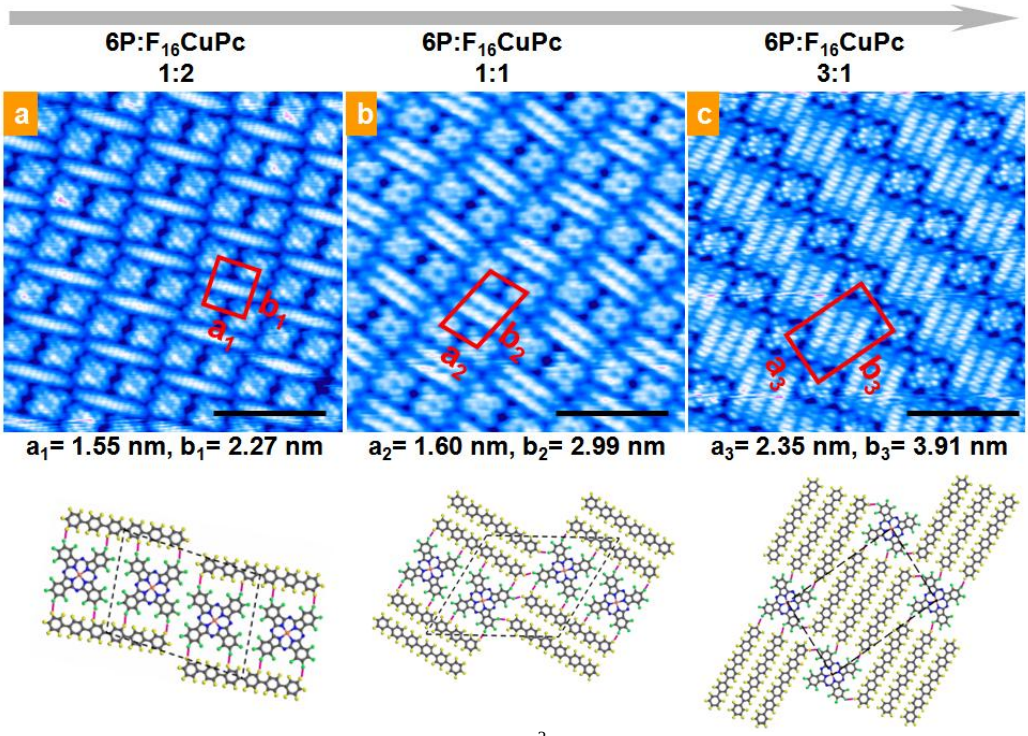

Figure 4.6 Top: Molecularly-resolved 15 × 15 nm^2 STM images of the oblique F_{16}CuPc molecular dot arrays with tunable intermolecular distance controlled by the 6P coverage. The oblique F_{16}CuPc molecular dot arrays comprise two F_{16}CuPc doublets interlinked (a) by a 6P monomer molecule at low 6P coverage 6P:F_{16}CuPc=1:2 (V_{tip} = 2.0 V); (b) by a 6P doublet by increasing the molecular ratio of 6P:F_{16}CuPc to 1:1 (V_{tip} = 2.0 V); and (c) by a 6P triplet at the high 6P coverage of 6P:F_{16}CuPc=3:1 (V_{tip} = 2.7 V). The scale bar in each STM image represents 5 nm. **Bottom:** The simulated molecular packing structures of the different oblique F_{16}CuPc molecular dot arrays. The pink short lines between F_{16}CuPc and 6P represent the possible C-F···H-C intermolecular hydrogen bonds. The dashed parallelograms indicate the primitive unit cells.

4.3.3 PEN:F_{16}CuPc binary networks

The second system is shown in Figure 4.7, whereby the intermolecular separation of the F_{16}CuPc molecular dot array is manipulated by intermixing F_{16}CuPc with pentacene (Pen), whose molecular length is almost half the length of 6P (Figure 4.5). Figure 4.7 shows selected molecularly-resolved 10×10 nm^2 STM images of the supramolecular packing structures at different Pen:F_{16}CuPc ratios. The bright short rod-like feature represents a single pentacene molecule. The oblique cell of $c_1 = 1.84 \pm 0.05$ nm, $d_1 = 1.86 \pm 0.05$ nm and $\beta_1 = 79.0° \pm 2°$ at Pen:F_{16}CuPc ratio of 1:1 (Figure 4.7a) can be enlarged to $c_2 = 2.24 \pm 0.05$ nm, $d_2 = 2.15 \pm 0.05$ nm and $\beta_2 = 81.0° \pm 2°$ at Pen:F_{16}CuPc ratio of 2:1 (Figure 4.7b), and further enlarged to $c_3 = 2.89 \pm 0.05$ nm, $d_3 = 2.88 \pm 0.05$ nm and $\beta_3 = 72.0° \pm 2°$ at higher Pen:F_{16}CuPc ratio of 4:1 (Figure 4.7c). From Figure 4.7c, we note that the dimensions of the pentacene doublet are comparable to that of the square F_{16}CuPc molecule. The geometrical similarity between a single F_{16}CuPc molecule and a pentacene doublet increases the rotational freedom of the pentacene doublet in binary molecular networks.

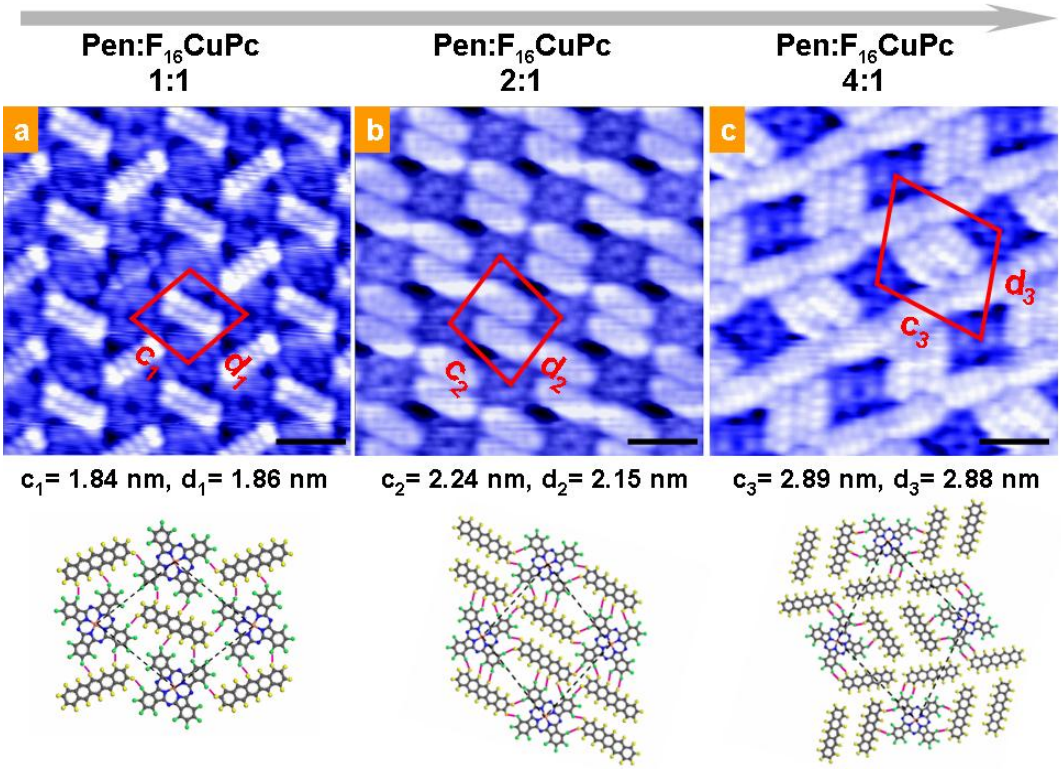

Figure 4.7 Molecularly-resolved 10 ×10 nm^2 STM images of the $F_{16}CuPc$ molecular dot arrays with tunable intermolecular distance controlled by the pentacene (Pen) coverage: (a) Pen:$F_{16}CuPc$=1:1 (V_{tip} = 2.5 V); (b) Pen:$F_{16}CuPc$ = 2:1 (V_{tip} = 3.0 V); and (c) Pen:$F_{16}CuPc$ = 4:1 (V_{tip} = 2.8 V). The short rod-like bright feature represents pentacene molecule. The scale bar in each STM image represents 2 nm. The DFT simulated molecular models are shown below of each STM image.

The in-plane orientation of the pentacene doublet can spontaneously switch between two different orientations in the Pen:$F_{16}CuPc$ networks at ratios of 4:1 and above, and therefore lack long-range ordering. Figures 4.8a-c display molecularly resolved STM images of Pen:$F_{16}CuPc$ networks with different $F_{16}CuPc$ coverages. In Figure 4.8a, a few $F_{16}CuPc$ molecules (indicated by the green rhombus) randomly insert into the pentacene monolayer on HOPG, and hence destroy the long-range ordering of the pentacene molecular arrays. There are two different pentacene doublets differing in their in-plane molecular

orientations, denoted as α_1 and β_1 in Figure 4.8a. The α_1 doublet has the same in-plane orientation as the pentacene monolayer; and the β_1 doublet undergoes an in-plane rotation with their long-molecular axis along the pentacene nanostripe packing direction (black dashed line). The β_1 doublets only exist next to the inserted F_{16}CuPc molecules. When the F_{16}CuPc coverage increases to about 0.3 ML, a short-range ordered network with Pen:F_{16}CuPc ratio of about 5:1 is formed, as highlighted by the black triangle in Figure 4.8b. There are four different pentacene doublets denoted as α_1, α_2, β_1 and β_2. As shown in the schematic drawing of Figure 4.8d, the pentacene doublets α_1 and α_2, β_1 and β_2 possess mirror symmetry, while α_1 and β_2, α_2 and β_1 can transform to each other by a rotation of 60 °. Figure 4.8c displays the supramolecular packing structure of Pen:F_{16}CuPc network at 4:1 ratio (the same as Figure 4.7c). The network is comprosed of F_{16}CuPc monomers surrounded by pentacene-singlet (yellow arrows) and pentacene-doublets (only α_2, β_1 and β_2 orientation here). The statistical number of α_2 doublets equals that of β_2 doublets, and the number of β_1 doublets is the greatest. The distribution of α_2 doublets and β_2 doublets is disordered and no long-range ordering can be observed in the Figure 4.8b and c. This suggests that the formation energies of the α_2 and β_2 doublets are similar.

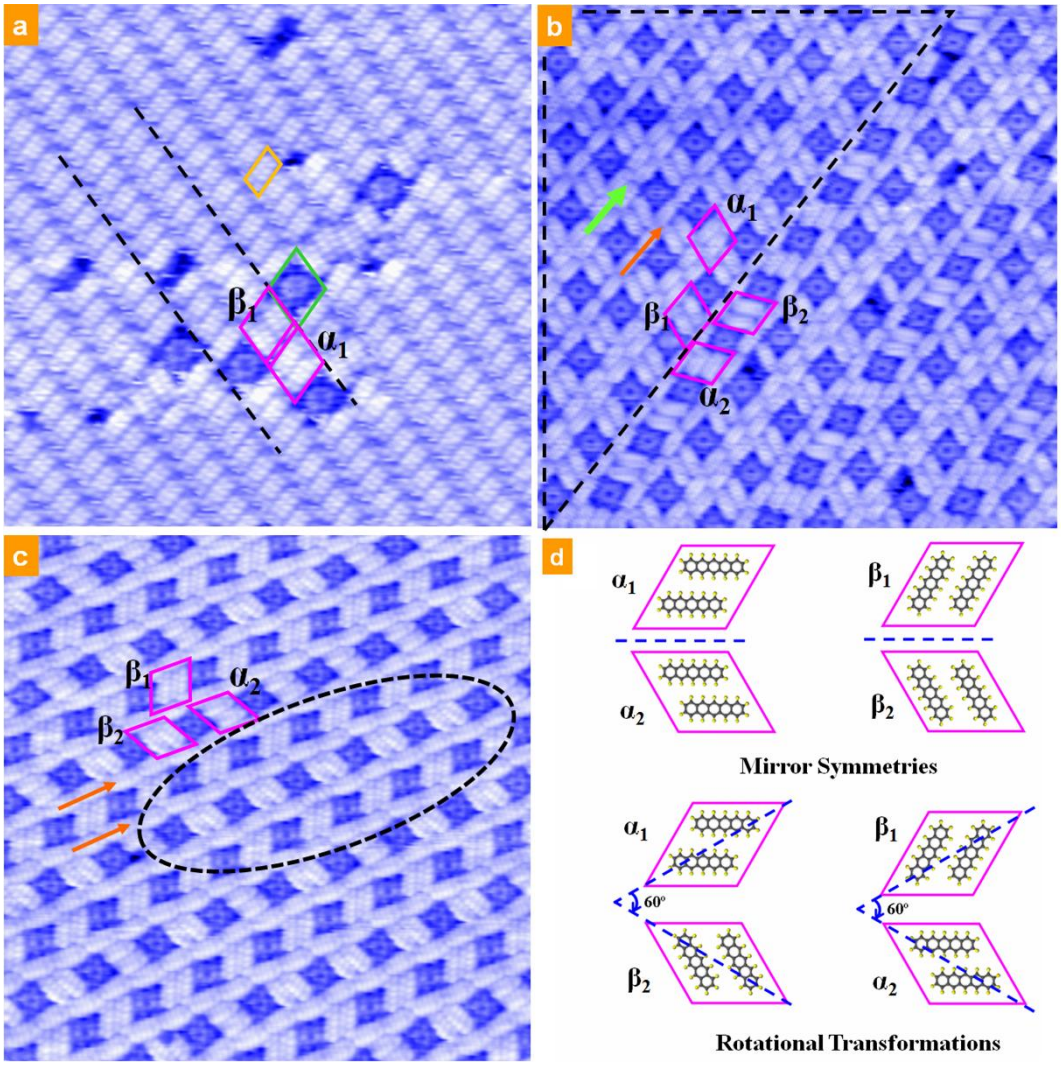

Figure 4.8 STM images of Pen:F_{16}CuPc networks at ratios of 4:1 and above. (a) Sparse F_{16}CuPc molecules are randomly embedded into the pentacene monolayer (20×20 nm^2, V_{tip} = 2.5 V). (b) The Pen:F_{16}CuPc network with a ratio of around 5:1. The black dotted triangle highlights the short-range ordered phase. Four pentacene doublets with different in-plane molecular orientations are denoted as α_1, α_2, β_1 and β_2, respectively (30×30 nm^2, V_{tip} = 2.6V). (c) The Pen:F_{16}CuPc network at a ratio of 4:1 with short-range order (30×30nm^2, V_{tip}=2.7V). (d) Schematic drawing demonstrates the relationship between the four different pentacene doublets, including mirror symmetries and rotational transformations.

4.3.4 DIP:F_{16}CuPc binary networks

The tunability of self-assembled molecular nanostructures on HOPG is further demonstrated by the third binary system of F_{16}CuPc with DIP. Since DIP is an

elliptical molecule with different dimensions to 6P and pentacene (Figure 4.5), the intermixing of F_{16}CuPc with DIP results in F_{16}CuPc dot arrays with different intermolecular separations and arrangements. As shown in Figure 4.9, the bright leaf-like feature represents a single DIP molecule. The structure of this binary supramolecular network, or the intermolecular distance of the F_{16}CuPc dot arrays, can be effectively adjusted by controlling the DIP:F_{16}CuPc ratio. The cell (denoted the separation of F_{16}CuPc dimmers) dimensions vary from e_1 = 1.75 ± 0.05 nm, f_1 = 2.35 ± 0.05 nm and γ_1 = 82.0 ° ± 2 ° at the DIP:F_{16}CuPc ratio of 1:2 (Figure 4.9a), e_2 = 1.91 ± 0.05 nm, f_2 = 1.91 ± 0.05 nm and γ_2 = 77.0 ° ± 2 ° at the ratio of 1:1 (Figure 4.9b), and e_3 = 2.46 ± 0.05 nm, f_3 = 2.44 ± 0.05 nm and γ_3 = 72.0 ° ± 2 ° at the ratio of 2:1 (Figure 4.9c). In Figure 4.9c, each F_{16}CuPc molecule is surrounded by 4 DIP molecules, which maximizes the number of the C-F···H-C intermolecular hydrogen bonds, giving good structural stability of this binary molecular network. Our simulated molecular models, shown below each STM image, suggest that the DIP:F_{16}CuPc binary molecular system has ten possible hydrogen bonds in the primitive unit cell when the intermixing ratio reaches 2:1 (listed in Table 1). Similar DIP and F_{16}CuPc binary networks combined through multiple intermolecular C-F···H-C bonding have also been reported on Au(111) and Cu(111) surfaces.[62]

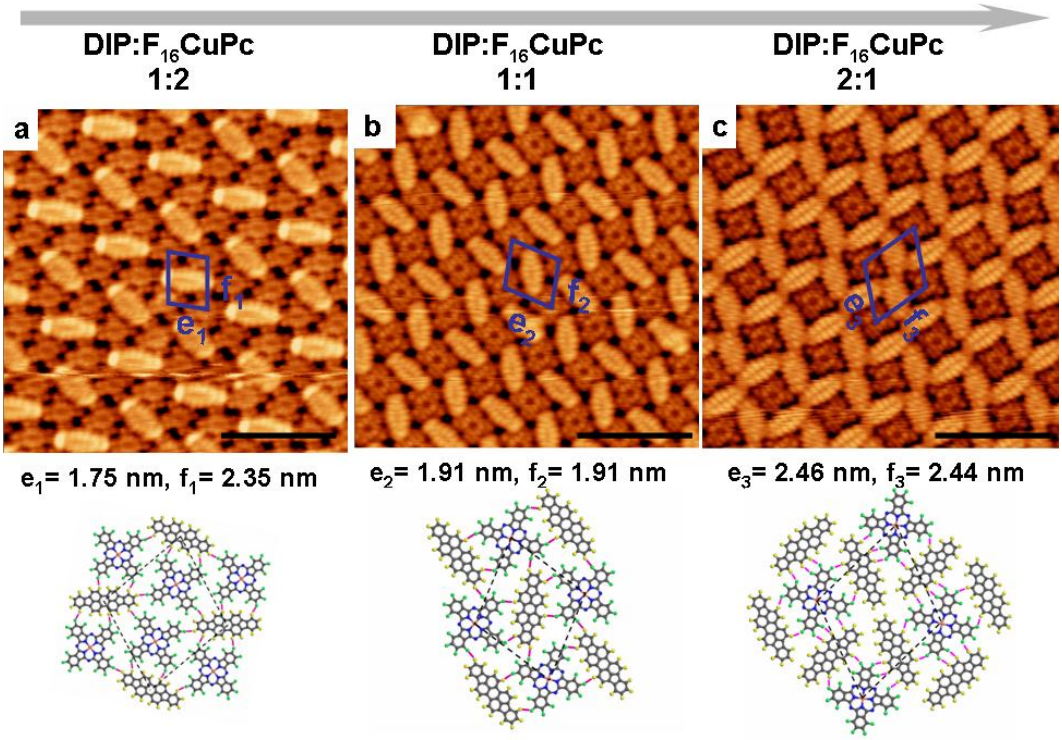

Figure 4.9 Molecularly-resolved 15 ×15 nm^2 STM images (top) and DFT simulated molecular models (below) of the F_{16}CuPc molecular dot arrays with tunable intermolecular distance controlled by the DIP coverage: (a) DIP:F_{16}CuPc=1:2 (V_{tip} = 2.8 V); (b) DIP:F_{16}CuPc = 1:1 (V_{tip} = 2.0 V); and (c) DIP:F_{16}CuPc = 2:1 (V_{tip} = 2.0 V). The leaf like bright feature represents DIP molecule. The scale bar in each STM image represents 5 nm.

4.3.5 Theoretical simulations based on density functional theory

To better understand the structural stability of these binary systems, DFT calculations were performed to evaluate the total intermolecular binding energy (E_{bind}) of each observed network. It is found that the molecule/graphite interfaces are dominated by π-π interactions, which constrain the molecules to lie flat with their conjugated π-plane parallel to the surface. The smooth potential energy surface of graphite does not induce any interlocking of adsorbed molecules with the substrate lattice. The 2D arrangements of the molecular networks are therefore mainly determined by lateral intermolecular interactions. In our DFT calculations, the energies of intermolecular interactions between every two neighboring

molecules are calculated to construct the total binding energy of each pattern. Although STM images have supplied very clear symmetries and packing structures, it is still necessary to evaluate the exact intermolecular distances for our DFT computational models. We first optimize the intermolecular C–H···F–C distances from the optimization conformations of hexafluorobenzene (C_6F_6) and benzene (C_6H_6) dimers on HOPG slabs, as shown in Figure 4.10. Consequently, we construct supramolecular packing structures on HOPG slabs based on the optimized intermolecular F···H (~2.5Å) and F···F (~2.7Å) distances as well as the structural symmetry observed from the STM images. The constructed molecular models agree well with our experimental results with deviations of less than 5%, as shown in the STM images in Figures 4.6, 4.7 and 4.9. All the calculations are on B3LYP[56, 57]/6-31G(d,p) level with the Gaussian03 package.[58]

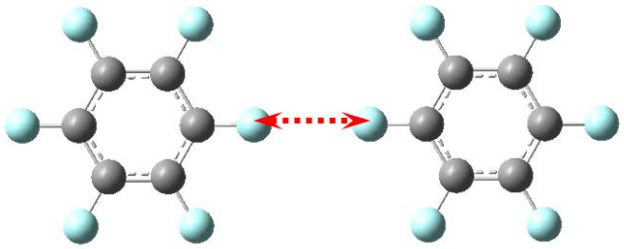

Figure 4.10 The optimized distances of C_6H_6-C_6F_6 and C_6F_6-C_6F_6 dimers on HOPG are obtained from DFT calculations, where the blue peripheral atoms represent F atoms and/or H atoms.

As shown in Table 4.1, we divide the formation energy E_{bind} into three parts, binding energies originating from F_{16}CuPc-F_{16}CuPc ($E_{F16\text{-}F16}$), X-X ($E_{X\text{-}X}$) and

F_{16}CuPc-X (E_{F16-X}) intermolecular interactions (X represents 6P, pentacene or DIP). It is obvious that the E_{bind} for each network is dominated by the F_{16}CuPc-X interactions (E_{F16-X}), confirming that the stability of these F_{16}CuPc dot arrays is greatly enhanced by intermolecular C-F···H-C bonding. In each primitive unit cell (denoted in the simulated molecular model below each STM image), the number of the possible C-F···H-C intermolecular hydrogen bonds with maximum length of 2.6 Å is also given in Table 4.1. Hence, the DFT calculations support our hypothesis that the formation of multiple intermolecular hydrogen bonds stabilizes these binary molecular networks.

6P:F_{16}	**$E_{F16-F16}$**	**E_{6P-6P}**	**E_{F16-6P}**	**E_{bind}**	**No. of H-bonds(<2.6Å)**
1:2	-0.73	-	-14.78	-15.51	8
1:1	-1.17	2.10	-18.70	-17.77	12
3:1	-	6.29	-13.84	-7.55	6
Pen:F_{16}	**$E_{F16-F16}$**	**$E_{Pen-Pen}$**	**$E_{F16-Pen}$**	**E_{bind}**	**No. of H-bonds(<2.6Å)**
1:1	-	-	-12.12	-12.12	6
2:1	-	0.65	-19.48	-18.83	12
4:1	-	2.97	-13.92	-10.95	8
DIP:F_{16}	**$E_{F16-F16}$**	**$E_{DIP-DIP}$**	**$E_{F16-DIP}$**	**E_{bind}**	**No. of H-bonds(<2.6Å)**
1:2	0.25	-	-13.74	-13.49	8
1:1	-	-	-13.86	-13.86	6
2:1	-	0.64	-19.26	-18.62	10

Table 4.1 Energy profile of the binary molecular networks on HOPG surface. E_{A-B} presents the intermolecular binding energy of the neighboring A and B molecules, where A and B represent F_{16}CuPc, Pen, 6P or DIP molecules respectively and independently. E_{bind} is the total intermolecular binding energy of each primitive cell as indicated in the simulated supramolecular packing structures. All the energies are counted in **[kcal mol^{-1}]**.

4.5 Summary

We have presented a novel bottom-up approach to construct tunable and robust 2D binary molecular nanostructures on inert graphite substrates. The self-assembly processes of the CuPc/F_{16}CuPc binary molecular system on HOPG is a model system for the study of selective and directional hydrogen bonding in molecular self-assembly on surfaces. Using *in-situ* LT-STM imaging, we find that the in-plane molecular orientation of individual CuPc or F_{16}CuPc molecule is very sensitive to the local molecular environment: at low CuPc coverage, the randomly inserted CuPc molecules in F_{16}CuPc monolayer matrix adopts the α- or β- in-plane orientations of the host matrix; as the CuPc coverage increases to 50%, CuPc and F_{16}CuPc transform to the α-phase to form a highly ordered chessboard-like pattern. This chessboard-like pattern spontaneously forms at the second CuPc/F_{16}CuPc layer. By MD simulations, we confirmed that the CuPc/F_{16}CuPc supramolecular arrangement (overall periodicity and molecular orientation) is stabilized by the intermolecular hydrogen bonding between neighboring CuPc and F_{16}CuPc.This detailed understanding of how the local molecular environment (substrate and neighboring molecules) determines the supramolecular arrangement enables us to design molecular nanostructures with desired functionalities.

The supramolecular packing structures can be controlled by careful selection of molecular building blocks with appropriate geometry (size and shape) and molecular ratios. As demonstrated in section 4.3, various 2D molecular networks have been fabricated in the binary molecular systems of F_{16}CuPc with 6P,

pentacene and DIP respectively, whose structural stability is sustained through the formation of multiple intermolecular C-F···H-C hydrogen bonds between the electronegative peripheral F atoms of F_{16}CuPc and the electropositive peripheral H atoms of 6P, pentacene or DIP. Our results also suggest that the component molecules have the freedom to assemble into their energy minima configurations on the graphite surfaces. The DFT calculations also confirmed that the intermolecular hydrogen bonding drives the formation of these molecular nanostructure arrays. Such molecular nanostructures with high degree of tunability have potential applications in molecular sensors and nanodevices. In particular, the versatility of the metal phthalocyanines facilitates the modification of the central metal atoms to feature desired functionalities, such as electronic spins for the construction of molecular spintronic devices.

References:

[1] R. Madueno, M. T. Raisanen, C. Silien, M. Buck, *Nature* **454**, 618-621(2008).

[2] S. De Feyter, F. De Schryver, *Top. Curr. Chem.* **258**, 205-255 (2005).

[3] L. Piot, D. Bonifazi, P. Samori, *Adv. Funct. Mater.* **17**, 3689-3693 (2007).

[4] Y. C. Ye, W. Sun, Y. F. Wang, X. Shao, X. G. Xu, F. Cheng, J. L. Li, K. Wu, *J. Phys. Chem. C.* **111**, 10138-10141 (2007).

[5] L. Sanchez, R. Otero, J. M. Gallego, R. Miranda, N. Martin, *Chem. Rev.* **109**, 2081-2091 (2009).

[6] J. A. Theobald, N. S. Oxtoby, M. A. Phillips, N. R. Champness, P. H. Beton, *Nature* **424**, 1029-1031 (2003).

[7] J. V. Barth, G. Constantini, K. Kern, *Nature* **437**, 671-679 (2005).

[8] J. V. Barth, *Annu. Rev. Phys. Chem. 58*, 375-407 (2007).

[9] S.-S. Li, B. H. Northrop, Q. H. Yuan, L. J. Wan, P. J. Stang, *Acc. Chem. Res.* **42**, 249-259 (2009); L. J. Wan, *Acc. Chem. Res.* **39**, 334-342 (2006).

[10] F. Cicoira, C. Santato, F. Rosei, *Top. Curr. Chem.* **285**, 203-267 (2008).

[11] F. Rosei, *J. Phys. Condens. Matter.* **16**, S1373-S1436 (2004).

[12] S. Stepanow, N. Lin, J. V. Barth, K. Kern, *Chem. Commun*. 2153-2155 (2006).

[13] H. L. Zhang, W. Chen, H. Huang, L. Chen, A. T. S. Wee, *J. Am. Chem. Soc.* **130**, 2720-2721 (2008).

[14] H. L. Zhang, W. Chen, L. Chen, H. Huang, J. Yuhara, A. T. S. Wee, *Small* **3**, 2015-2018 (2007).

[15] W. Chen, H. L. Zhang, H. Huang, L. Chen, A. T. S. Wee, *Appl. Phys. Lett*. **92,** 193301 (2008).

[16] M. Corso, W. Auwärter, M. Muntwiler, A. Tamai, T. Greber, J. Osterwalder, *Science* **303**, 217-220 (2004).

[17] J. Weckesser, A. De Vita, J. V. Barth, C. Cai, K. Kern, *Phys. Rev. Lett.* **87**, 096101 (2001).

[18] J. V. Barth, J. Weckesser, C. Z. Cai, P. Günter, L. Bürgi, O. Jeandupeux, K. Kern, *Angew. Chem, Int. Ed.* **39**, 1230-1234 (2000).

[19] M. Stohr, M. Wahl, H. Spillmann, L. H. Gade, T. A. Jung, *Small* **3**, 1336-1340 (2007).

[20] S. Stepanow, M. A. Lingenfelder, A. Dmitriev, H. Spillmann, E. Delvigne, N. Lin, X. Deng, C. Cai, J. V. Barth, K. Kern, *Nature Mater.* **3**, 229-233 (2004); M. A. Lingenfelder, H. Spillmann, A. Dmitriev, S. Stepanow, N. Lin, J. V. Barth, K. Kern, *Chem. Eur. J.* **10**, 1913-1919 (2004).

[21] N. Lin, S. Stepanow, F. Vidal, J. V. Barth, K. Kern, *Chem. Commun*. 1681-1683 (2005); N. Lin, A. Langner, S. L. Tait, R. Chandrasekar, M. Ruben, K. Kern, *Chem. Commun.* 4860-4862 (2007); A. Langner, S. L. Tait, N. Lin, R. Chandrasekar, M. Ruben, K. Kern, *Angew. Chem. Int. Ed*. **47**, 8835-8838 (2008); A. Langner, S. L. Tait, N. Lin, R. Chandrasekar, M. Ruben, K. Kern, *Proc. Natl. Acad. Sci.* **104**, 17927-17930 (2007).

[22] U. Schlickum, R. Decker, F. Klappenberger, G. Zoppellaro, S. Klyatskaya, M. Ruben, I. Silanes, A. Arnau, K. Kern, H. Brune, J. V. Barth, *Nano Lett.* **7**, 3813-3817 (2007).

[23] R. Madueno, M. T. Raisanen, C. Silien, M. Buck, *Nature* **454**, 618-621 (2008).

[24] J. C. Swarbrick, B. L. Rogers, N. R. Champness, P. H. Beton, *J. Phys. Chem. B* **110**, 6110-6114 (2006); J. Ma, B. L. Rogers, M. J. Humphry, D. J. Ring, G. Goretzki, N. R. Champness, P. H. Beton, *J. Phys. Chem. B* **110**, 12207-12210 (2006); P. A. Staniec, L. M. A. Perdigao, A. Saywell, N. R. Champness, P. H. Beton, *ChemPhysChem* **8**, 2177-2181 (2007); P. A. Staniec, L. M. A. Perdigao, B. L. Rogers, N. R. Champness, P. H. Beton, *J. Phys. Chem. C* **111**, 886-893 (2007).

[25] S. B. Lei, K. Tahara, X. L. Feng, S. Furukawa, F. C. De Schryver, K. Müllen, Y. Tobe, S. De Feyter, *J. Am. Chem. Soc.* **130**, 7119-7129 (2008).

[26] G. Pawin, K. L. Wong, K. Y. Kwon, L. Bartels, *Science* **313**, 961-962 (2006).

[27] H. Spillmann, A. Kiebele, M. Stöhr, T. A. Jung, D. Bonifazi, F. Cheng, F. Diederich, *Adv. Mater.* **18**, 275-279 (2006).

[28] W. D. Xiao, X. L. Feng, P. Ruffieux, O. Groning, K. Müllen, R. Fasel, *J. Am. Chem. Soc.* **130**, 8910-8912 (2008).

[29] R. Otero, M. Schöck, L. M. Molina, E. Lægsgaard, I. Stensgaard, B. Hammer, F. Besenbacher, *Angew. Chem. Int. Ed.* **44**, 2270-2275 (2004); R. Otero, M. Lukas, R. E. A. Kelly, W. Xu, E. Lægsgaard, I. Stensgaard, L. N. Kantorovich, F. Besenbacher, *Science* **319**, 312-315 (2008).

[30] A. Llanes-Pallas, M. Matena, T. Jung, M. Prato, M. Stohr, D. Bonifazi, *Angew. Chem. Int. Ed.* **47**, 7726-7730 (2008).

[31] T. Yokoyama, S. Yokoyama, T. Kamikado, Y. Okuno, S. Mashiko, *Nature* **413**, 619-621 (2001).

[32] L. M. A. Perdigao, N. R. Champness, P. H. Beton, *Chem. Commun.*, 538–540 (2006).

[33] D. F. Perepichka, F. Rosei, *Science* **323**, 216-217 (2009).

[34] L. Grill, M. Dyer, L. Lafferentz, M. Persson, M. V. Peters, S. Hecht, *Nature Nanotech.* **2**, 687-691 (2007).

[35] M. Treier, N. V. Richardson, R. Fasel, *J. Am. Chem. Soc.* **130**, 14054-14055 (2008).

[36] A. Gourdon, *Angew. Chem., Int. Ed.* **47**, 6950-6953 (2008).

[37] W. Chen, H. Li, H. Huang, Y. X. Fu, H. L. Zhang, J. Ma, A. T. S. Wee, *J. Am. Chem. Soc.* **130**, 12285-12289 (2008).

[38] L. Kampschulte, T. L. Werblowsky, R. S. K. Kishore, M. Schmittel, W. M. Heckl, M. Lackinger, *J. Am. Chem. Soc.* **130**, 8502-8507 (2008).

[39] S. B. Lei, M. Surin, K. Tahara, J. Adisoejoso, R. Lazzaroni, Y. Tobe, S. De Feyter, *Nano Lett.* **8**, 2541-2546 (2008).

[40] M. E. Canas-Ventura, W. D. Xiao, D. Wasserfallen, K. Müllen, H. Brune, J. V. Barth, R. Fasel, *Angew. Chem. Int. Ed.* **46**, 1814-1818 (2007).

[41] F. Silly, A. Q. Shaw, M. R. Castell, G. A. D. Briggs, *Chem. Commun*. 1907-1909 (2008).

[42] K. W. Hipps, L. Scudiero, D. E. Barlow, M. P. Cooke, *J. Am. Chem. Soc.* **124**, 2126-2127 (2002); L. Scudiero, K. W. Hipps, D. E. Barlow, *J. Phys. Chem. B* **107**, 2903-2909 (2003).

[43] K. Suto, S. Yoshimoto, K. Itaya, *J. Am. Chem. Soc.* **125**, 14976-14977 (2003); S. Yoshimoto, A. Tada, K. Suto, S.-L. Yau, K. Itaya, *Langmuir* **20**, 3159-3165 (2004); K. Suto, S. Yoshimoto, K. Itaya, *Langmuir* **22**, 10766-10776 (2006); S. Yoshimoto, Y. Honda, O. Ito, K. Itaya, *J. Am. Chem. Soc.* **130**, 1085-1092 (2008).

[44] U. K. Weber, V. M. Burlakov, L. M. A. Perdigao, R. H. J. Fawcett, P. H. Beton, N. R. Champness, J. H. Jefferson, G. A. D. Briggs, D. G. Pettifor, *Phys. Rev. Lett.* **100**, 156101 (2008).

[45] V. Oison, M. Koudia, M. Abel, L. Porte, *Phys. Rev. B* **75**, 035428 (2007).

[46] S. Lukas, G. Witte, Ch. Wöll, *Phys. Rev. Lett*. **88**, 028301 (2002).

[47] F. Ortmann, W. G. Schmidt, F. Bechstedt, *Phys. Rev. Lett.* **95**, 186101 (2005).

[48] D. G. de Oteyza, T. N. Krauss, E. Barrena, S. Sellner, H. Dosch, J. O. Osso, *Appl. Phy. Lett.* **90**, 243104 (2007).

[49] Y. L. Huang, W. Chen, S. Chen, A. T. S. Wee, *Appl. Phys. A* **95**, 107-111 (2009).

[50] W. Chen, H. Huang, S. Chen, L. Chen, H. L. Zhang, X. Y. Gao, A. T. S. Wee,

Appl. Phys. Lett. **91**, 114102 (2007).

[51] M. Abel, V. Oison, M. Koudia, C. Maurel, C. Katan, L. Porte, *ChemPhysChem* **7**, 82–85 (2006); M. Koudia, M. Abel, C. Maurel, A. Bliek, D. Catalin, M. Mossoyan, J. –C. Mossoyan, L. Porte, *J. Phys. Chem. B* **110**, 10058-10062 (2006).

[52] J. Wang, H. Wang, X. Yan, H. Huang, D. H. Yan, *Appl. Phys. Lett.* **87**, 093507 (2005); J. Wang, H. Wang, X. Yan, H. Huang, D. H. Yan, *Chem. Phys. Lett.* **407**, 87–90 (2005); K. M. Lau, J. X. Tang, H. Y. Sun, C. S. Lee, S. T. Lee, D. H. Yan, *Appl. Phys. Lett.* **88**, 173513 (2006); S. L. Lai, M. Y. Chan, M. K. Fung, C. S. Lee, S. T. Lee, *J. Appl. Phys.* **101**, 014509 (2007).

[53] W. Chen, S. Chen, H. Huang, D. C. Qi, X. Y. Gao, A. T. S. Wee, *Appl. Phys. Lett.* **92**, 063308 (2008).

[54] *Materials studio*, version 4.0, Accelrys Inc., San Diego (2006).

[55] R. S. Mulliken, *J. Chem. Phys*. **23**, 1833-1840 (1955).

[56] A. D. Becke, *J. Chem. Phys.* **98**, 5648-5652 (1993).

[57] C. Lee, W. Yang, R. G. Parr, *Phys. Rev. B* **37**, 785-789 (1988).

[58] M. J. Frisch, G. W. Trucks, H. B. Schlegel, G. E. Scuseria, M. A. Robb, J. R. Cheeseman, J. A. Montgomery, Jr., T. Vreven, K. N. Kudin, J. C. Burant, J. M. Millam, S. S. Iyengar, J. Tomasi, V. Barone, B. Mennucci, M. Cossi, G. Scalmani, N. Rega, G. A. Petersson, H. Nakatsuji, M. Hada, M. Ehara, K. Toyota, R. Fukuda, J. Hasegawa, M. Ishida, T. Nakajima, Y. Honda, O. Kitao, H. Nakai, M. Klene, X. Li, J. E. Knox, H. P. Hratchian, J. B. Cross, V. Bakken, C. Adamo, J. Jaramillo, R. Gomperts, R. E. Stratmann, O. Yazyev, A. J. Austin, R. Cammi, C. Pomelli, J. W. Ochterski, P. Y. Ayala, K. Morokuma, G. A. Voth, P. Salvador, J. J. Dannenberg, V. G. Zakrzewski, S. Dapprich, A. D. Daniels, M. C. Strain, O. Farkas, D. K. Malick, A. D. Rabuck, K. Raghavachari, J. B. Foresman, J. V. Ortiz, Q. Cui, A. G. Baboul, S. Clifford, J. Cioslowski, B. B. Stefanov, G. Liu, A. Liashenko, P. Piskorz, I. Komaromi, R. L. Martin, D. J. Fox, T. Keith, M. A. Al-Laham, C. Y. Peng, A. Nanayakkara, M. Challacombe, P. M. W. Gill, B. Johnson, W. Chen, M. W. Wong, C. Gonzalez, J. A. Pople, Gaussian 03, D.01; Gaussian, Inc: Wallingford, CT (2004).

[59] T. Steiner, *Angew. Chem. Int. Ed.* **41**, 48-76 (2002).

[60] W. Chen, H. Huang, A. T. S. Wee, *Chem. Commun*. 4276-4278 (2008).

[61] Y. L. Huang, W. Chen, S. Chen, A. T. S. Wee, *Appl. Phys. A* **95**, 107-111 (2009).

[62] E. Barrena, D. G. de Oteyza, H. Dosch, Y. Wakayama, *ChemPhysChem* **8**, 1915-1918 (2007).

Chapter 5

Molecular Trapping on 2D Binary Molecular Networks

5.1 Introduction

Selective coupling of functioning molecules at special adsorption sites on molecular surface nanotemplates represents a promising route to fabricate ordered organic nanostructure arrays with desired functionality over macroscopic areas for molecular nanodevice applications.[1-6] 2D nanoporous surface nanotemplates have been reported to provide geometrical voids to trap molecules.[1-6] Examples include the boron nitride nanomesh,[7,8] carbon nanomesh on silicon carbide,[9] supramolecular nanoporous surface templates constructed via metal-ligand,[10] multiple intermolecular hydrogen bonding[11-14] or other non-covalent intermolecular interactions.[15-17] Selective trapping of molecules can also be realized through molecular recognition on preferential binding sites on non-porous nanotemplates via specific non-covalent intermolecular interactions.[18-23] In particular, 2D supramolecular networks with bi- or multi- components can offer different molecular adsorption sites, and hence facilitate the growth of nanostructures with desired patterns. In this chapter, we demonstrate the growth of organic nanostructure arrays via preferential molecular adsorptions on non-porous planar binary molecular nanotemplates.

The construction of tunable and robust 2D binary molecular nanostructures with different molecular components and relative molecular ratios on graphite has been demonstrated in Chapter 4.[24] It is found that some of the rigid hydrogen-bonding networks can be used to accommodate incoming guest molecules on specific adsorption sites and facilitate the formation of regular patterns atop the underlying templates. In order to preserve the 2D arrangement of the underlying molecular networks as well as the pristine unique properties of the trapped functioning molecules during the assembly processes, stabilizing the trapped molecules by selective and non-chemical intermolecular interactions (such as intermolecular π-π interaction) is required. In the following sections, the assemblies of 2nd layer F_{16}CuPc molecules on the binary molecular networks of DIP:F_{16}CuPc and 6P:F_{16}CuPc on graphite are investigated. The 2nd layer F_{16}CuPc molecules exclusively adsorb atop the same type of molecule in the underlying binary molecular network mainly via intermolecular π-π interaction, resulting in the formations of F_{16}CuPc molecular dots or chain arrays.

5.2 2nd layer molecular dots atop the DIP:F_{16}CuPc binary network

5.2.1 The adsorption of 2nd layer F_{16}CuPc molecules at various coverages

The formation of DIP:F_{16}CuPc binary networks at different relative molecular ratios has been demonstrated in Chapter **4.3.4**. The template used here is the one with DIP:F_{16}CuPc molecular ratio of 2:1.[24] Figure 5.1a shows the molecularly resolved 30 × 30nm^2 STM image of the DIP:F_{16}CuPc network, where the four-

lobe pattern represents a F_{16}CuPc molecule and the bright leaf-like feature represents a single DIP molecule. Each F_{16}CuPc molecule is surrounded by 4 DIP molecules to maximize the intermolecular interactions (mainly C-F···H-C hydrogen bonding between the peripheral F atoms on F_{16}CuPc and H atoms on neighboring DIP), thereby ensuring good structural stability of this binary molecular network.[24, 25] The corresponding molecular model is shown in Figure 5.1c. The primitive cell indicated by a rhombus in Figure 5.1a reveals an intermolecular distance between the nearest-neighbor F_{16}CuPc molecules (from central Cu atom to Cu atom) of 2.68 ± 0.02 nm (experimental result), and a distance between the second nearest-neighbor F_{16}CuPc molecules (along the short diagonal direction) of 2.88 ± 0.02 nm. Further deposition of 0.14 ML F_{16}CuPc molecules (1 ML refers to a close-packed F_{16}CuPc monolayer with the molecular plane parallel to HOPG surface[26]) results in a decoration of individual molecules on this molecular template, as shown in Figure 5.1b. However, at this coverage, we cannot observe the formation of any long-range ordered molecular nanostructure in the 2nd layer F_{16}CuPc molecules. From the zoom-in 15×15 nm^2 image in Figure 5.1d, we find that each F_{16}CuPc molecule in the 2nd layer adsorbs precisely on top of the underlying F_{16}CuPc molecule. The 2nd layer molecule and its underlying F_{16}CuPc molecule have the same in-plane molecular orientation, and there is no visible lateral displacement between the 1st layer and 2nd layer molecules. As indicated by black and green arrows in Figure 5.1d, the 1st layer F_{16}CuPc molecules adopt two different in-plane molecular orientations with azimuth angles of $\alpha = 95° \pm 2°$ and $\beta = 85° \pm 2°$ respectively. Along the red dashed

line direction, the F_{16}CuPc molecules process the same in-plane molecular orientation. Correspondingly, the 2nd layer F_{16}CuPc molecules process the in-plane orientations determined by the underlying ones. The 2nd layer F_{16}CuPc adopting the flat-lying configuration (no out-plane orientation observed) agrees well with our previous observations of the bi-layer F_{16}CuPc on HOPG (Chapter **3**) and Ag(111).[27] The proposed stacking structure is demonstrated in the schematic image of Figure 5.1e, where the purple molecules represent the 1st layer F_{16}CuPc (underlying) and the orange ones represent the 2nd layer molecules.

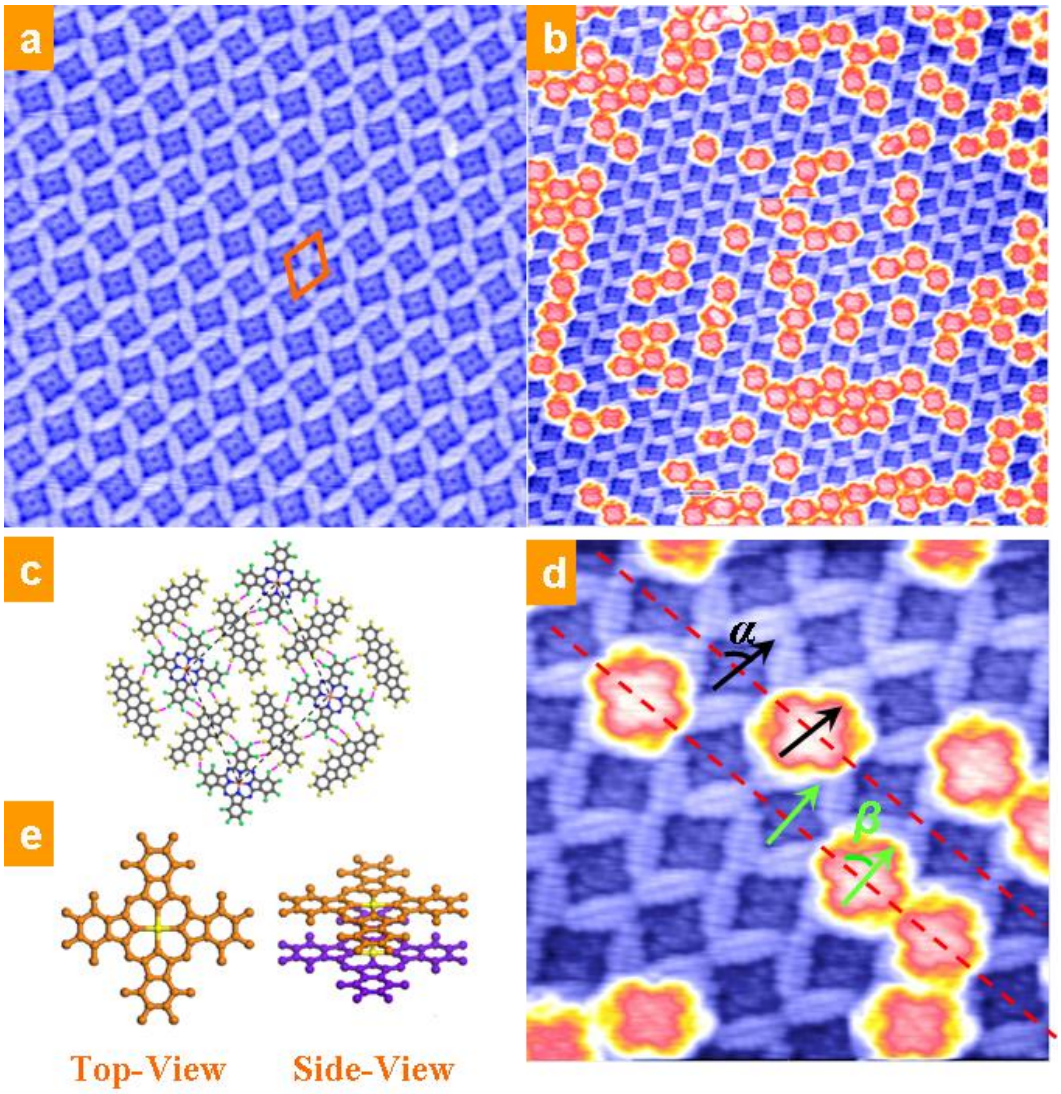

Figure 5.1 (a) 30 × 30nm^2 STM image (V_{tip} = 2.2 V) shows the DIP:F_{16}CuPc network at the ratio of 2:1, where each F_{16}CuPc molecule is surrounded by 4 DIP molecules, and (c) its corresponding simulated supramolecular structure. (b) A deposition of 0.14 ML F_{16}CuPc onto the network results in the random decoration of isolated F_{16}CuPc molecules on this network (50 × 50nm^2, V_{tip} = 1.9 V). (d) A zoom-in 15 × 15 nm^2 image of panel b reveals that the top F_{16}CuPc molecule adsorbs exactly on top of the underlying F_{16}CuPc molecular site in the binary molecular network (V_{tip} = 2.0 V). The schematic drawing of the packing structures is shown in panel (e) by both top-view and side-view.

To confirm the observed packing geometry, we further analyze the lateral line profiles taken along the 2nd layer molecular arrays as well as the underlying molecular template. In Figure 5.2a, the molecularly resolved STM image shows the DIP:F_{16}CuPc network decorated with ~0.05 ML F_{16}CuPc, where the dashed line 1 is taken along the 2nd layer molecular arrays and line 2 along the template. Figure 5.2c shows that the lines 1 and 2 have the same 2.88 nm periodicity. It also shows that the protrusions of the line 1 (corresponding to 2nd layer F_{16}CuPc) and the pits of the line 2 (1st layer F_{16}CuPc) are almost coaxial, as indicated by the purple dashed line in Figure 5.2c. Hence, the 2nd layer F_{16}CuPc molecules sit precisely atop the underlying ones with their central copper atoms aligned coaxially. This proposed stacking geometry differs with previously reported multilayer metal phthalocyanine thin films (such as F_{16}CuPc and CoPc), which usually adopt slipped or rotated stacking geometries to maximize interlayer π-π interactions.[26-28] The stacking structure of the 2nd layer F_{16}CuPc molecules precisely adsorbed upon the 1st layer ones is suggested to be confined by the underlying binary DIP:F_{16}CuPc network.

The preferential adsorption still survives when the occupation of the 1st layer F_{16}CuPc adsorption sites increases to ~50% (the coverage of the 2nd layer F_{16}CuPc

is increased to ~0.2 ML) as shown in Figure 5.2b. From large-scale STM images, no long-range ordered, closed-packing aggregation of the 2nd layer F_{16}CuPc molecules is observed. Correspondingly, as indicated by the quasi-hexagons in Figure 5.2b, the intermolecular distance between the nearest-neighbor 2nd layer molecules is around 2.68 nm, consistent with the underlying network. When the coverage of the 2nd layer F_{16}CuPc increases to ~0.4 ML (almost every 1st F_{16}CuPc adsorption site is occupied), a loose-packed layer is formed with the same F_{16}CuPc-F_{16}CuPc intermolecular distance as the underlying template (Figure 5.2d). The DIP:F_{16}CuPc network can therefore serve as an effective molecular nanotemplate to steer the formation of isolated F_{16}CuPc molecular dot arrays. The formation of such unique stacking geometry of the 2nd layer F_{16}CuPc is clearly due to geometrical confinement by the underlying DIP:F_{16}CuPc network.

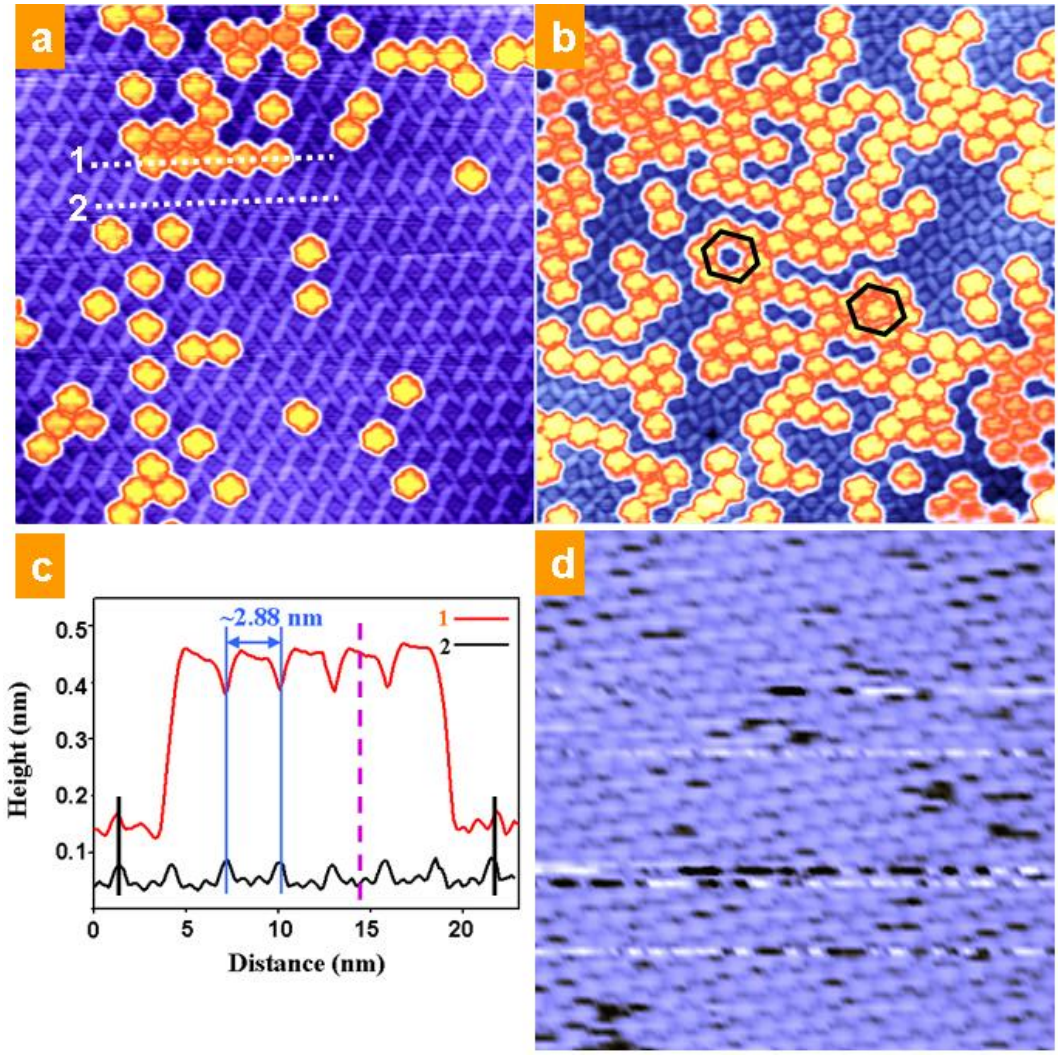

Figure 5.2 The DIP:F_{16}CuPc networks are decorated by different amounts of F_{16}CuPc: (a) ~ 0.05 ML F_{16}CuPc (50 × 50 nm^2, V_{tip} = 2.0 V), (b) ~ 0.2 ML F_{16}CuPc (50 × 50 nm^2, V_{tip} = 2.7 V), and (d) ~ 0.4 ML F_{16}CuPc (50 × 50 nm^2, V_{tip} = -2.5 V) (c) The line profiles corresponding to the dashed lines 1 and 2 in panel (a) reveal the same 2.88 nm periodicity of the 2nd layer molecular arrays and the underlying network. The short black lines show that these two lines have the same starting and ending points, while the dashed purple line shows that the centers of the 2nd layer and the 1st layer F_{16}CuPc molecules are precisely coaxial.

5.2.2 Statistics of the distribution of the 2nd layer F_{16}CuPc molecules

We next address the question of whether the F_{16}CuPc molecules in the second layer are randomly distributed or not. We analyzed the distribution of the 2nd layer molecules on the DIP:F_{16}CuPc template via a chi-square test, to test the

randomness hypothesis.[29, 30] The test method can be described as follows. Figure 5.3 shows a 50×50 nm^2 STM image of the DIP:F_{16}CuPc template decorated with 0.14 ML F_{16}CuPc (40% of the underlying F_{16}CuPc adsorption sites are occupied). We divided the 50×50 nm^2 area into 9 smaller squares and counted the population of the adsorbed molecules in each square cell. $\boldsymbol{A_{ij}}$ ($\boldsymbol{i}$, $\boldsymbol{j}$ = 1, 2, or 3) represents any square cell and $\boldsymbol{X_{ij}}$ represents the corresponding molecular population. We obtain the total molecular population $\boldsymbol{N}$ = 143 by summing up all the $\boldsymbol{X_{ij}}$ ($\sum_{i,j} X_{ij}$), and the expected value $\boldsymbol{E}$ = 15.9 of $\boldsymbol{A_{ij}}$ by dividing $\boldsymbol{N}$ with 9. The value of the test-statistic is

$$\chi^2 = \sum_{i,j} \frac{(X_{ij} - E)^2}{E} \ ,$$

Thus, we obtained χ^2 = 2.573 in this example. The probability ($\boldsymbol{P}$) of observing a test statistic in a chi-square distribution can be determined using standard statistical tables once we know the value of χ^2 and the degree of freedom $\boldsymbol{df}$ of the test. The $\boldsymbol{df}$ equals to $\boldsymbol{m}$ – 1, where $\boldsymbol{m}$ is number of unit cells we divided the image into. Hence, $\boldsymbol{df}$ = 8 ($\boldsymbol{m}$ = 3×3) in the example of Figure 5.3. Correspondingly, $\boldsymbol{P}$ (2.573, 8) is found to be 0.958, which means that we have no evidence to reject the null hypothesis that the distribution observed in Figure 5.3 is a random distribution.[29, 30]

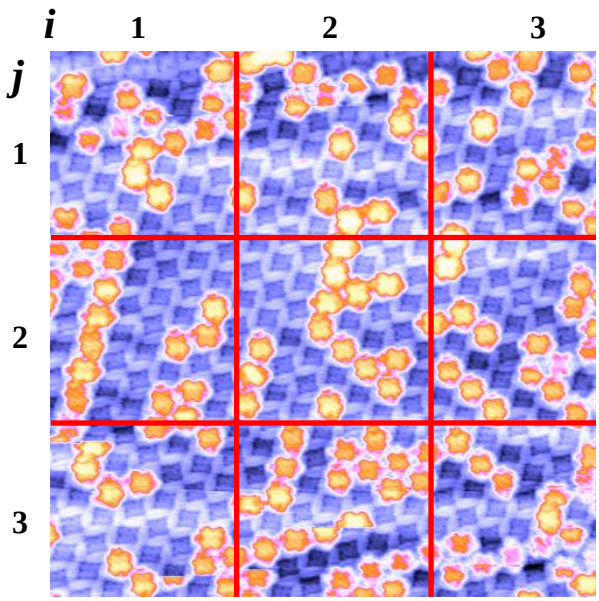

Figure 5.3 A 50×50 nm^2 STM image showing the DIP:F_{16}CuPc template decorated with 0.14 ML F_{16}CuPc is divided into 9 square cells.

The statistical results of 5 different images are shown in Table 5.1. We analyzed two 50×50 nm^2 STM images at low coverage (0.05 ML), a 50×50 nm^2 and a 100×100 nm^2 image at medium coverage (0.14 ML), and also a 75×75 nm^2 image at high coverage (0.2 ML). For each sample, we performed three different plots, namely 3×3, 4×4, and 5×5, where the corresponding ***df*** is 8, 15, and 24 respectively. As the expected value is required to be larger than 5 for the chi-square test, the sample 1 and 2 at low coverage cannot be further divided into 16 or 25 cells. A ***P***-value of 0.05 or less is usually regarded as statistically significant where we have evidence to reject the null hypothesis of a random distribution. Our chi-square test results are shown in Table 5.1. Only two ***P***-values at the low coverages are less than 0.05; the others are all larger than 0.5, and some of them

are very close to 1. This suggests that there may be evidence for clustering at low coverage (0.05 ML), but there is no evidence for long-range order at the higher coverages.

The random distribution of the 2nd layer F_{16}CuPc (especially at 0.14 ML and 0.2 ML) on the DIP:F_{16}CuPc template is understandable. Firstly, the intermolecular distance between the nearest-neighbor 2nd layer molecules is around 2.68 nm, much larger than the 1.55 nm periodicity of the closed packed F_{16}CuPc monolayer.[26] This suggests that there is no strong lateral intermolecular interaction between the 2nd layer molecules. Secondly, the underlying DIP:F_{16}CuPc network is preserved after the adsorption of 2nd layer F_{16}CuPc. Figure 5.4a and b demonstrate two 50 × 50 nm^2 STM images subsequently captured at V_{tip} = 2.3 V (0.14 ML coverage), where surface molecular diffusion is observed. **A1** and **A2** indicate a molecule diffusing from one site to the other; the green ellipse highlights the other example. Obviously, reconstruction of the underlying template, which could involve strong interfacial interactions between the 1st and 2nd layer molecules and further affect the arrangement of the 2nd layer molecules, does not occur in this system. The surface molecular diffusion also suggests a relatively weak interfacial interaction between the 2nd layer molecules with the underlying template.

Coverages	Sample	Degree of freedom			
		8 (3×3)	15 (4×4)	24 (5×5)	
Low coverage (0.05 ML)	$N_1 = 56$ (50×50 nm^2)	$\chi^2 = 23.71$ $P = 0.003$	-	-	significant
	$N_2 = 50$ (50×50 nm^2)	$\chi^2 = 18.04$ $P = 0.021$	-	-	
Medium coverage (0.14 ML)	$N_3 = 143$ (50×50 nm^2)	$\chi^2 = 2.573$ $P = 0.958$	$\chi^2 = 13.53$ $P = 0.561$	$\chi^2 = 8.923$ $P = 0.997$	non-significant
	$N_4 = 600$ (100×100 nm^2)	$\chi^2 = 5.310$ $P = 0.724$	$\chi^2 = 6.027$ $P = 0.979$	$\chi^2 = 14.00$ $P = 0.947$	
High coverage (0.2 ML)	$N_5 = 438$ (75×75 nm^2)	$\chi^2 = 2.587$ $P = 0.957$	$\chi^2 = 8.831$ $P = 0.886$	$\chi^2 = 16.68$ $P = 0.862$	

Table 5.1 The chi-square test of the 2nd layer molecular distribution.

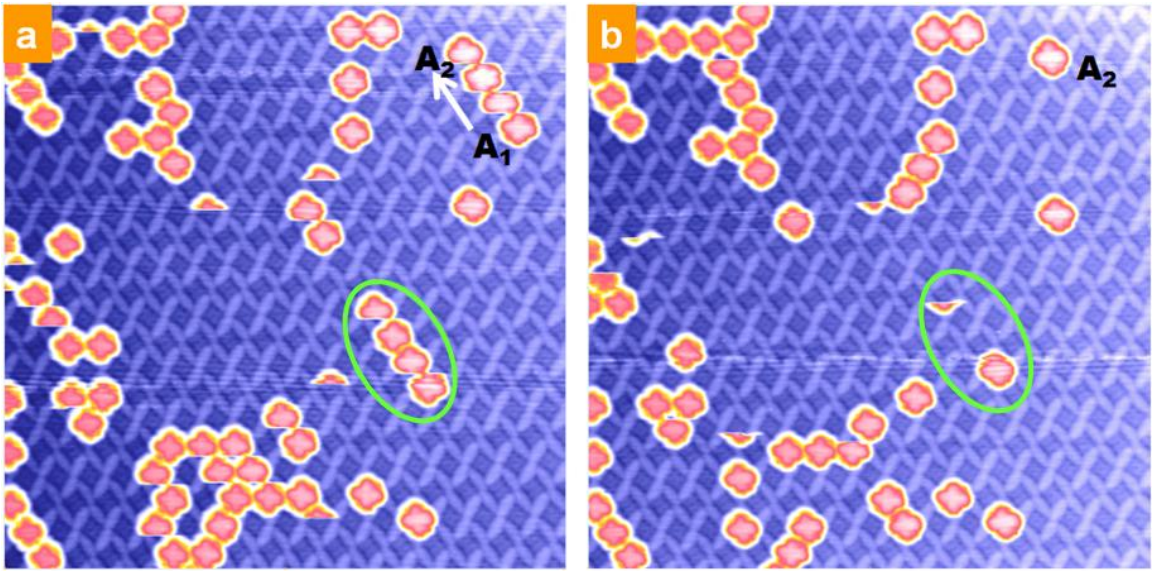

Figure 5.4 (a) and (b) 50 × 50 nm^2 STM images subsequently captured at V_{tip} = 2.3 V, I_{set} = 100pA at the same area. **A1** and **A2** indicate surface molecular diffusion from one site to the other, and the green ellipse highlights the other example. The underlying DIP: F_{16}CuPc template stays uniform during the molecular diffusion.

5.3 2nd layer molecular chains on 6P:F_{16}CuPc binary network

5.3.1 Flexibility of the 6P molecular stripes at different molecular coverages

It has been reported by our group and others that the packing structure of 6P monolayer on graphite is dynamic.[31-33] Figure 5.5a shows a representative molecularly resolved 15×15 nm^2 STM image of a well-ordered 6P monolayer on HOPG, in which each long rod-like feature represents a single 6P molecule. The length of the 6P molecule along its long-axis direction is 2.95 ± 0.02 nm, as highlighted in Figure 5.5a. The periodicity along the 6P nanostripe (highlighted by the dashed line) is 0.70 ± 0.02 nm, as revealed by the line profile in Figure 5.5e. As shown by the schematic drawing in Figure 5.5f, the proposed model of the 6P monolayer involves face-on 6P molecules packed in side-by-side. The face-on configuration refers to 6P molecule packing with their extended molecular π-planes parallel to the substrate. Such face-on 6P monolayer on HOPG is stabilized by dispersion interaction. At higher 6P coverage, a more compact 6P monolayer phase forms with periodic insertion of edge-on 6P molecules into the face-on 6P molecular matrix. The edge-on configuration refers to 6P molecules orientated with their phenyl rings perpendicular to the surface, and long molecular axis parallel to the surface, and the edge-on 6P molecules are displayed as brighter features in the STM image compared to the surrounding face-on 6P molecules as shown in Figure 5.5b–d. In Figure 5.5b, a deposition of 0.10 ML 6P on the face-on 6P monolayer on HOPG leads to the formation of 6P nanostripes with a large intermolecular spacing of 2.5 ± 0.02 nm along the 6P packing

direction (marked by the dashed line). The corresponding line profile is shown in Figure 5.5e, and the proposed model involves an alternating arrangement of one edge-on 6P molecule and three successive face-on 6P molecules as shown in Figure 5.5h. In Figure 5.5c and d, a more compact 6P nanostripe array is formed as a result of increasing the 6P coverage to 0.15 ML onto the face-on 6P monolayer. The periodicity along the 6P packing direction is 1.8 ± 0.02 nm as revealed by the line profile c in Figure 5.5e. Figure 5.5g shows the corresponding schematic model comprising a periodic placement of two face-on 6P molecule with one edge-on 6P molecule. The placement of the neighboring face-on and edge-on 6P molecules are stabilized by electrostatic forces between these two types of 6P molecules.[32, 33] This is reminiscent of the typical herringbone structure commonly observed in 6P single crystal solids.[34, 35] Such tunable periodicity of the alternating arrangement of the face-on and edge-on 6P molecules with variable numbers of inserted edge-on 6P molecules, has also been observed on Au(111) surface.[31]

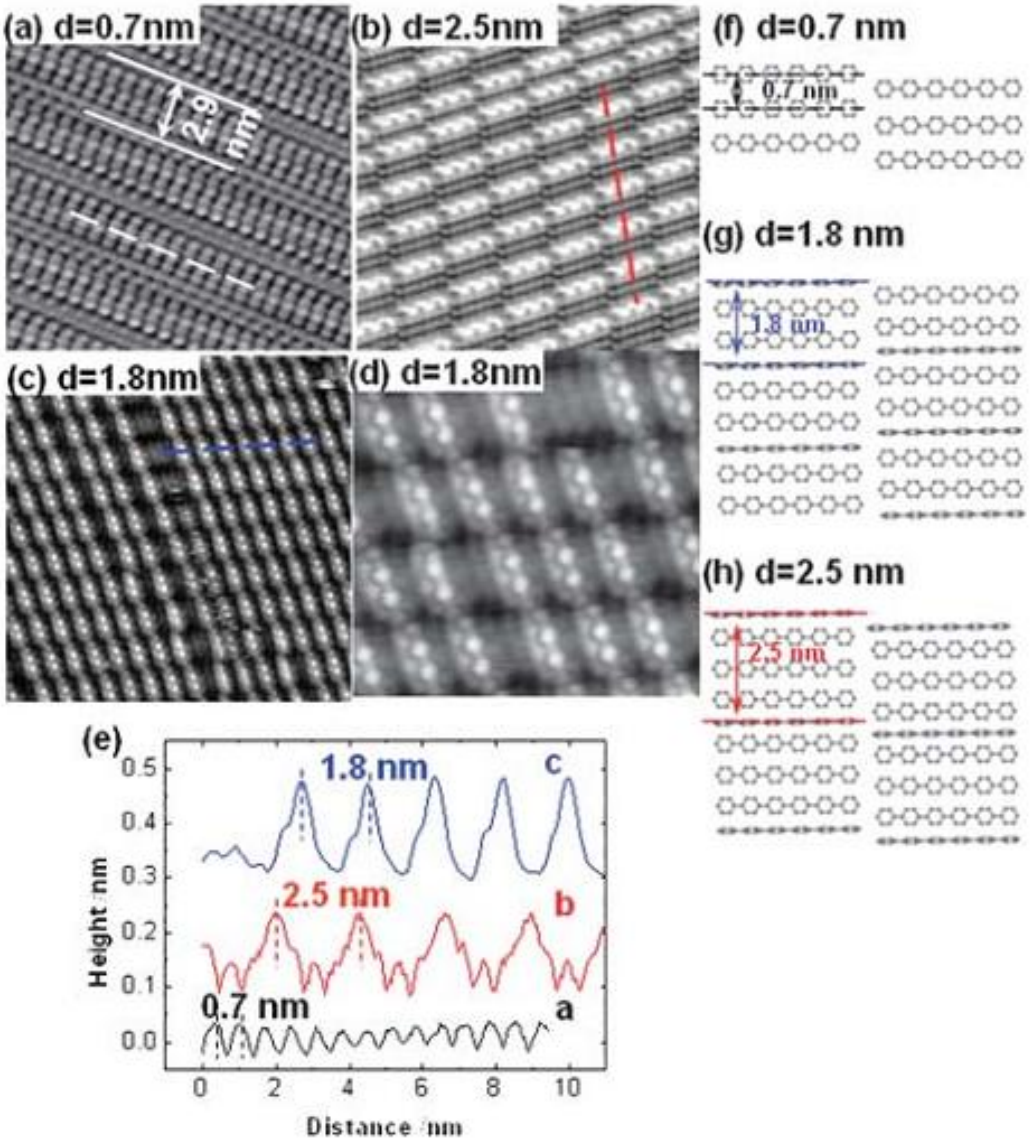

Figure 5.5 Coverage-dependent STM images of 6P on HOPG surface. (a)face-on 6P monolayer (15 × 15 nm^2, V_{tip} = -1.5 V); (b) face-on +edge-on 6P layer with 2.5 nm inter-stripe distance (20 × 20 nm^2, V_{tip} = 3.3 V); (c) face-on + edge-on 6P layer with 1.8 nm inter-stripe distance (30 × 30 nm^2, V_{tip} = -3.2 V), and (d) corresponding detailed 12 × 12 nm^2 image for panel (c). (e) Corresponding line profiles as indicated by the dashed line in panels (a), (b) and (c). Panels (f), (g) and (h): Corresponding schematic models for the supramolecular arrangement of 6P molecules on HOPG in panels (a), (b) and (c), respectively. (Figure adapted from Ref.31)

5.3.2 Tunability of the 6P:F_{16}CuPc binary network with insertion of edge-on 6P molecules

The tunability of the 6P:F_{16}CuPc binary network with variable 6P:F_{16}CuPc relative molecular ratio has been discussed in Chapter 4.3. Here, we present the

tunability of the binary network caused by the insertion of edge-on 6P molecules. Figure 5.6a shows a 30 × 30 nm^2 STM image of a 6P:F_{16}CuPc supramolecular network at the 6P:F_{16}CuPc molecular ratio of 3:1, with the unit cell comprising two F_{16}CuPc doublets interconnected by a 6P triplet through intermolecular C-F···H-C hydrogen bonding.[24] The proposed molecular packing structure is demonstrated in the left of Figure 5.6g. All the 6P and F_{16}CuPc molecules adopt the face-on configuration with their extending molecular π-planes parallel to the substrate. The intermolecular distance between the neighboring 6P molecules is 0.70 ±0.02 nm, as shown in Figure 5.6d. This intermolecular distance is consistent with the previously reported periodicity of 6P monolayer with pure face-on configuration on HOPG or other metal substrates.[31-33] It has been demonstrated that the packing structure of the 6P monolayer on graphite is very dynamic,[31-33] and increasing the 6P coverage leads to the insertion of edge-on 6P into the face-on 6P molecular array to form a more compact 6P phase. The periodicity of the alternating arrangement of the face-on and edge-on 6P molecules can be adjusted by the amount of the inserted edge-on 6P molecules as shown previously.[31] Such control can also be realized in our binary molecular system of F_{16}CuPc with 6P and therefore further increases the tunability of the binary molecular networks. As shown in Figures 5.6a to b, the random insertion of edge-on 6P molecules at higher 6P coverage causes structural rearrangement of the 6P:F_{16}CuPc network. In Figure 5.6b, the pink rod-like feature represents a single edge-on 6P molecule embedded into the face-on 6P molecular array. The formed F_{16}CuPc linear chain arrays are interconnected with the single 6P molecular stripes comprising

randomly positioned edge-on and face-on 6P molecules via the formation of multiple intermolecular C-F···H-C hydrogen bonding.

By controlling the 6P coverage, ordered 6P molecular stripes with periodic placement of a face-on 6P dimer and an edge-on 6P monomer can be formed. Such ordered 6P stripes allow the formation of long-range ordered alternating 6P:F_{16}CuPc linear molecular chain arrays as shown in Figure 5.6 c. Figure 5.6f displays the line profile taken along the edge-on + face-on 6P chain as marked by the dashed line in Figure 5.6c, revealing a 1.8 nm periodicity of the 6P molecular chains. The F_{16}CuPc chains also have the same periodicity. The proposed supramolecular packing structures of the face-on 6P molecular chain and the edge-on + face-on 6P chain with 1.8 nm periodicity are shown by the schematic drawings in Figure 5.6d and 5.6e respectively, the same as that shown in Figure 5.5 f and g. The corresponding supramolecular model of the 6P:F_{16}CuPc molecular chain array is shown in the right of Figure 5.6g. The formation of multiple intermolecular C-F···H-C hydrogen bonding between neighboring F_{16}CuPc and 6P chains ensures the structural stability of this molecular network.

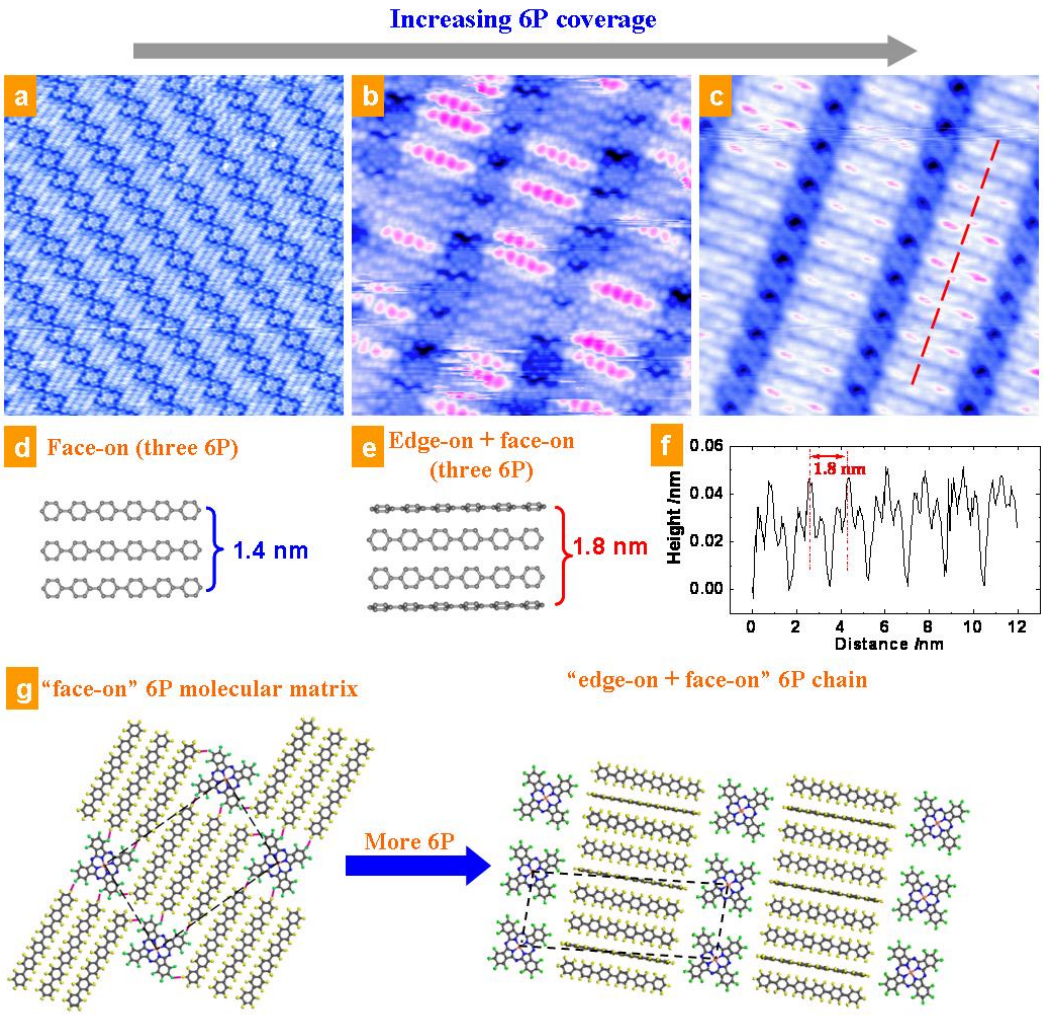

Figure 5.6 (a) 30 × 30nm^2 STM image showing the perfectly ordered oblique F_{16}CuPc molecular dot array comprising two F_{16}CuPc doublets interlinked by a 6P triplet with 6P:F_{16}CuPc = 3:1 (V_{tip} = 2.7 V). (b) the insertion (randomly) of the edge-on 6P molecules into face-on 6P molecules results in the transition to a F_{16}CuPc linear chain array (15 × 15 nm^2, V_{tip} = 2.5 V). (c) F_{16}CuPc linear chain array interconnected by an ordered edge-on + face-on 6P molecular wire can be obtained (15 × 15 nm^2, V_{tip} = 2.6 V). (d) and (e) display the schematic drawings of the molecular packing structures of the face-on 6P triplet and the edge-on + face-on 6P chain, respectively. (f) The line profile is taken along the edge-on + face-on 6P chain as marked by the dashed line in panel c, revealing a 1.8 nm periodicity. (g) Proposed corresponding supramolecular packing structure transition from panel (a) to panel (c).

5.3.3 Preferential adsorption of the 2nd layer F_{16}CuPc molecules

The rigid 6P:F_{16}CuPc linear chain array can serve as an effective surface nanotemplate to selectively accommodate additional F_{16}CuPc molecules to form

2^{nd} layer 1D molecular chain arrays, as shown in Figure 5.7a and its corresponding zoom-in STM image in Figure 5.7b. The inter-chain distance of the 2^{nd} layer F_{16}CuPc chain array is 4.65 ± 0.02 nm and the intermolecular distance along the F_{16}CuPc chain is 1.80 ± 0.02 nm, exactly matching that of the underlying 6P:F_{16}CuPc molecular nanotemplate. The ellipse in Figure 5.7b highlights an incomplete 2^{nd} layer F_{16}CuPc chain. This reveals the exclusive adsorption of the 2^{nd} layer F_{16}CuPc atop the underlying F_{16}CuPc molecules with a small lateral displacement (~ 0.50 nm) along the molecular chain direction. The in-plane molecular orientation of the top F_{16}CuPc is identical to that of the underlying one. At lower F_{16}CuPc coverage, there are more vacancies on the 2^{nd} layer, as shown in Figure 5.7c. Figure 5.7d displays the proposed molecular packing structure of the F_{16}CuPc bilayer stacking with a slipped geometry along the F_{16}CuPc molecular chain (denoted by the red arrow). A similar slipped stacking geometry, which maximizes the interlayer π-π interactions, has been previously observed for close packed 2^{nd} layer F_{16}CuPc films on Ag(111)[27] and HOPG,[26] and for the multilayer stacked CoPc thin film on Pb/Si(111).[28] Hence, the preferred adsorption of the 2^{nd} layer F_{16}CuPc atop the 1^{st} layer ones is mainly driven by interlayer F_{16}CuPc-F_{16}CuPc π-π interactions.

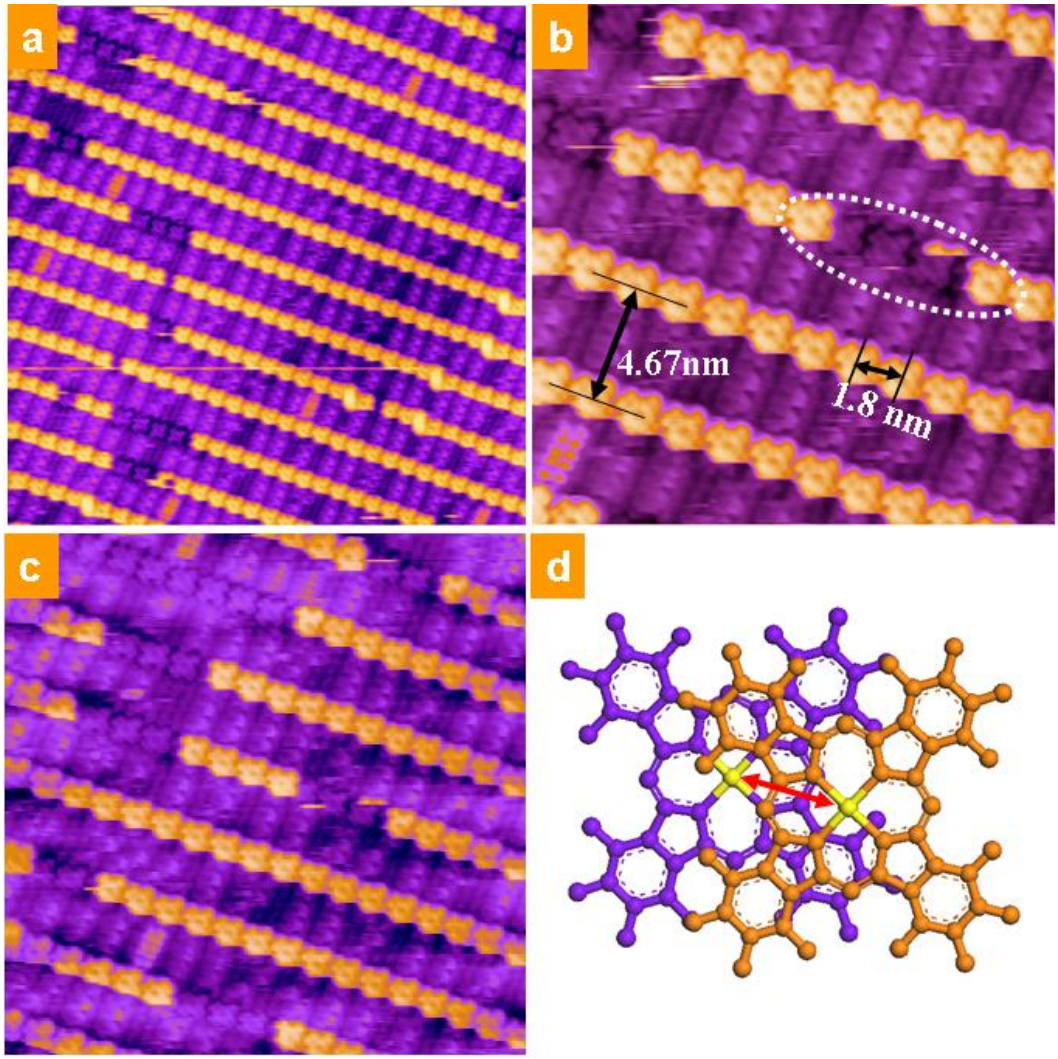

Figure 5.7 (a) and (b) display the formation of the 2nd layer F_{16}CuPc molecular chain arrays (V_{tip} = 2.8 V; panel a, 50 × 50nm^2; panel b, 20 × 20nm^2). The 2nd layer F_{16}CuPc preferentially adsorbs atop the underlying F_{16}CuPc molecules, as highlighted by the ellipse in panel b. The top (orange) and the underlying (purple) F_{16}CuPc molecules adopt a slipped geometry, as shown by the schematic drawing in (d). (c) At lower F_{16}CuPc coverage, there are more vacancies on the 2nd layer F_{16}CuPc stripes, compared to that shown in panel a (30 × 30 nm^2, V_{tip} = 2.0 V).

5.4 Summary

Preferential molecular adsorption on non-porous supramolecular networks has been demonstrated using the model systems of 2nd layer F_{16}CuPc on DIP:F_{16}CuPc and 6P:F_{16}CuPc supramolecular surface nanotemplates. The arrangement of the 2nd layer supramolecular nanostructures, individual molecular

dots or linear molecular chains, is strongly influenced by the underlying molecular networks. This suggests a possible large scale method to fabricate organic nanostructure arrays with desired functionality for potential use in molecular nanodevices. The interlayer π-π interactions between the 1st and 2nd layer F_{16}CuPc molecules play important roles in facilitating the preferential adsorption. Such preferential adsorption at particular molecular sites of a binary molecular template via specific intermolecular interactions may be used as an ideal model system to investigate the intermolecular interactions and kinetic growth processes at the atomic scale.

Reference:

[1] D. Bonifazi, S. Mohnani, A. Llanes-Pallas, A. *Chem. Eur. J.* **15**, 7004-7025 (2009).

[2] T. Kudernac, S. Lei, J. A. A. W. Elemans, S. De Feyter, *Chem. Soc. Rev.* **38**, 402-421 (2009).

[3] L. Sanchez, R. Otero, J. M. Gallego, R. Miranda, M. Martin, *Chem. Rev.* **109**, 2081-2091 (2009).

[4] L. J. Wan, *Acc. Chem. Res*. **39**, 334-342 (2006).

[5] J. Mao, H. Zhang, Y. H. Jiang, Y. Pan, M. Gao, W. D. Xiao, H. J. Gao, *J. Am. Chem. Soc.* **131**, 14136-14137 (2009).

[6] F. Cicoira, C. Santato, F. Rosei, *Top. Curr. Chem.* **285**, 203-267 (2008).

[7] H. Dil, J. Lobo-Checa, R. Laskowski, P. Blaha, S. Berner, J. Osterwalder, T. Greber, *Science* 319, 1824-1826 (2008).

[8] M. Corso, W. Auwärter, M. Muntwiler, A. Tamai, T. Greber, J. Osterwalder, *Science* **303**, 217-220 (2004).

[9] W. Chen, A. T. S. Wee, *J. Phys. D: Appl. Phys.* **40**, 6287-6299 (2007).

[10] S. Stepanow, M. Lingenfelder, A. Dmitriev, H. Spillmann, E. Delvigne, N. Lin, X. Deng, C. Cai, J. V. Barth, K. Kern, *Nature Materials* **3**, 229-233 (2004).

[11] J. A. Theobald, N. S. Oxtoby, M. A. Phillips, N. R. Champness, P. H. Beton, *Nature* **424**, 1029-1031 (2003).

[12] P. A. Staniec, L. M. A. Perdigao, A. Saywell, N. R. Champness, P. H. Beton, *ChemPhysChem* **8**, 2177-2181 (2007).

[13] L. M. A. Perdigao, A. Saywell, G. N. Fontes, P. A. Staniec, G. Goretzki, A. G. Phillips, N. R. Champness, P. H. Beton, *Chem. Eur. J.* **14**, 7600-7607 (2008).

[14] R. Madueno, M. T. Raisanen, C. Silien, M. Buck, *Nature* **454**, 618-621 (2008).

[15] L. Piot, F. Silly, L. Tortech, Y. Nicolas, P. Blanchard, J. Roncali, D. Fichou, *J. Am. Chem. Soc.* ***131***, 12864-12865 (2009).

[16] H. L. Zhang, W. Chen, L. Chen, H. Huang, X. S. Wang, J. Yuhara, A. T. S. Wee, *Small* **3**, 2015-2018 (2007).

[17] L. Chen, W. Chen, H. Huang, H. L. Zhang, J. Yuhara, A. T. S. Wee, *Adv. Mater.* **20**, 484-488 (2008).

[18] D. Bonifazi, A. Kiebele, M. Stöhr, F. Cheng, T. Jung, F. Diederich, F. Spillmann, *Adv. Funct. Mater.* **17**, 1051-1062 (2007).

[19] S. Lei, M. Surin, K. Tahara, J. Adisoejoso, R. Lazzaroni, Y. Tobe, S. De Feyter, *Nano Lett.* **8**, 2541-2546 (2008).

[20] B. Calmettes, S. Nagarajan, A. Gourdon, M. Abel, L. Porte, R. Coratger, *Angew. Chem. Int. Ed.* **47**, 6994-6998 (2008).

[21] J. Lu, S. B. Lei, Q. D. Zeng, S. Z. Kang, C. Wang, L. J. Wan, C. L. Bai, *J. Phys. Chem. B* **108**, 5161-5165 (2004).

[22] X. H. Kong, K. Deng, Y. L. Yang, Q. D. Zeng, C. Wang, *J. Phys. Chem. C* **111**, 17382-17387 (2007).

[23] O. Ivasenko, J. M. MacLeod, K. Yu. Chernichenko, E. S. Balenkova, R. V. Shpancheko, G. V. Nenajdenko, F. Rosei, D. F. Perepichka, *Chem. Comm.* 1192-1194 (2009).

[24] Y. L. Huang, W. Chen, H. Li, J. Ma, J. Pflaum, A. T. S. Wee, *Small* **6**, 70-75 (2010).

[25] E. Barrena, D. G. de Oteyza, H. Dosch, Y. Wakayama, *ChemPhyChem* **8**, 1915-1918 (2007).

[26] Y. L. Huang, W. Chen, S. Chen, A. T. S. Wee, *Appl. Phys. A* **95**, 107-11 (2009).

[27] H. Huang, W. Chen, A. T. S. Wee, *J. Phys. Chem. C.* **112**, 14913-14918 (2008).

[28] X. Chen, Y. S Fu, S. H. Ji, T. Zhang, P. Cheng, X. C. Ma, X. L. Zou, W. H. Duan, J. F. Jia, Q. K. Xue, *Phys. Rev. Lett.* **101**, 197208 (2008).

[29] http://en.wikipedia.org/wiki/Chi-square_distribution.

[30] http://en.wikipedia.org/wiki/Pearson%27s_chi-square_test**.**

[31] W. Chen, H. L. Zhang, H. Huang, L. Chen, A. T. S. Wee, *Appl. Phys. Lett*. ***92*****,** 193301 (2008).

[32] W. Chen, H. Huang, A. T. S. Wee, *Chem. Commun*., 4276-4278 (2008).

[33] C. B. France, B. A. Parkinson, *Appl. Phys. Lett.* **82**, 1194 (2003).

[34] K. N. Baker, A.V. Fratini, T. Resch, H. C. Knachel, W. W. Adams, E. P. Socci, B. L. Farmer, *Polymer* **34**, 1571-1578 (1993).

[35] G. Koller, S. Berkebile, M. Oehzelt, P. Puschnig, C. Ambrosch-Draxl, F. P. Netzer, M.G. Ramsey, *Science* **317**, 351-355 (2007).

Chapter 6

Dipolar Molecule: Chloroaluminum Phthalocyanine

6.1 Introduction

The construction of low-dimensional organic molecular layers is an alternative route to fabricate devices at the nanometer scale to meet the requirements of microelectronics device miniaturization.[1-7] Organic molecules with permanent magnetic or electric polarities have attracted attention as promising materials for high-density data-storage bits, single-molecule magnets, organic spintronics, biosensors and so on.[8-11] The chloroaluminum phthalocyanine (ClAlPc) molecule with electric dipole moment perpendicular to its molecular π-plane, is investigated in this chapter.[12] The ClAlPc molecular structure is shown in Figure 6.1, where the Al-Cl bond is out-of-plane and of a length of 2.167 Å. As the Al atom is positively charged and Cl atom is negatively charged, the molecule has an electric dipole moment (P = 1.87 debye) which permanently points from Cl to Al (as shown in Figure 6.1b).[12] There are two possible configurations for this non-planar molecule to adopt when it adsorbs on a surface, denoted by Cl-up and Cl-down configurations in Figure 6.1b. A molecular dipole monolayer can be formed by neatly aligning all ClAlPc molecular dipoles up or down.[12, 13] In section **6.2**,

the formation of single-layer and bi-layer ClAlPc films on HOPG are investigated by LT-STM.

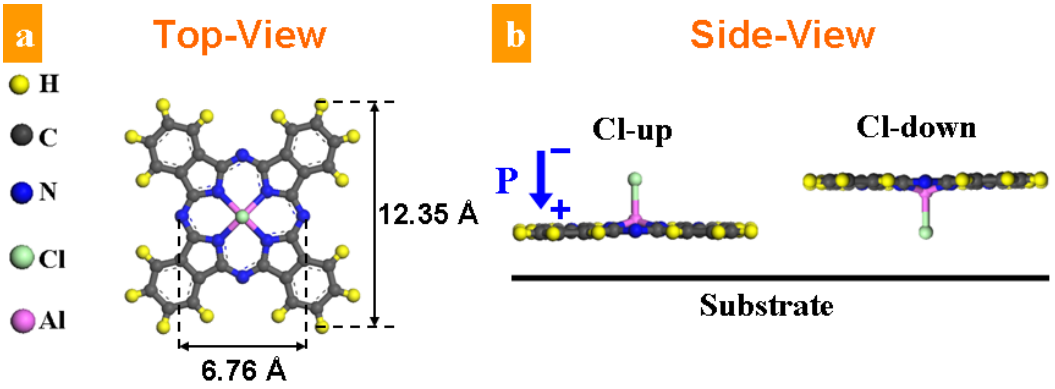

Figure 6.1 (a) ClAlPc molecular structure and its dimensions. (b) Side views of ClAlPc molecules adsorbed on a substrate with Cl-up and Cl-down configurations respectively.

Nanoscale phase separation of binary or multicomponent molecular systems on surfaces represents one promising approach to build long-range ordered molecular nanostructure arrays.[14, 15] This approach has been widely used in organic solar cells for effective interface nanostructuring to maximize the donor-acceptor interface area for efficient exciton dissociation and charge separation.[16-22] In this chapter, we demonstrate the fabrication of molecular dipole chain arrays using nanoscale phase separation of a binary molecular system on graphite (section **6.3**). With the co-adsorption of DIP, ClAlPc molecular dipole chain arrays are formed via nanoscale phase separation. The inter-chain spacing of the dipole chain arrays can be tuned by varying the DIP coverage. By replacing ClAlPc with non-dipolar CuPc, similar binary molecular chain arrays are formed as a result of phase separation.

Controlled single-molecule manipulation has potential applications in

molecule-based functional devices where individual molecules can serve as memory elements, diodes, transistors, or switches. STM has been shown to be a powerful tool in manipulating single atoms or molecules.[23-26] The tip-induced atomic/molecular dynamic motion (e. g., desorption, diffusion, slide and rotation) or chemical reaction is attributed to electrostatic forces, electron-induced vibration and so on. The controlled flipping of individual ClAlPc molecules by an STM tip on graphite substrate is reported in section **6.4**. The reversible switching of the molecular dipole moment is proposed to be induced by electrostatic forces. The realization of single-molecule flipping is a demonstration of the ultimate spatial resolution achievable using molecular arrays, and has promising applications in ultra-high density data storages.

6.2 ClAlPc thin films on HOPG

ClAlPc thin films were deposited at a constant rate of 0.15 ML min^{-1} on HOPG substrates at room temperature. Before the HOPG surface is fully covered, ClAlPc molecules aggregate into either single-layer or bi-layer islands with irregular shapes on the graphite terraces. Large-scale STM images of the HOPG surface with 0.8 ML ClAlPc coverage are shown in Figure 6.2. In Figure 6.2a (150×150 nm^2), a single-layer ClAlPc island (right) with irregular-shape edge (white dashed line) is formed and coexists with bare HOPG surface with dissociated molecules (left). This single-layer island is composed of two domains (separated by the red dashed line) rotated relative to each other. Red arrows

denote the molecular stripe direction for the top and bottom domains respectively. Figure 6.2b (50×50 nm^2) demonstrates the formation of a single-layer + bi-layer island, where the bare HOPG surface is also observable at the left side of the image.

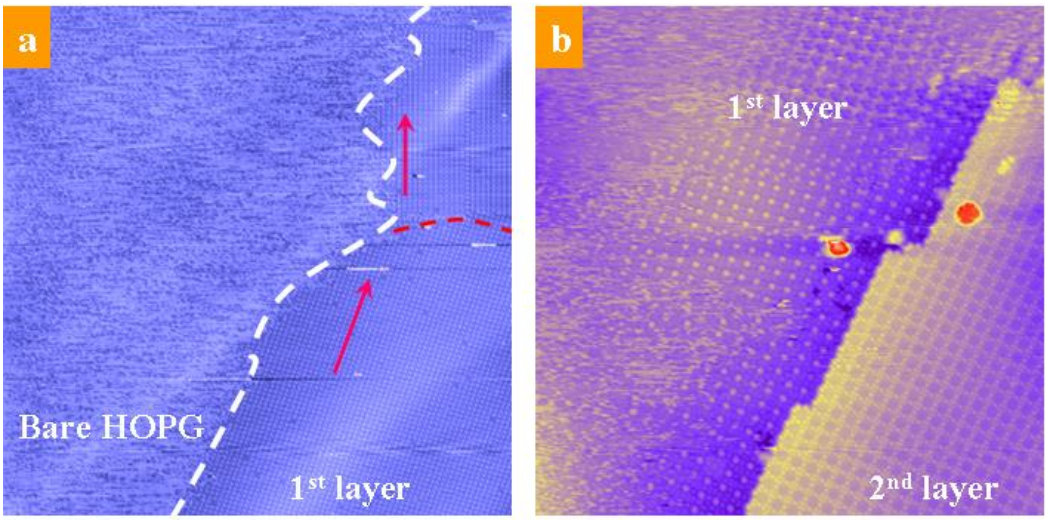

Figure 6.2 Large-scaled STM images demonstrate the formation of the single-layer + bi-layer ClAlPc film at 0.8 ML coverage. (a) 150×150 nm^2, V_{tip} = 2.4 V; and (b) 50×50 nm^2, V_{tip} = 2.6 V.

In Figure 6.3, high-resolution STM images show the supramolecular packing structures of the single-layer ClAlPc islands on HOPG. At the 1st monolayer, most ClAlPc molecules (> 98%) appear as a four-lobe feature with a bright central protrusion. The protrusions are in orange in panels 6.3a, c and d, and in white in panels 6.3e and f, and are attributed to Cl atoms pointing out of the molecular π-planes. This molecular protrusion suggests that the ClAlPc molecules adopt the Cl-up configuration (Figure 6.1b). Thus, a molecular dipole monolayer is formed on the graphite as the ClAlPc molecular dipoles are neatly aligned up. Two overall arrangements coexist in the 1st monolayer, namely an ordered phase

(Figure 6.3a-d) and a disordered phase (Figure 6.3 e and f). The molecularly resolved STM image of Figure 6.3a (30×30 nm^2) corresponds to the close-packed ordered phase with 4-fold symmetry, where brighter and dimmer defects are observable. Figure 6.3c and d are enlarged images corresponding to panel 6.3a, which are captured at different tip bias (2.4 V and -2.4 V respectively, and I_{set} = 0.1 nA) at the same area. The square unit cell highlighted in panel 6.3c has dimensions of 1.51×1.51 nm^2. The molecule with brighter contrast compared to its surrounding molecules at both positive and negative tip bias (indicated by purple arrows), is suggested to be ClAlPc molecules with Cl-down configuration at the 1st layer; and the molecule with dimmer contrast (denoted by green arrows) is attributed to an impurity from the ClAlPc molecular source.

Figure 6.3e (50×50 nm^2) and its corresponding zoom-in image in Figure 6.3f (15×15 nm^2) demonstrate the arrangement of the disordered phase. Dashed lines in panel 6.3f indicate that the ClAlPc molecules are packing into long molecular stripes extending over the HOPG terraces. Two different domains, namely **S**- and **R**- domains with different in-plane molecular orientations, are observed in the disordered region. The **S**- and **R**- domains possess the same periodicity of about 1.51 nm along the strip direction (dashed lines). By defining an azimuth angle θ between the ClAlPc molecular axis and the stripe direction, we have $\theta_S = 20° \pm 2°$ (between the blue arrow and the white dashed line) for the **S**-domain and $\theta_R = 60° \pm 2°$ (between the green arrow and the black dashed line) for the **R**-domain. The supramolecular arrangement of the S-domain is actually the same as that of the ordered phase (Figure 6.3a-d) with square unit cell. The disordered phase is

predominantly comprised of the **S**-domains (more than 80%), and the insertions of the **R**-domains are the result of the lack of long-range order. As highlighted by the short purple line ***AB***, the intermolecular spacing between two nearest neighboring **S**- and **R**- molecules (from central Cl atom to Cl atom) is of 1.70 ± 0.02 nm, which is larger than the intermolecular spacing of 1.51 nm along the molecular stripe. Thus, the mismatch between the neighboring molecular stripes can enlarge the spacing between two neighboring molecular dipoles, which helps to reduce the in-plane stress of the molecular dipole monolayer.

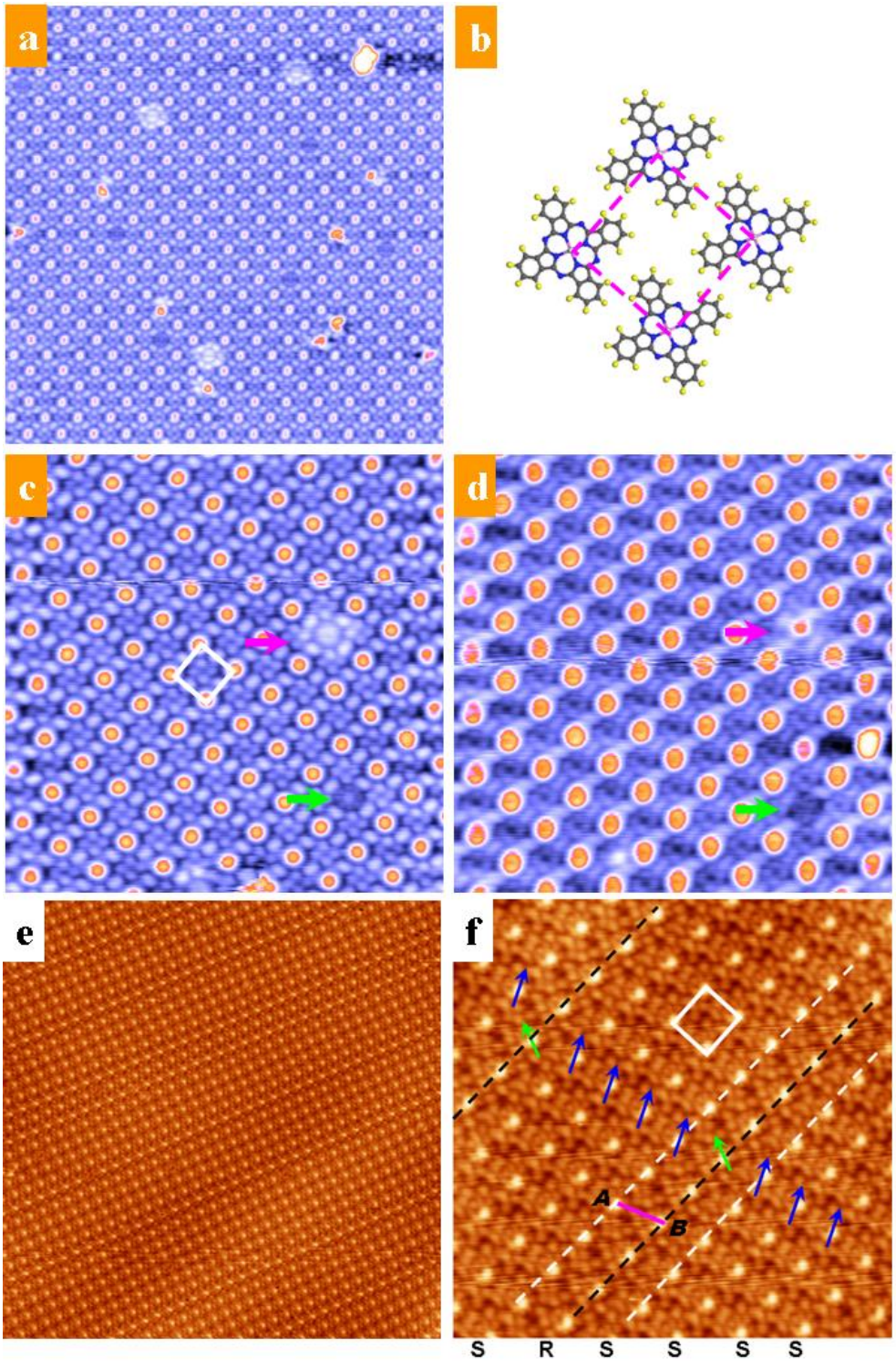

Figure 6.3 Single-layer ClAlPc islands on HOPG. (a) The well-ordered phase of the 1st layer ClAlPc on HOPG (30×30 nm^2, V_{tip} = 2 V); (c) and (d) are correspondingly enlarged image recorded at the same area at different tip bias, 2.4 V and -2.4 V respectively (I_{set} = 0.1 nA, 15 ×15 nm^2); (b) Proposed molecular model for the square unit cell in panel (c). (e) Large-scale STM image (50×50 nm^2, V_{tip} = 2.5 V), and (f) a zoom-in image of the disordered region comprising **S**-

and **R**- domains. The arrows denote the molecular axis (15×15 nm^2, V_{tip} = 2.5 V), where green ones for the **R**-domains, and blue ones for the **S**-domains.

The STM image in Figure 6.4 displays a single-layer + bi-layer island of ClAlPc on HOPG. The bright domain on the left-hand side represents the bi-layer ClAlPc film, while the dimmer domain on the right-hand side corresponds to the monolayer film. The lateral profile in Figure 6.4c corresponding to the black line in panel 6.4a reveals the height difference of ~0.3 nm between the bi-layer and single-layer films, which similar to the layer height of other planar Pc (e. g., F_{16}CuPc or CuPc) monolayer with flat-lying configuration.[27] The enlarged STM image with sub-molecular resolution in Figure 6.4b demonstrates the supramolecular packing structure of the 2nd layer ClAlPc. As noted by the imposed molecular models at the lower right corner, each four-lobe feature with a central depression at positive tip-bias represents a 2nd layer ClAlPc molecule. Such molecular characteristic is similar to other planar Pc molecules under STM imaging.[27] The dark four-lobe features highlighted by the white circle in Figure 6.4a are attributed to ClAlPc vacancies in the 2nd layer. The 2nd layer ClAlPc molecules are suggested to adopt the Cl-down configuration, in contrast to the 1st layer ones preferring the Cl-up configuration. The 2nd layer ClAlPc molecules are also close packed with 4-fold symmetry. The 2nd layer has the same 1.51 × 1.51 nm^2 square unit cell as the ordered domain of the 1st monolayer. Through close inspections of the edges of the bi-layer islands, we find that the 2nd layer ClAlPc molecule perches on the center of the 1st layer unit cell (ordered domains). The

stacking structure of the 1st and 2nd layers is shown in the schematic drawing in Figure 6.4d, where the purple molecule with a gray center represents the 1st layer molecule with Cl-up configuration and the blue one represents the 2nd layer molecule with Cl-down configuration (Cl atom is not observable). Such bi-layer packing structure of the ClAlPc film has been suggested previously by the measurement of metastable atom electron spectroscopy.[12] It also has been observed for other non-planar Pc molecular thin films.[12]

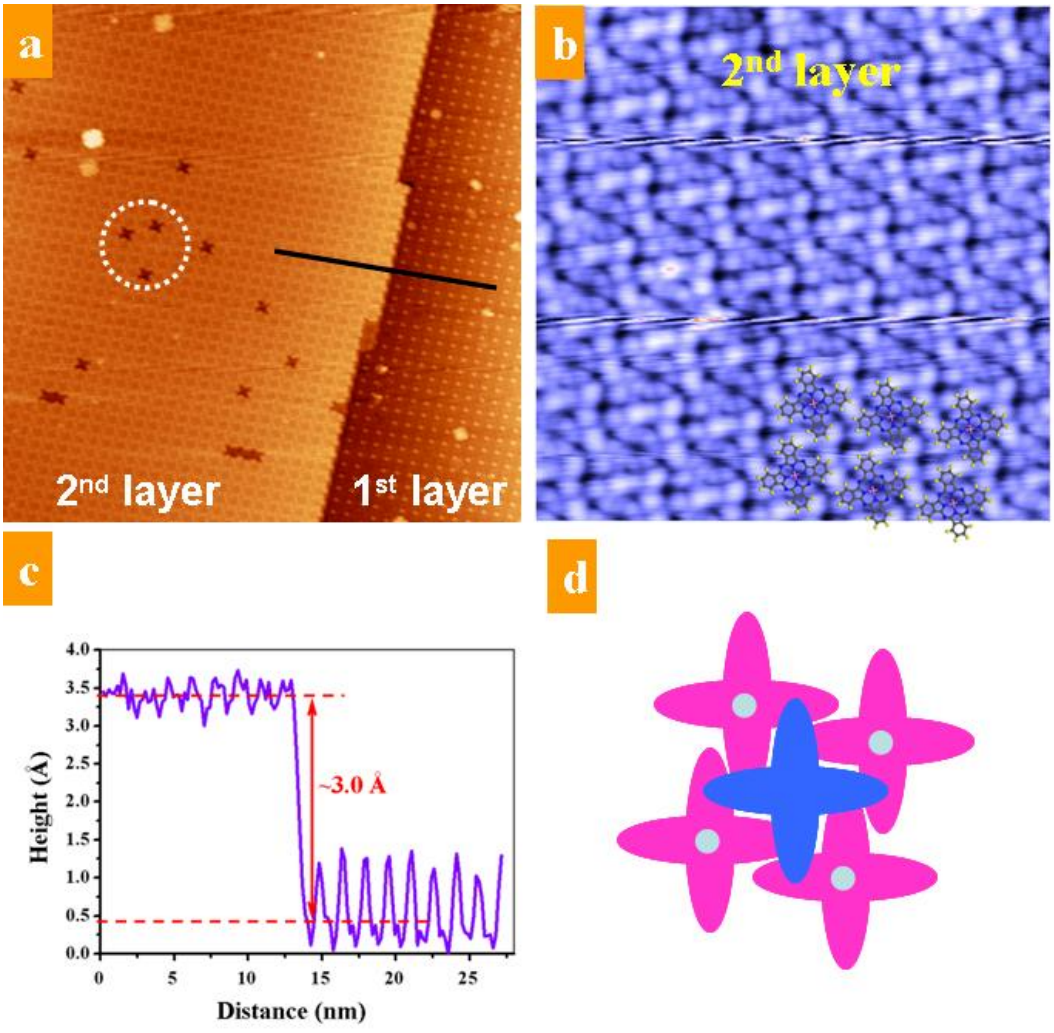

Figure 6.4 (a) Large-scale STM image shows the formation of the single-layer + bi-layer ClAlPc island, where the white circle highlights three ClAlPc molecular vacancies (60×60 nm^2, V_{tip} = 2.8 V). (b) A zoom-in of the 2nd layer region (10×10 nm^2, V_{tip} = 2 V). (c) The lateral profile

corresponding to the black line in panel (a) reveals a height difference of 3 Å. (d) Proposed stacking structure of the ClAlPc bi-layer film, where the purple molecules represent the 1st layer molecules and the blue one represents the 2nd layer molecule.

6.3 The formation of molecular dipole chain arrays via nanoscale phase separation

Molecular-resolved STM images in Figure 6.5 demonstrate the formation of ClAlPc molecular chain arrays via nanoscale phase separation by the co-adsorption with DIP molecules (certain amount of DIP was subsequently deposited on the HOPG surface covered with sub-monolayer ClAlPc at RT, or *vice versa*). At the ClAlPc:DIP co-adsorption ratio of 1:1, a highly ordered binary molecular array is formed by an alternating arrangement of a single ClAlPc molecular chain with a single DIP molecular chain as shown in Figure 6.5a and its corresponding zoom-in image in Figure 6.5c. Every bright protrusion in orange corresponds to the central Cl atom of each ClAlPc molecule with Cl-up configuration, and the leaf-like pattern is attributed to the DIP molecules.[28] In decreasing the ClAlPc:DIP ratio to 2:3 (Figure 6.5b), the ClAlPc molecular chain array is interconnected by single or double DIP molecular chains without long range order, where the label '**S**' refers to a single DIP molecular chain and '**D**' to a double one. A well-ordered arrangement is formed as the ClAlPc:DIP ratio is further decreased to 1:2 (Figure 6.5d), comprising single ClAlPc molecular dipole chains separated by double DIP molecular chains. The approximately rectangular unit cells of two ordered molecular dipole arrays are denoted in Figure 6.5c and d respectively,

with dimensions of 1.51 × 2.65 nm^2 for the 1:1 array and enlarged to 1.51 × 3.78 nm^2 for the 1:2 array. Correspondingly, the proposed molecular models are shown in Figure 6.5e and f respectively. Thus, the molecular dipole chains can be formed at various relative molecular coverages of ClAlPc and DIP with tunable inter-chain separation.

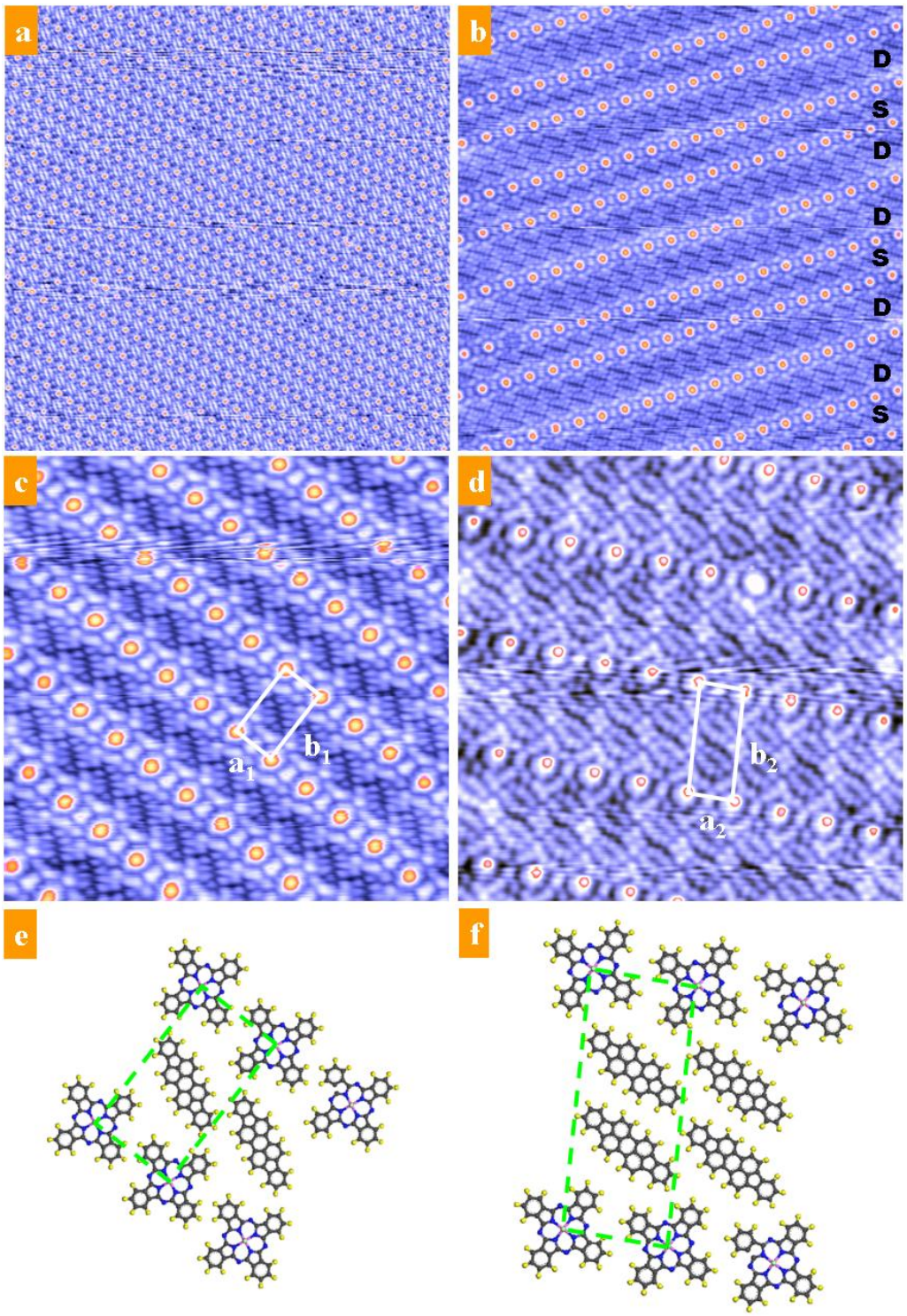

Figure 6.5 Molecular dipole chain arrays formed by the co-adsorption of ClAlPc and DIP molecules: (a) large-scale and (c) enlarged STM images at the ClAlPc:DIP ratio of 1:1 (panel a, 50 × 50 nm^2, V_{tip} = 2.2 V; panel c, 15 × 15 nm^2, V_{tip} = 20 V); (b) DIP-rich phase (30 × 30 nm^2, V_{tip} = 2.0 V), and (d) at the lower ClAlPc:DIP ratio of 1:2 (15 × 15 nm^2, V_{tip} = 2.2 V). (e) and (d) are schematic models showing the supramolecular packing structure of panel (c) and (d) respectively.

Similar nanoscale phase separations were observed in the binary molecular system of DIP with non-dipolar CuPc phthalocyanine molecule. Figure 6.6 shows the supramolecular packing structures of CuPc:DIP binary monolayers with different relative molecular ratios. Large-scale images in Figure 6.6a and b correspond to the CuPc-rich region and DIP-rich region respectively, where the CuPc chains have brighter contrast compared to the DIP chains. As previously observed for ClAlPc, 1D linear CuPc molecular chains and DIP molecular chains are formed. In the CuPc-rich region, single DIP molecular chains are interconnected through single- or multi- CuPc molecular chains (Figure 6.6a). In Figure 6.6c with CuPc:DIP ratio of 1:1, an ordered binary molecular array is formed comprising alternating single CuPc and single DIP molecular chains, similar to that in Figure 6.5c. The unit cell is highlighted by the white rectangle with dimensions of c_1=1.50 nm and d_1=2.60 nm. At the CuPc:DIP ratio of 1:2 (Figure 6.6b and d), single CuPc molecular chains are separated by double DIP molecular chains, thereby forming a larger rectangle unit cell with c_2=1.50 nm and d_2=3.72 nm. Such formation of linear CuPc:DIP molecular chain arrays by nanoscale phase separation has also been observed on Ag(111).[14] It suggests that such nanoscale phase separation is a common feature in the binary systems of some planar/non-planar phthalocyanine with DIP.

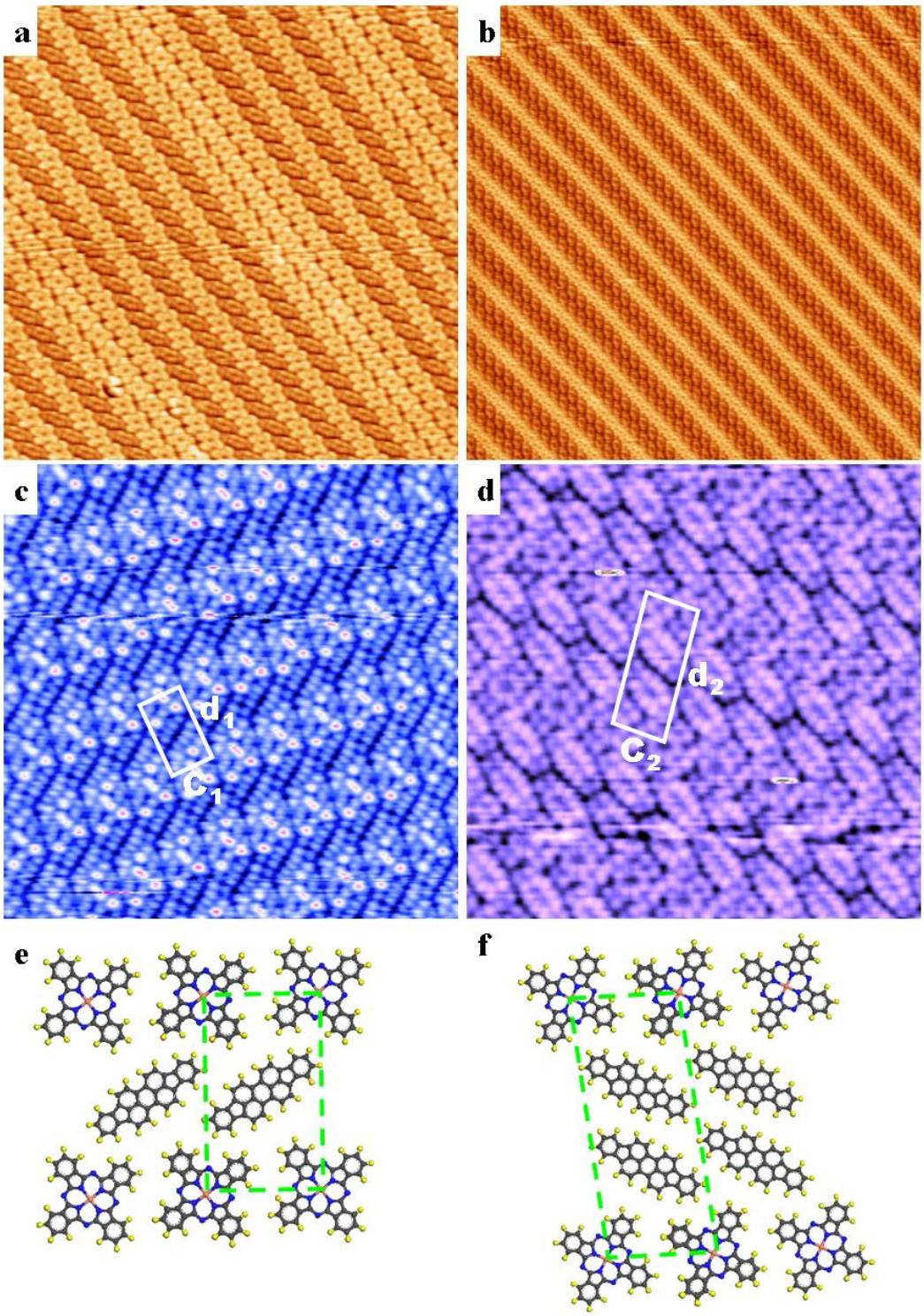

Figure 6.6 Large-scale STM images show (a) the CuPc-rich region and (b) DIP-rich region (panel a, 30 × 30 nm^2, V_{tip} = 2.0 V; panel b, 50 × 50 nm^2, V_{tip} = 2.0 V) for the CuPc:DIP binary system on graphite.. (c) and (d) correspond to the ordered phases formed at the CuPc:DIP ratios of 1:1 and 1:2 respectively, whose schematic molecular model is given below each STM image. (panel c, 15 × 15 nm^2, V_{tip} = 2.0 V; panel d, 10 × 10 nm^2, V_{tip} = 2.2 V)

6.4 Single-molecule manipulation

Molecular switches on surfaces are of great interest because they are potential components in single-molecule-based functional devices. Here, we demonstrate that a single-molecule switch can be obtained via reversible transformations of the ClAlPc molecular configurations in the close-packed layer. We operated and characterized the switch by LT-STM at both 4 K and 77K, and only the STM images recorded at 4K were discussed here. As previously shown in Figure 6.2, most of the 1st layer ClAlPc molecules are absorbed on HOPG surface with Cl-up configuration; the ones adopting Cl-down configuration are easily distinguished as they have brighter contrast without central protrusion comparing to the Cl-up molecules. The configuration switch from the Cl-up (denoted as '1' state) to Cl-down (denoted as '0' state) can be induced by positioning the tip above the molecule and subsequently applying a positive-bias voltage pulse. As demonstrated in Figure 6.7a, after applying a (4.5 V, 2 ms) pulse atop a target ClAlPc molecule, the molecule flipped from '1' to '0' as marked by the yellow arrow. Subsequently, a series of (4.5 V, 2 ms) pulses were applied sequentially as the tip was positioned above different molecules marked by green crosses in Figure 6.7a-e. The underlying molecules were correspondingly switched from '1' states to '0' states as shown in Figure 6.7b-f. During the applications of pulses, the tip was held at constant-height (e.g., V_{set} = 2.2 V, I_{set} = 80 pA, and a tip-molecule separation $\boldsymbol{D}$ of about 10 Å). The ClAlPc molecular features in panel a-e are a bit different from that in panel f, which is suggested to be caused by

different tip states. Nevertheless, the central protrusion of the Cl-up molecules and the brighter contrast of the Cl-down molecules are still distinguishable.

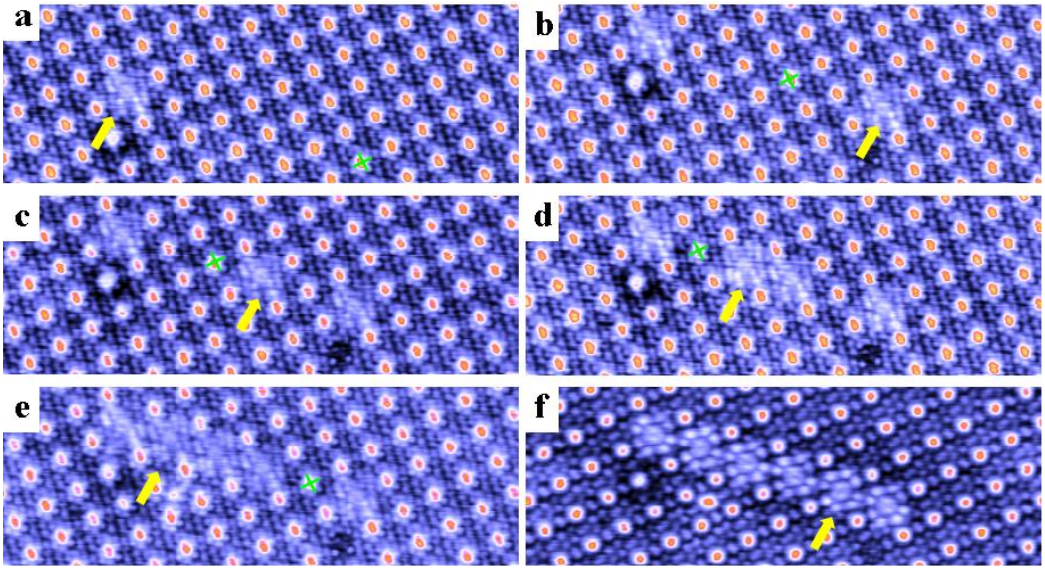

Figure 6.7 Sequence of STM images illustrating individual switching of Cl-up molecules ('1') to Cl-down molecules ('0') on HOPG surface. The target molecules in state '1' are denoted by green crosses in panel a, b, c, d, and e. After applying a series (4.5 V, 2 ms) pulses, the addressed molecules consequently flipped to state '0' as indicated by the yellow arrows in panel b, c, d, e and f respectively. (Sizes: 7 × 20 nm^2; V_{tip} = 2.2 V, I_{set} = 80 pA; 4 K).

The single-molecule switching is controllable and confined to the specifically addressed molecule. Thereby, specific patterns can be written on the molecular dipole monolayer. The high-resolution STM images in Figure 6.8 demonstrate the process of writing a label 'N' on the molecule-dot matrix, where each ClAlPc molecule represents a pixel. The ClAlPc molecules are neatly aligned in Cl-up configuration in Figure 6.8a, where a defect (impurity) is indicated by a purple arrow. After applying (4.5 V, 2 ms) pulses at 7 different Cl-up molecules (denoted by green crosses) sequentially as described above, the target molecules flipped

into Cl-down states as shown in Figure 6.8b. The molecular configuration can also be transformed reversibly from '0' to '1' conformation. We applied a negative pulse (-3 V, 2 ms) at a Cl-down molecule (denoted by the red cross) in panel 6.8b, and found that it reversely flipped to the Cl-up configuration in Figure 6.8c. This molecule (indicated by yellow arrow in Figure 6.8c) transformed to '0' state again by applying the positive pulse (Figure 6.8d). The other molecule that revealed the reversable manipulation is highlighted by the red cross in Figure 6.8c, and is correspondingly switched back to '1' state in Figure 6.8d. In Figure 6.8d, the letter 'N' is successfully written in an area of 12 × 20 nm^2. The reverse manipulation suggests that this dipolar molecule could be used as high-density storage bits, as it is possible to write, read and erase information on the molecular dipole arrays. The density of the storage made of such dipolar molecules could reach 40 TBits per cm^2, which is hundreds times of the highest density has been reached nowadays.

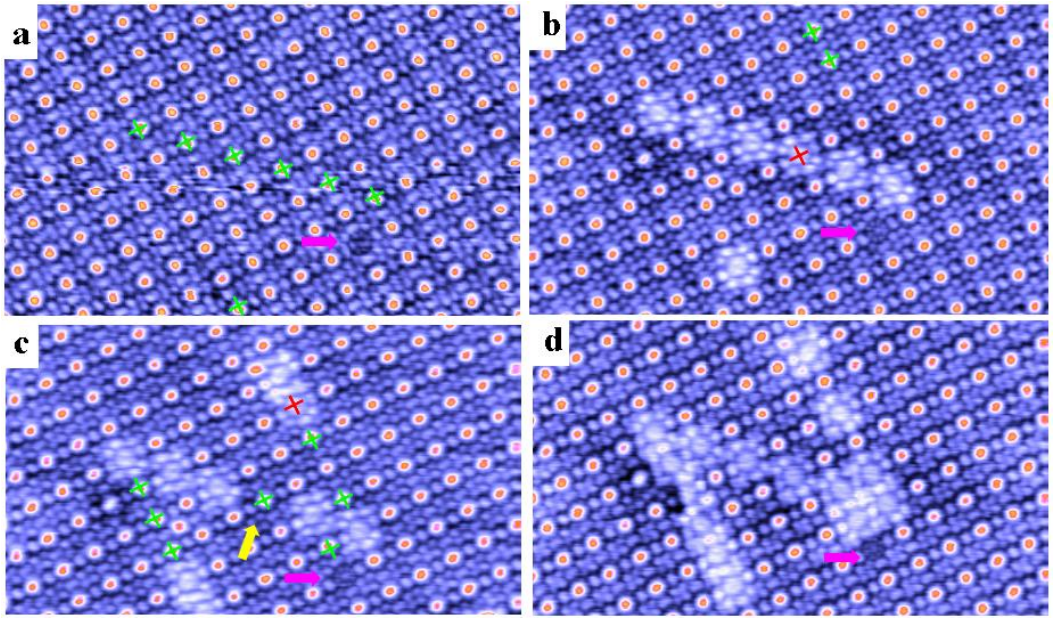

Figure 6.8 A letter 'N' is written on the molecule-dot matrix by STM. Green crosses denote the target molecules applied with positive-bias tip voltage pulses, and the red ones applied with negative-bias pulses. (a) - (d) were subsequently recorded at the same area after applying bias voltage pulses, where the purple arrows mark the same defect molecule. The yellow arrow in panel c highlights the reversable manipulation of a molecule: '1' to '0' from panel a to b, '0' to '1' from panel b to c, and '1' to '0' from panel c to d. (Size: 12 × 20 nm^2; V_{tip} = 2.2 V, I_{set} = 80 pA; 4 K)

The switching manipulations are clearly dependent on the sign of the bias pulse. Hence, we suggest that electrostatic force between the tip and the molecule is the driving mechanism that controls the molecular switching. As demonstrated in the schematic drawing of Figure 6.9, the ClAlPc molecule is actually exposed in an external electric field formed between the tip and the substrate during the application of bias pulse (and also STM scanning process). The electric field is of the order of 10^9 V/cm as the tip-sample separation is typically around 10 Å. The electric field surrounding the tip is dependent on its curvature, and has the highest field intensity at the vicinity of the tip.[29, 30] When a positive-bias pulse is applied

to the Cl-up molecule, the molecule is lifted up by the attractive electrostatic force between the positive-charged tip and the negative-charged Cl atom, making it unstable and causing it to flip into the Cl-down configuration. As the tip-molecule (sample) separation is typically around 10 Å and the space between the ClAlPc molecular π-plane and the graphite substrate is around 3 Å, the total tip-graphite separation is 13 Å (if the tip is precisely positioned atop the Cl atom, the tip-graphite separation could be 15 Å if we take into account the length of the Al-Cl bond at about 2 Å). The dimensions of the ClAlPc are shown in Figure 6.1, where the width of the molecule is about 12.3 Å, and the radius of the porphyrine is about 6.8 Å. Thus, the separation geometry between the tip and the graphite allows the underlying ClAlPc molecule to flip over. The Cl-down configuration is more stable under positive-charged tip due to the repulsive force between the positive-charged tip and the positive-charged Al atom. Conversely, the switching from Cl-down state to Cl-up state is facilitated by a negative-bias voltage pulse, as the positive-charged Al atom is attracted upwards to the negative-charged tip. Further experiments are required to confirm our proposed mechanism.

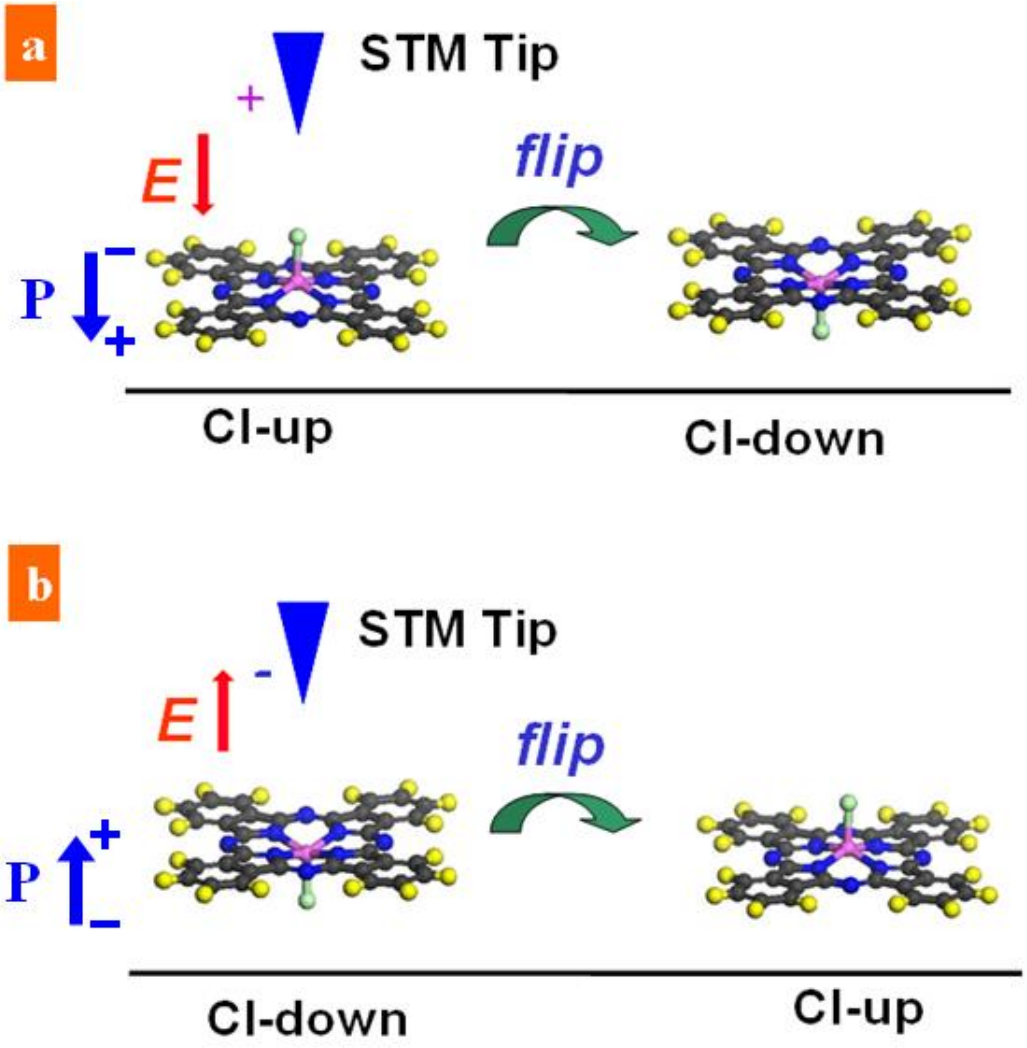

Figure 6.9 The schematic drawing demonstrates the possible mechanism that controls the molecular switching: (a) Cl-up state flips to Cl-down state by positive-bias voltage pulse and (b) Cl-down state flips to Cl-up state by negative-bias voltage pulse.

6.5 Summary

In summary, the formation of molecular dipole chain arrays has been demonstrated by *in-situ* LT-STM imaging. The pure ClAlPc single layer film forms a well-ordered molecular dipole monolayer array with the Cl-up

configuration on graphite surface. Disordered domains are also observable at the 1st monolayer to reduce the in-plane dipolar stress. The 2nd layer ClAlPc molecules adopt Cl-down configuration and stack atop the ordered domains of the 1st monolayer with the same periodicity. After co-adsorption of sub-monolayer ClAlPc with DIP, molecular dipole chain arrays can be fabricated with various inter-chain separations at different relative molecular coverages. In the binary molecular system of CuPc with DIP, nanoscale phase separation is also observable, resulting in the formation of similar molecular chain arrays. Single-molecule manipulation controlled by an STM tip is also demonstrated at 4K. The controlled flipping of individual ClAlPc molecules from Cl-up to Cl-down and *vice versa* is attributed to strong electrostatic forces. The precise and reversible control makes the ClAlPc molecule a promising basic information bit for ultrahigh density information storage.

References:

[1] C. Joachim, J. K. Gimzewski, A. Aviram, *Nature* **408**, 541-548 (2000).

[2] A. Nitzan, M. A. Ratner, *Science* **300**, 1384-1389 (2003).

[3] C. Joachim, M. A. Ratner, *Proc. Natl. Acad. Sci. USA* **102**, 8801-8808 (2005).

[4] R. L. Carroll, C. B. Gorman, *Angew. Chem. Int. Ed.* **41**, 4379-4400 (2002).

[5] J. V. Barth, G. Costanitini, K. Kern, *Nature*, **437**, 671-679 (2005); J. V. Barth, *Annu. Rev. Phys. Chem.* **58**, 375-407 (2007).

[6] S.-S. Li, B. H. Northrop, Q. H. Yuan, L. J. Wan, P. J. Stang, *Acc. Chem. Res.*

42, 249-259 (2009); L. J. Wan, *Acc. Chem. Res.* **39**, 334-342 (2006).

[7] F. Cicoira, C. Santato, F. Rosei, *Top. Curr. Chem.* **285**, 203-267 (2008).

[8] G. Christou, *Polyhedron* **24**, 2065-2075 (2005).

[9] A. Naitabdi, J.-P. Bucher, P. Gerbier, P. Rabu, M. Drillon, *Adv. Mater.* **17**, 1612-1616 (2005).

[10] R. Sessoli, A. K. Powell, *Coord. Chem. Rev.* **253**, 2328-2341 (2009).

[11] A. Vermeulen, H. Zhou, A. Pardi, *J. Am. Chem. Soc.* **122**, 9638-9647(2000).

[12] S. Kera, H. Yamane, H. Honda, H. Fukagawa, K. K. Okudaira, N. Ueno, *Surf. Sci.* **566,** 571-578 (2004).

[13] Y. Azuma, T. Yokota, S. Kera, M. Aoki, K. K. Okudaira, Y. Harada, N. Ueno, *Thin Solid Films* **327**, 303–307 (1998).

[14] H. Huang, Y. L. Huang, J. Pflaum, A. T. S. Wee, W. Chen, *Appl. Phys. Lett.* **95**, 263309 (2009).

[15] M. Zhao, K. Deng, P. Jiang, S. S. Xie, D. Fichou, C. Jiang, *J. Phys. Chem. C* **114**, 1646-1650 (2010).

[16] G. Yu, J. Gao, J. C. Hunnelen, F. Wudl, A. J. Heeger, *Science* **270**, 1789-1791 (1995).

[17] P. Peumans, S. Uchida, and S. R. Forrest, *Nature* **425**, 158-162 (2003).

[18] F. Yang, M. Shtein, S. R. Forrest, *Nature Mater.* **4**, 37-41 (2005).

[19] W. L. Ma, C. Y. Yang, X. Gong, K. Lee, A. J. Heeger, *Adv. Funct. Mater*. **15**, 1617-1622 (2005).

[20] R. Otero, D. Ecija, G. Fernandez, J. M. Gallego, L. Sanchez, N. Martin, R. Miranda, *Nano Lett*. **7**, 2602-2607 (2007).

[21] L. Sánchez, R. Otero, J. M. Gallego, R. Miranda, N. Martin, *Chem. Rev.* **109**, 2081-2091 (2009).

[22] S. Uchida, J. G. Xue, B. P. Rand, S. R. Forrest, *Appl. Phys. Lett*. **84**, 4218-4220 (2004).

[23] R. A. Wolkow, *Annu. Rev. Phys. Chem.* **50**, 413-441 (1999), and references therein.

[24] H. Brune, *Surf. Sci. Rep.* **31**, 125-225 (1998), and references therein.

[25] S. W. Hla, K. H. Rieder, *Annu. Rev. Phys. Chem.* **54**, 307-330 (2003), and references therein.

[26] J. I. Pascual, N. Lorente, Z. Song, H. Conrad, H. P. Rust, *Nature* **423**, 525-528 (2003).

[27] Y. L. Huang, H. Li, J. Ma, H. Huang, W. Chen, A. T. S. Wee, *Langmuir* **26**, 3329-3334 (2010).

[28] Y. L. Huang, W. Chen, H. Li, J. Ma, J. Pflaum, A. T. S. Wee, *Small* **6**, 70-75 (2010).

[29] M. Tsukada, K. Kobayashi, N. Isshiki, H. Kageshima, *Surf. Sci. Rep*. **13**, 265-304 (1991).

[30] R. Wiesendanger, H.-J. Guntherodt, et al., *Scanning tunneling microscopy I: general principles and applications to clean and adsorbate-covered surfaces*, (Berlin; New York: Springer , c1992).

Chapter 7

Conclusions and Future Research

7.1 Summary of This Thesis

The work presented herein aimed to study 2D molecular self-assemblies on solid surfaces or surface-supported nanotemplates by LT-STM. Highly ordered molecular arrays stabilized by non-covalent interactions, including van der Waals force, intermolecular hydrogen bonding, intermolecular dipole-dipole interaction, interfacial π-π interaction and so on were successfully fabricated by careful design and selection of molecular building blocks and supporting substrates. It has been demonstrated that the 2D supramolecular arrangements (size and overall pattern) largely rely on the nature of the molecular building blocks (e. g., functionality, electronic properties, shape and size) as well as the underlying substrate. That is to say, to control the formation of 2D multicomponent molecular assemblies, the ability to manipulate the local molecular environment is very crucial.

In the first part of this work (chapter **3**), *in situ* LT-STM and synchrotron-based high-resolution PES and NEXAFS measurements were utilized to study the supramolecular arrangement, molecular orientation, and electronic structures of ultrathin F_{16}CuPc films and DIP films on surfaces. It was found that F_{16}CuPc molecules adopt the lying-down configuration on HOPG when the film thickness is below 5 nm (about 10-15 ML). The DIP molecules also lie flat on HOPG at one

monolayer thickness; when the film thickness increases to 10 nm, the DIP molecules adopt the lying-down configuration with their molecular planes slightly tilted away from the substrate. Such lying-down configurations are facilitated by the molecule-graphite interfacial π-π interactions. In contrast, DIP molecules stand upright on inert SiO_2 substrate due to weak interfacial interaction. Furthermore, the IP difference between the standing-up (on SiO_2) and lying-down (on HOPG) DIP films were studied by PES experiments. The IP was found to be orientation-dependent. The standing-up DIP film has lower IP compared to the lying-down film. The detailed investigations of how the supramolecular packing structures of π-conjugated planar molecules on surfaces, determined by the subtle competition between intermolecular interactions and molecule-substrate interactions, enable us to better control the organic film properties (e. g., molecular orientation and electronic energy level alignments).

We developed a novel bottom-up approach to fabricate tunable 2D binary molecular networks stabilized by multiple intermolecular hydrogen bonds on graphite in chapter **4**. By embedding different guest molecules (CuPc, 6P, pentacene or DIP) into the host molecular matrix (F_{16}CuPc monolayer), various molecular arrays with tunable intermolecular separations were formed. It is revealed that the supramolecular packing structures can be controlled by careful selection of molecular building blocks with appropriate geometry (size and shape) as well as relative molecular ratio in bi-component systems. By MD and DFT simulations, we confirmed that the structural stability of these binary systems is sustained through the formation of multiple intermolecular C-F···H-C hydrogen

bonds between the electronegative peripheral F atoms of F_{16}CuPc and the electropositive peripheral H atoms of CuPc, 6P, pentacene or DIP. The simulated results also suggested F···H distances of ~2.5-2.6 Å for the possible C-F···H-C hydrogen bonds in these networks, which are typical of weak hydrogen bonds. The fabrication of these tunable binary molecular networks suggests a promising route to design and construct tunable and robust molecular nanostructure arrays for molecular sensors, molecular spintronic devices, and single-molecular p-n nanojunctions.

Some of the binary molecular networks fabricated previously can be used as nano-templates to accommodate incoming guest molecules at specific adsorption sites. In chapter **5**, we demonstrated the assembly of 2nd layer F_{16}CuPc molecules on the DIP:F_{16}CuPc network formed at the ratio of 2:1 and 6P:F_{16}CuPc linear chain arrays. In both systems, the 2nd layer F_{16}CuPc molecules precisely adsorb atop the same type of molecules of the underlying host networks to form regular patterns, namely 2nd layer molecular dots and chain arrays respectively. Such preferential adsorption is attributed to interfacial π-π interactions between the 1st layer and 2nd layer F_{16}CuPc molecules. The utilization of interfacial π-π interactions to trap functional organic molecules at specific adsorption sites provides a possible method to fabricate organic nanostructure arrays over macroscopic areas. The studies of the preferential adsorptions atop 2D molecular networks are also helpful for the understanding of intermolecular interactions and kinetic growth processes at the atomic scale.

Finally, ClAlPc molecule with permanent electric polarity, a promising material for high-density data-storage bits, single-molecule switches, biosensors and so on, is investigated in chapter **6**. The formation of a molecular dipole monolayer on graphite surface by assembling ClAlPc molecules in a Cl-up configuration has been demonstrated by LT-STM. In contrast, the 2^{nd} layer ClAlPc molecules adopt a Cl-down configuration. We also investigated the formation of ClAlPc molecular chain arrays via nanoscale phase separation by the co-adsorption with DIP molecules. 1D molecular dipole chains are fabricated at different ClAlPc:DIP ratios with tunable inter-chain separation. Similar nanoscale phase separation is also observed in CuPc:DIP system, which suggests that this is a common phenomenon in binary systems of different phthalocyanine molecules with DIP. A tip-induced single-molecule switch is demonstrated via reversible manipulations of the ClAlPc molecular configurations, from Cl-up to Cl-down and *vice versa*, in the ClAlPc close-packed monolayer. The reversible single-molecule manipulation makes it become possible to write, read and erase information on the molecular dipole monolayer, and makes this dipolar molecule a possible candidate for use as a high-density storage bit.

7.2 Future Work

In this thesis, we have studied the self-assembly of different π-conjugated organic molecular systems on solid surfaces and surface-supported nanotemplates guided by various intermolecular interactions and molecule-substrate interactions.

However, the electronic properties of the well-defined 2D supramolecular networks (e. g., surface energy potential and electronic energy level alignment) as well as their potential applications are less clear so far. The construction of organic devices or molecular electronics based on molecular self-assembly is still in its infancy.

Theoretical simulations based on MD and DFT were employed to support some of our experimental results, e. g., roles played by the relatively weak C-F···H-C hydrogen bonding in some binary molecular systems. However, because of the restrictions of present simulation methods and computational power, it is impossible to obtain very precise formation energies involved in the molecular self-assemblies, such as intermolecular binding energies and molecule-substrate adsorption energies. Furthermore, subtle competitions among various relatively weak interactions (e. g., van der Waals forces, interfacial π-π interactions, and intermolecular dipole-dipole interactions) are still distinguishable. Complementary experiments and supporting simulation work are needed in order to address these outstanding issues.

Proposed future work includes:

(1) Measurements of the electronic properties of the 2D supramolecular nanostructures, including both mono- and bi- component systems. STS and PES measurements with high resolution can be used to determine possible charge transfer between neighboring molecules of the multi-component networks, or the electronic energy level alignments of the organic thin films, especially for those component molecules processing high charge carrier

mobility.

(2) Complementary experiments to determine the underlying mechanism that controls the single-molecule flipping of ClAlPc molecules on HOPG. It would be necessary to investigate the relationships between the switching probability and the pulse voltage, and also the tip-molecule separation. Measurements of the ClAlPc molecular conductivity at different configurations via STS are also needed.

(3) Studies of the molecular self-assembly on other surfaces such as Au(111), Ag(111) and Cu(111). The π-conjugated organic molecules usually have stronger molecule-substrate interactions with metallic single-crystal substrates than with graphite. In order to obtain a comprehensive understanding of how the molecule-substrate interactions affect the supramolecular packing structure and hence the electronic properties of the organic thin films, it is necessary to systematically study and compare the molecular assemblies on different substrates.

(4) Studies of other organic molecules with desirable functionalities, especially dipolar and magnetic molecules which have potential applications in molecular memory or spintronic devices. The routine fabrication of stable, regular molecular dipole or electronic spin arrays would be advantageous. Moreover, investigations of the supramolecular self-assembly mediated by dipole-dipole interactions or spin-spin coupling would be of interest, and which are seldom reported.